

Crop Growth Monitoring by Hyperspectral and Microwave Remote Sensing

**Inaugural-Dissertation
zur Erlangung des Doktorgrades
der Mathematisch-Naturwissenschaftlichen Fakultät
der Universität zu Köln**

vorgelegt von
Wolfgang Koppe
aus Jena

Friedrichshafen, 12.11.2013

Berichterstatter: Prof. Dr. Georg Bareth
Prof. Dr. Karl Schneider

Tag der mündlichen Prüfung: 21.01.2014

ABSTRACT

Timely monitoring of crop growth status at different scales is crucial for improving regional crop management decisions. The main objective of the recent study is a model development to predict and estimate crop parameters, here biomass, plant N concentration and plant height, based on different earth observation systems that provide complementary information. Among these are the hyperspectral sensor Hyperion and the multi-spectral sensor ALI based on EO-1 satellite, ASAR on Envisat and TerraSAR-X. Based on the characteristics of the different systems, methods are analysed regarding crop parameter estimation and crop growth status monitoring on a regional level. Factors which are taken into account for optical data are bandwidth and centre of the wavebands, spectral reflectance response from visible and near infrared and the performance of vegetation indices based on the two sensors for semi-empirical parameter estimation. Concerning the SAR sensors Envisat ASAR and TerraSAR-X, parameters such as wavelength, incidence angle and polarization were analysed in terms of crop parameter retrieval and crop status determination. For this, two test areas, one for winter wheat in Northern China Plain (Huimin County) and one for rice in the Northeast of China (Jiansanjiang) were selected. At both sites, intensive ground data collection during the vegetation periods in 2006, 2007 for Huimin and 2009 and 2011 for Jiansanjiang were performed.

Concerning the winter wheat crop monitoring based on hyperspectral, multi-spectral and C-band SAR data, the study was conducted in Huimin County, Shandong Province of China in the growing season of 2005/2006 involving three large winter wheat fields each year managed by different farmers. Winter wheat growth parameters including aboveground biomass, plant N concentration, LAI, and plant height were collected at different growth stages. Three different prediction models were investigated: traditional vegetation indices calculated from broad and narrow bands, and Normalized Ratio Indices (NRI) calculated from all possible two-band combinations of Hyperion between 400 and 2500 nm. The results indicated that TVI performed best among the tested vegetation indices using either broad bands ($R^2 = 0.69, 0.32$ and 0.64 for biomass, N concentration and plant height, respectively) or narrow bands ($R^2 =$

0.71, 0.33 and 0.65 for biomass, N concentration and plant height, respectively). The best performing Normalized Ratio Index (NRI) selected through band combination analysis were significantly better than TVI, achieving R^2 of 0.83, 0.81 and 0.79 for biomass, plant N concentration and plant height, respectively. The different NRI models use wavebands from the NIR (centred at 874, 732, and 763 nm) and the SWIR (centred at 1225 and 1305 nm) spectrum with varying bandwidth between 10 and 190 nm. The result of this part proved that vegetation indices derived from NIR- and SWIR-Hyperion spectrum are better predictors of plant aboveground biomass, nitrogen concentration and plant height than indices derived from only visible spectrum. In addition, Envisat ASAR VV polarization data were related to winter wheat crop parameters. Bivariate correlation results from this study indicate that both multi-temporal EO-1 Hyperion as well as Envisat ASAR data provides notable relationships with crop conditions. As expected, linear correlation of hyperspectral data performed slightly better for biomass estimation ($R^2 = 0.83$) than microwave data ($R^2 = 0.75$) for the 2006 field survey. Based on the results, hyperspectral Hyperion data seem to be more sensitive to crop conditions. Improvements for crop parameter estimation were achieved by combining hyperspectral indices and microwave backscatter into a multiple regression analysis as a function of crop parameter. Combined analysis was performed for biomass estimation ($R^2 = 0.90$) with notable improvements in prediction power.

For the rice monitoring in the Sanjiang Plain, Northeast China, the main objective was the understanding of the coherent co-polarised X-band backscattering signature of rice at different phenological stages in order to retrieve growth status. For this, multi-temporal dual polarimetric TerraSAR-X High Resolution SpotLight data (HH/VV) as well as single polarised StripMap (VV) data were acquired from the test site. In conjunction with the satellite data acquisition, a ground truth field campaign was carried out.

The backscattering coefficients at HH and VV of the observed fields were extracted on the different dates and analysed as a function of rice phenology to provide a physical interpretation for the co-polarised backscatter response in a temporal and spatial manner. Then, a correlation analysis was carried out between TerraSAR-X

backscattering signal and rice biomass of stem, leaf and head to evaluate the relationship with different vertical layers within the rice vegetation.

HH and VV signatures show two phases of backscatter increase, one at the beginning up to 46 days after transplanting and a second one from 80 days after transplanting onwards. The first increase is related to increasing double bounce reflection from the surface-stem interaction. Then, a decreasing trend of both polarizations can be observed due to signal attenuation by increasing leaf density. A second slight increase is observed during senescence. Correlation analysis showed a significant relationship with different vertical layers at different phenological stages which prove the physical interpretation of X-band backscatter of rice. The seasonal backscatter coefficient showed that X-band is highly sensitive to changes in size, orientation and density of the dominant elements in the upper canopy.

Overall, the study demonstrated successfully the estimation of crop status by multi-sensoral remote sensing data. The use of different sensor systems to acquire timely information is especially important for agricultural decision support systems. Thus, as many different systems are available in the future, the combination of different satellite sources is gaining more importance.

KURZZUSAMMENFASSUNG

Methoden und Techniken der Fernerkundung fungieren als wichtige Hilfsmittel im regionalen Umweltmanagement. Um diese zu optimieren, untersucht die folgende Arbeit sowohl die Verwendung als auch Synergien verschiedener Sensoren aus unterschiedlichen Wellenlängenbereichen.

Der Fokus liegt auf der Modellentwicklung zur Ableitung von Pflanzenparametern aus fernerkundlichen Bestandsmessungen sowie auf deren Bewertung. Zu den verwendeten komplementären Fernerkundungssystemen zählen die Sensoren EO-1 Hyperion und ALI, Envisat ASAR sowie TerraSAR-X. Für die optischen Hyper- und Multispektralsysteme werden die Reflexion verschiedener Spektralbereiche sowie die Performanz der daraus abgeleiteten Vegetationsindizes untersucht und bewertet. Im Hinblick auf die verwendeten Radarsysteme konzentriert sich die Untersuchung auf Parameter wie Wellenlänge, Einfallswinkel, Radarrückstreuung und Polarisierung. Die Eigenschaften verschiedener Parameterkombinationen werden hierbei dargestellt und der komplementäre Beitrag der Radarfernerkundung zur Wachstumsüberwachung bewertet. Hierzu wurden zwei Testgebiete, eines für Winterweizen in der Nordchinesischen Tiefebene und eines für Reis im Nordosten Chinas ausgewählt. In beiden Gebieten wurden während der Wachstumsperioden umfangreiche Feldmessungen von Bestandsparametern während der Satellitenüberflüge oder zeitnah dazu durchgeführt.

Mit Hilfe von linearen Regressionsmodellen zwischen Satellitendaten und Biomasse wird die Sensitivität hyperspektraler Reflexion und Radarrückstreuung im Hinblick auf das Wachstum des Winterweizens untersucht. Für die optischen Daten werden drei verschiedene Modelvarianten untersucht: traditionelle Vegetationsindizes berechnet aus Multispektraldaten, traditionelle Vegetationsindizes berechnet aus Hyperspektraldaten sowie die Berechnung von Normalised Ratio Indices (NRI) basierend auf allen möglichen 2-Band Kombinationen im Spektralbereich zwischen 400 und 2500 nm. Weiterhin wird die gemessene Biomasse mit der gleichpolarisierten (VV) C-Band Rückstreuung des Envisat ASAR Sensors linear in Beziehung gesetzt. Um den

komplementären Informationsgehalt von Hyperspektral und Radardaten zu nutzen, werden optische und Radardaten für die Parameterableitung kombiniert eingesetzt.

Das Hauptziel für das Reisanbaugebiet im Nordosten Chinas ist das Verständnis über die kohärente Dualpolarimetrische X-Band Rückstreuung zu verschiedenen phänologischen Wachstumsstadien. Hierfür werden die gleichpolarisierte TerraSAR-X Rückstreuung (HH und VV) sowie abgeleitete polarimetrische Parameter untersucht und mit verschiedenen Ebenen im Bestand in Beziehung gesetzt. Weiterhin wird der Einfluss der Variation von Einfallswinkel und Auflösung auf die Bestandsparameterableitung quantifiziert. Neben der Signatur von HH und VV ermöglichen vor allem die polarimetrischen Parameter Phasendifferenz, Ratio, Kohärenz und Entropy-Alpha die Bestimmung bestimmter Wachstumsstadien.

Die Ergebnisse der Arbeit zeigen, dass die komplementären Fernerkundungssysteme Optik und Radar die Ableitung von Pflanzenparametern und die Bestimmung von Heterogenitäten in den Beständen ermöglichen. Die Synergien diesbezüglich müssen auch in Zukunft weiter untersucht werden, da neue und immer variablere Fernerkundungssysteme zur Verfügung stehen werden und das Umweltmanagement weiter verbessern können.

ACKNOWLEDGEMENT

The thesis was embedded in The International Center For Agro-Informatics and Sustainable Development (ICASD). The research of this project was supported by different institutions and companies: the Natural Science Foundation of China (Project number: 30571080), International Bureau of the BMBF, the GIS&RS Group of the University of Cologne, the Sino-German Cooperative Nitrogen Management Project (MOST 2007DFA30850), the Qixing Research and Development Center in Heilongjiang and Astrium GEO-Information Services.

The thesis was supervised by Prof. Dr. Georg Bareth, which is also the person to whom I owe most for many reasons. First, he was giving me the chance to come to the University of Cologne to participate in his pleasant working group and to start working on the thesis. Furthermore, his enthusiastic and motivating way of supervising was like a “fountain” of ideas and always refreshing which enabled me to continue and accomplish the thesis, even in difficult times. After leaving the University and the interesting city of Cologne, Prof. Bareth provided always support and continued taking care for me – Vielen Dank!

I also thank to Prof. Dr. Karl Schneider, for his willing to act as the second examiner for the thesis and for providing software licences and support during my time in Cologne.

Furthermore, my sincerely thanks to

- Jürgen Janoth, for fully supporting my PhD activities at Infoterra.
- Simon Hennig and Martin Gnyp and many more students for working hard in the field.
- All colleagues of the “Bareth working group”, for the always fruitful collaboration and for not getting tired to weaken my dislike of Cologne and for making it a nice place for living.

And finally special thanks to my parents, who always supported the long and rocky way with warm words and Thüringer Klöße!

TABLE OF CONTENT

ABSTRACT	I
KURZZUSAMMENFASSUNG.....	IV
ACKNOWLEDGEMENT	VI
TABLE OF CONTENT.....	VII
LIST OF FIGURES.....	IX
LIST OF TABLES.....	XI
LIST OF ABBREVIATIONS.....	XII
1 INTRODUCTION	1
1.1 Motivation.....	1
1.2 Thesis Outline.....	3
1.3 Remote Sensing for Supporting Crop Monitoring.....	4
1.4 Objective and Hypotheses	10
2 LITERATURE REVIEW.....	12
2.1 Multispectral and Hyperspectral Imaging	12
2.1.1 Reflectance Properties.....	12
2.1.1.1 Atmospheric Effects	15
2.1.1.2 Radiance and Reflectance	16
2.1.2 Hyperspectral Crop Monitoring*	17
2.2 Synthetic Aperture Radar.....	19
2.2.1 SAR System Parameters.....	20
2.2.1.1 Frequency.....	20
2.2.1.2 Radar Equation.....	21
2.2.1.3 Range and Azimuth Resolution	22
2.2.2 Properties of Imaging Radar	23
2.2.2.1 Speckle	23
2.2.2.2 Image Geometry and Geometric Distortions	24
2.2.2.3 SAR Interaction with the Target.....	25
2.2.2.4 Scattering Mechanism.....	27
2.2.2.5 Polarization	30
2.2.2.6 Compact Polarimetric Data	32
2.2.3 State of the Art SAR Crop Monitoring.....	32
2.2.3.1 Rice Crop Monitoring	33
2.2.3.2 Winter Wheat Crop Monitoring	36
2.3 Synergism of Optical and SAR	37
3 METHODS AND USED DATA	40
3.1 Ground Truth	42
3.1.1 Huimin County Test Site*.....	42
3.1.1.1 Experimental Design	43
3.1.1.2 Field Measurements.....	44
3.1.2 Jiansanjiang Test Site*	49
3.1.2.1 Experimental Design	50
3.1.2.2 Field Measurements.....	52
3.2 Satellite Data Acquisitions, Processing and Analysis.....	53
3.2.1 EO-1 Hyperion and ALI*	55
3.2.1.1 EO-1 Hyperion and ALI Processing	56
3.2.1.2 Analysis of Hyperspectral EO-1 Hyperion Data	58

3.2.2	Envisat ASAR Processing*	60
3.2.3	TerraSAR-X Processing	63
3.2.3.1	Speckle Suppression	65
3.2.3.2	Power	68
3.2.3.3	Correlation	69
3.2.3.4	Compact Polarimetric Decomposition	71
3.2.4	Statistical Analysis*	72
4	RESULTS	75
4.1	Crop Phenological Development	75
4.1.1	Winter Wheat Growth*	75
4.1.2	Rice Growth	78
4.2	Hyperspectral Imaging of Winter Wheat	83
4.2.1	Spectral Reflectance as a Function of Crop Parameters*	83
4.2.2	Spectral Vegetation Indices and the Relationship with Crop Parameters*	86
4.2.2.1	Single Band Relationship with Crop Parameters	86
4.2.2.2	Standard Broad Band and Narrow Band Vegetation Indices	87
4.2.2.3	Relationship of Narrow Band Normalized Ratio Indices (NRI) with Crop Parameters	88
4.2.2.4	Validation of NRI model	89
4.2.3	Discussion of Multispectral and Hyperspectral Data for Winter Wheat Monitoring*	91
4.2.3.1	Processing of EO-1 Data	91
4.2.3.2	Single Band and Standard Vegetation Indices	92
4.2.3.3	Narrow Band Normalized Difference Indices	93
4.3	Winter Wheat Monitoring with C-band	96
4.3.1	Temporal Backscatter Behaviour of Winter Wheat	96
4.3.2	Relating Crop Condition to Envisat ASAR	98
4.3.3	Discussion of C-band SAR Data for Wheat Monitoring	99
4.4	Synergy of Hyperspectral and C-band SAR Data for Crop Parameter Estimation*	100
4.5	Polarimetric Rice Monitoring with X-band	102
4.5.1	Power: Backscattering Signature and Ratio	102
4.5.1.1	Incidence Angle Differences	103
4.5.1.2	Typical Backscattering Signature	104
4.5.1.3	Co-pol Ratio (HH/VV)	105
4.5.2	Correlation: Polarimetric Coherence and Phase Difference	106
4.5.3	Polarimetric Decomposition: Alpha and Entropy	107
4.5.4	Correlation Analysis between Backscattering Coefficients and Plant Variables*	108
4.5.5	Polarimetric Growth Stage Monitoring	111
4.5.6	Discussion of Polarimetric Rice Monitoring*	113
4.5.6.1	Incidence Angle	119
4.5.6.2	Polarimetric Parameters	119
5	SYNERGISTIC SUMMARY AND CONCLUSION	122
5.1	Hyperspectral Imaging	123
5.2	SAR C-band Imaging and Synergism of Optic and SAR	124
5.3	SAR X-band Imaging	125
5.4	Validation of Hypothesis and Objectives	126
5.4.1	Huimin Test Site	126
5.4.2	Jiansanjiang Test Site	128
6	REFERENCES	129
	APPENDIX	141
A.1:	Selection of Standard Vegetation Indices	141
A.2:	TerraSAR-X HH and VV Imagery of Rice	142
A.3:	Separability of Rice against other Crops	145
A.4:	Polarimetric parameters for rice and non-rice.	148

LIST OF FIGURES

Figure 1-1: Recent and future earth observation optical satellite missions.	7
Figure 1-2: Recent and future earth observation SAR satellite missions.	8
Figure 2-1: Hyperspectral image cube of EO-1 Hyperion extracted over the study site in Huimin County.	14
Figure 2-2: Typical reflectance curves (soil and vegetation) extracted from EO-1 Hyperion of Huimin County (April 19, 2006).	15
Figure 2-3: Inter-relationship between wavelength and frequency for the most common SAR systems on a log scale (modified after Henderson & Lewis 1998).	21
Figure 2-4: Imaging geometry of side looking SAR (modified after Woodhouse 2006). θ_l is the look angle, θ_d is the depression angle and θ_i the incidence angle.	24
Figure 2-5: Backscatter as a function of surface roughness (after Woodhouse 2006).	27
Figure 3-1: Overview of processing steps applied in the thesis.	41
Figure 3-2: Test sites in Huimin County (Gnyp et al. 2013).	43
Figure 3-3: Farming fields in Huimin County.	44
Figure 3-4: Farming fields in Huimin County with measurement points.	45
Figure 3-5: Arrangement of canopy spectral reflectance measurements with ASD Handheld and QualitySpec (modified after Laudien 2007).	47
Figure 3-6: Canopy spectral reflectance measurements at April 7, 2006 (Photo Martin Gnyp).	48
Figure 3-7: Test sites in Jiansanjiang (Gnyp et al. 2013).	49
Figure 3-8: Experimental design of the Jiansanjiang test site.	51
Figure 3-9: Small plots within larger rice fields (Photo Martin Gnyp 2009).	52
Figure 3-10: Pre-processing steps of EO-1 Hyperion data.	56
Figure 3-11: Comparison of single pixel spectra before (a) and after (b) atmospheric correction. Spectra were acquired on April 19, 2006.	57
Figure 3-12: Processing chain of Envisat ASAR.	61
Figure 3-13: Processing chain of TerraSAR-X.	65
Figure 3-14: SAR filter results (based on HS, August 8, 2009). Left: Unfiltered. Middle: Level Bell. Right: Anisotropic, 8 iterations.	68
Figure 4-1: Biomass development of winter wheat in 2006 and dates of image and ground truth acquisition.	76
Figure 4-2: Spatial-temporal distribution of dry matter of two fields in 2006.	77
Figure 4-3: Rice growth stages, growth phases as well as plant height and total biomass graphs of the growing season of 2009 and 2011. Time is represented in days after transplantation (modified after Koppe et al. 2013).	81
Figure 4-4: Total dry matter and yield measured at the farmers' fields. Fields with biomass measurements and plots with detailed sampling.	82
Figure 4-5: Reflection behavior of winter wheat (Xili). Left: recorded by ASD Fieldspec (blue) and EO-1 Hyperion (red) in 2006. Right: recorded by QualitySpec (blue) and EO-1 Hyperion (red) in 2007.	84

Figure 4-6: Correlation coefficient (r) between Hyperion single band reflection and biomass in the growing season of 2006.	87
Figure 4-7: Coefficient of determination (R^2) between Hyperion narrow band vegetation indices calculated from all possible two-band combinations and biomass (a) and total nitrogen content (b) (Koppe et al. 2010a).	89
Figure 4-8: Measured versus predicted aboveground biomass using the regression model described in equation 4.2 (Koppe et al. 2012).	91
Figure 4-9: Scatterplot of (a) aboveground biomass against standard narrow band NDVI and (b) best waveband combination from NRI, 874 nm and 1225 nm (Koppe et al. 2010a).	95
Figure 4-10: Temporal evolution for bare soil (green) and winter wheat (blue) of C-VV backscatter (Koppe et al. 2012).	96
Figure 4-11: C-VV backscatter related to aboveground biomass (Koppe et al. 2012).	99
Figure 4-12: Mean temporal backscattering coefficient (σ^0) for different incidence angles of VV and HH of rice during the vegetation periods in 2009 and 2011. (a) SL, 26°. (b) HS, 39° and SM, 36°. (c) SL, 46°.	103
Figure 4-13: TerraSAR-X Spotlight images at HH (top), VV (down) at three acquisition dates in 2009 (modified after Koppe et al. 2013).	104
Figure 4-14: HH/VV ratio of six rice parcels as a function of time at 26° incidence angle.	106
Figure 4-15: Co-polar phase difference and coherence of six rice parcels as a function of time at 26° incidence.	107
Figure 4-16: Co-polar eigenvector decomposition (α and entropy) of six rice parcels at 26° incidence.	108
Figure 4-17: Relating phenological stage of rice to polarimetric parameters.	112
Figure 4-18: Correlation coefficients of TerraSAR-X HS backscatter (VV and HH) with stem, leaf, head and total biomass at DAT 35, 46 and 79.	115
Figure 4-19: Backscatter behavior of rice at different growth stages. (a) Flooded rice field, DAT 0. (b) Early vegetative stage, DAT 35. (c) Late vegetative stage, DAT 46. (d) Reproductive stage, DAT 79.	116
Figure 4-20: Left: Comparison of σ^0 signature between problematic fields (blue dashed line) and average of the normal growing fields (red solid line) based on SM VV backscatter. Upper right: Photo of a problematic field. Lower right: Photo of a normally growing field.	117
Figure 4-21: Left: Comparison of coherence signatures of different land cover classes. Right: Coherence image (July 7, 2011).	121
Figure A-1: Landcover classification (TerraSAR-X HS 2009, July 5 and July 27) (modified after Hütt, 2012), overlaid by experimental plots.	142
Figure A-2: TerraSAR-X HH and VV images (incidence angle 26°) of growing season of 2011).	144
Figure A-3: X-band backscatter (inc. angle 39°) of HH and VV of rice crop 2009.	145
Figure A-4: TerraSAR-X color composite of DAT 46 and DAT 68 (2009).	145
Figure A-5: Separability analyses of land cover classes based on HH and VV difference (modified after Hütt 2012).	146
Figure A-6: Separability analyses of land cover classes based on α angle (modified after Hütt 2012).	146
Figure A-7: Land cover classifications (modified after Hütt 2012).	147
Figure A-8: Polarimetric parameters for rice and non-rice for incidence angle of 26° and 46°.	149

LIST OF TABLES

Table 2-1: Crop characteristics which influence remote sensing in the VIS – NIR and in the microwave domain (Kühbauch & Hawlitschka 2003).	38
Table 3-1: Soil chemical properties of the farming fields in 2006 (Li et al. 2008).	44
Table 3-2: Sensor specifications of ASD Field Spec and Quality Spec (Analytical Spectral Devices 1999)..	47
Table 3-3: Acquired satellite data for the test sites Huimin and Jiansanjiang (modified after Koppe et al. 2012 and Koppe et al. 2013).	54
Table 3-4: Technical specification of EO-1 Hyperion and ALI.	55
Table 3-5: Standard vegetation indices evaluated in this study (Koppe et al. 2010a).....	59
Table 3-6: Technical specification of Envisat ASAR.....	61
Table 3-7: Technical specification of TerraSAR-X and TanDEM-X.....	64
Table 3-8: Quantitative measurement of noise for standard adaptive and experimental filters.	67
Table 4-1: Crop growth variables measured at different dates in 2006 and 2007 (Koppe et al. 2012).	77
Table 4-2: Statistics of measured agronomic parameters during the field campaign 2009 (modified after Koppe et al. 2013).	79
Table 4-3: Information about field experiments in 2009 and 2011.....	80
Table 4-4: Coefficient of determination (R^2) between ALI broad band, Hyperion narrow band vegetation indices and measured agronomic parameters (Koppe et al. 2010a).....	86
Table 4-5: Coefficient of determination (R^2) between biomass and NRI for the validation model based on multi-temporal and mono-temporal data (modified after Koppe et al. 2012).	90
Table 4-6: Coefficient of determination (R^2) between biomass and Envisat ASAR backscatter (Koppe et al. 2012).	99
Table 4-7: Coefficient of determination (R^2) between biomass and Envisat ASAR backscatter (Koppe et al. 2012).	101
Table 4-8: Correlation coefficients (R^2) between backscatter (HH and VV) and plant variables, including total biomass of the whole plant and the components stem, leaf and head for HS and SM (modified after Koppe et al. 2013).	110
Table 5-1: Validation of objective and hypothesis for Huimin test site.....	127
Table 5-2: Validation of objective and hypothesis for Jiansanjiang test site.....	128
Table A-1: Standard vegetation indices.	141

LIST OF ABBREVIATIONS

ALI	Advanced Land Imager
ASAR	Advanced Synthetic Aperture Radar
ASD	Analytical Spectral Device
BBCH	Biologische Bundesanstalt, Bundessortenamt und Chemische Industrie
BIOM	Biomass
DAT	Day After Transplanting
dB	Decibel
DN	Digital Number
ENL	Effective Number of Looks
EO-1	Earth Observing 1 mission
FAO	Food Agricultural Organization
GCP	Ground Control Point
GHz	Gigahertz
GIS	Geographical Information System
GMES	Global Monitoring for Environment and Security
HH	Horizontal-Horizontal (polarization)
HR	High Resolution
HS	High-Resolution SpotLight
IEEE	Institute of Electrical and Electronics Engineers
ICASD	International Center for Agro-Informatics and Sustainable Development
IR	Infrared
LAI	Leaf Area Index
MARS	Monitoring Agricultural ResourceS
NDVI	Normalized Differenced Vegetation Index
NIR	Near Infrared
NRI	Normalised Ratio Index
OSAVI	Optimised Soil-Adjusted Vegetation Index
PAZ	Identical satellite to TerraSAR-X, Spanish for peace

POLInSAR	Polarimetric Interferometric SAR
PPD	Polarimetric Phase Difference
PRF	Pulse Repetition Frequency
PWC	Plant Water Content
RADAR	Radio Detection and Ranging
RAR	Real Aperture Radar
REP	Red Edge Position
RE	Relative Error
RMSE	Root Mean Square Error
SAR	Synthetic Aperture Radar
SEAMLESS	System for Environmental and Agricultural Modelling; Linking European Science and Society
SLAR	Side Looking Radar Systems
SL	SpotLight
SM	StripMap
SR	Simple Ratio
SWIR	Short Wave Infrared
TCI	Triangle Chlorophyll Vegetation Index
STD	Standard Deviation
TIROS	Television and InfraRed Observation Satellite
TanDEM-X	TerraSAR-X-Add-on for Digital Elevation Measurements
TVI	Triangular Vegetation Index
UAV	Unmanned Aerial Vehicle
VHR	Very High Resolution
VIS	Visible
VV	Vertical-Vertical (polarization)
WB	World Bank
WFP	World Food Program
WRS	World Reference System

1 INTRODUCTION

The recent study with its elaborate design would not have been possible without and is closely interwoven with the research of The International Center For Agro-Informatics and Sustainable Development (ICASD). The ICASD is a cooperation between the Institute of Geography, University of Cologne and the College of Resources and Environmental Sciences, China Agricultural University. The overall mission of the Center is to promote the sustainable development of intensive agriculture, an efficient management of natural resources as well as the application of information technology in agriculture.

Within the framework of this cooperation, the focus of this thesis lies on the integration of active and passive remote sensing technologies into modern agricultural management.

1.1 Motivation

As cereal grains, rice (*Oryza*) and wheat (*Triticum*) are the most important agricultural crops covering together 369 million ha of earth's surface in 2010, accounting for 53% of total harvested area of cereal crops in 2010 (FAOSTATS 2013). The productions quantity amounts to 672 million tons rice and 650 million tons wheat in 2010, representing over 54% of the total production amount of cereal crops. Over the last 40 years, the cereal production quantity increased by 20% in average per decade, whereas the harvested area remains constant in a certain range (FAOSTATS 2013). As a consequence, most of the increase must be attributed to a more efficient agricultural production due to increase of fertilizer, pesticides and water supply as well as the usage of new cropping technologies. Beside to positive effects concerning productivity, along with the intensification of agricultural production also environmental problems may arise. The use of pesticides and over-fertilization contaminates surface and ground water unintendedly (Miller 2004); irrigation of crops in dry areas can lead to depletion of underground aquifers, subsidence and salinization (ILRI 1989). As a consequence, the intensive agriculture may aggravate temporal and permanent land

degradation or land use change. In 2012, global agriculture had to feed around seven billion people, and although the population growth rate is expected to decrease, in 2050 the global population will be more than nine billion (UN Database 2012). Based on these figures, improvement in production efficiency must further accelerate to guarantee food security for the next decades. According to FAO (2013), the definition of food security is as follows: “Food security is a situation that exists when all people, at all times, have physical, social and economic access to sufficient, safe and nutritious food that meets their dietary needs and food preferences for an active and healthy life”. To meet the goals and requirements for food security, different programs were established. From an European perspective, the most important program is the Global Monitoring for Environment and Security (GMES, from 2013 Copernicus), whereas one of the ‘Land Applications’ aims at global food security. For this, a global crop monitoring service shall be established with the objective of near real-time crop condition assessment and yield forecast (GMES 2012). Another European program, already established in 1988, is the Monitoring Agricultural Resources (MARS), providing scientific support in terms of agro-meteorological crop modelling, yield forecast and crop inventories in- and outside Europe (MARS 2012). There are further initiatives for improving food security on continental and global level, e.g. the Food and Agricultural Organization (FAO), the World Bank (WB), the World Food Programme (WFP) or the System for Environmental and Agricultural Modelling – Linking European Science and Society (SEAMLESS 2012). Beside these initiatives for food security, there is parallel also a commercial market emerging in the field of agricultural services for insurance and finance. Especially the crop insurance market is interested in timely information on productivity and an end-to-end service solution on crop status and yield forecast. In conclusion, the identified stakeholders of timely agricultural information are numerous, but primarily include: policy makers, organizations responsible for food security and environment, land use planners, crop insurances as well as the financial market controlling prices and trade volumes.

In the mentioned initiatives and programs, remote sensing based technologies are important tools for information extraction and decision support. In this context, remote sensing is used for gathering spatial-temporal crop information to calibrate

crop growth models, provide spatial variability information of crop status and final yield forecast. In particular, to cope with the imbalance between food supply and demand today and in the future, there is strong need to further investigate and develop agricultural monitoring systems that assure a sustainable use of land resources (Justice & Becker-Restef 2007).

1.2 Thesis Outline

The present thesis uses different data acquisition methods such as space-borne active and passive remote sensing, in-situ ground truth measurements and interviews to allow a quantitative analysis of the data.

Chapter 1 addresses the benefit of using remote sensing data for spatial-temporal agricultural monitoring. An overview of actual and future sensor systems for earth observation is given. Furthermore, the motivation, hypothesis and objectives and the significance of the thesis are highlighted. Chapter 2 reviews the physical properties of remote sensing, the properties of imaging spectroscopy as well as the properties of radar imagery. One focus in this chapter is put on the physics of radar imaging. Beside the physics, a literature review of agricultural monitoring based on hyperspectral and radar sensor systems is provided. In the methods part (Chapter 3) an introduction into the two different test areas, which were explored in the framework of this study, is given. Additionally to this, the used satellite imagery and the processing methods are presented. This includes the image pre-processing, the core processing of the satellite data, the collection and analysis of the ground truth data. The results of the study are presented in chapter 4. At first, winter wheat and rice phenological development are described. Subsequently the results of hyperspectral and radar crop monitoring of winter wheat are presented, followed by the polarimetric analysis of X-band rice monitoring. In each of the three sections, the results are discussed in relation to state of the art research. In chapter 5, the results and discussions from chapter 4 are summarised in relation to the objectives and hypothesis of the thesis.

The thesis is based on three published papers, which form the core of the study. The topics addressed in the three papers are summarized in Figure 3-1. Additionally to the

papers, a literature review addressing the theoretical fundamentals of optical and radar remote sensing as well as a polarimetric analysis of the X-band data was carried out. The published papers are:

- KOPPE, W., GNYP, M. L., LAUDIEN, R., JIA, L., LI, F., CHEN, X., ZHANG, F., & BARETH, G., 2006: Deriving of winter wheat characteristics from combined radar and hyperspectral data analysis. – SPIE Proceedings, Geoinformatics'2006, Wuhan, China.
- KOPPE, W., LI, F., GNYP, M. L., MIAO, Y., JIA, L., CHEN, X., ZHANG, F., & BARETH, G., 2010: Evaluating Multispectral and Hyperspectral Satellite Remote Sensing Data for Estimating Winter Wheat Growth Parameters at Regional Scale in the North China Plain. – Photogrammetrie, Fernerkundung, Geoinformation, **3**: 167-178.
- KOPPE, W., GNYP, M. L., YAO, Y., MIAO, Y., & BARETH, G., 2011: Agricultural Monitoring with Spaceborne X-band SAR Data. – Proceedings on the Workshop of Remote Sensing Methods for Change Detection and Process Modelling, 18-19 November 2010, University of Cologne, Germany, Kölner Geographische Arbeiten, **92**: 55-61.
- KOPPE, W., HENNIG, S. D., LI, F., GNYP, M. L., MIAO, Y., JIA, L., CHEN, X., & BARETH, G., 2012: Multi-Temporal Hyperspectral and Radar Remote Sensing for Estimating Winter Wheat Biomass in the North China Plain. – Photogrammetrie, Fernerkundung, Geoinformation, **3**: 281-298.
- KOPPE, W., LI, F., GNYP, M. L., HÜTT, C., MIAO, Y., YAO, Y., CHEN, X., & BARETH, G., 2013: Rice monitoring with multi-temporal and dual-polarimetric TerraSAR-X data. – International Journal of Applied Earth Observation and Geoinformation, **21**: 568-576.

1.3 Remote Sensing for Supporting Crop Monitoring

To meet the requirements for sustainable resource management, a continuous monitoring and evaluation of resources is essential. Important information for decision support on local, regional and global level are:

- information about cropped areas and crop type
- timely information on production estimate
- yield forecast

This information needs to be updated on a regular basis, as it is fundamental in terms of agricultural production assessment and change of land use on different spatial levels. To account frequently for agricultural production, land cover and land use, yield forecast and environmental problems, diverse methods are used that serve different scales. Among others, these methods surveys regarding land use and interview of

farmers (De Groote & Traoré 2005), collection of statistical data (FAOSTAT 2013), crop growth modelling such as ORYZA for rice (Bouman et al. 2001) as well as airborne and spaceborne remote sensing data acquisition (Moran et al. 1997). As this thesis addresses low scale spatial monitoring, the following chapters focus on space-borne remote sensing for agricultural applications.

Remote sensing is a data acquisition method that acquires information about objects on earth's surface without any physical contact. For data retrieval the electromagnetic radiation in different wavelength is used. In general, the sensor systems are mounted on UAV (Unmanned Aerial Vehicle), plane or satellite (Albertz 2009).

Space-borne satellite earth observation allows for frequent monitoring of agricultural areas in different wavelength and spatial resolutions. The use of satellite remote sensing for earth observation has a long history. Already in the early 1960s, the first low-resolution television camera mounted on a satellite (TIROS mission – Television and InfraRed Observation Satellite) was brought into space for monitoring purpose. Since the early 1960s, many earth observations satellites with different characteristics have been launched in order to image earth surface. Today there is a wide variety of sensor systems available, whereas the main distinguishing factors in terms of monitoring applications are:

- Orbit (sun synchronous, geosynchronous) and revisit time
- Operating frequency range
- Footprint size / swath width
- Sensor resolution and radiometric performance
- Number of spectral bands or polarizations

The listed parameters characterize the different sensor systems and qualify them for dedicated monitoring applications such as agricultural monitoring. In Figure 1-1 and Figure 1-2 recent and future commercial and scientific earth observation missions are shown. The earth observations missions with optical sensors are separated into High Resolution missions (HR) with up to 1 m resolution and Very High Resolution missions (VHR) with a resolution higher than 1 m. As apparent from the Figure 1-1 and Figure

1-2, a lot of space-borne optical imaging systems from medium to very high resolution are currently available that can contribute to agricultural monitoring at different spatial and temporal scales. In the field of radar sensors there are many different systems currently in orbit. In Figure 1-2 the SAR missions are distinguished in X-, C-, S-, and L-band. In the future there will be a large number of X-band systems, the four satellites from the Cosmo-Skymed 2nd generation mission or TerraSAR-X2 as well. There is also a large number of missions in longer wavelength, enabling a complementary use of the different frequencies. In terms of SAR, the trend is towards higher resolution, larger swath width, shorter revisit time by constellation missions and full polarization.

The wide variety of missions in the optical and SAR domain allow for using complementary information with short time intervals to improve agricultural monitoring tasks. In the recent thesis, data from hyperspectral optical mission EO-1 Hyperion and from the SAR missions Envisat ASAR (C-band) and TerraSAR-X (X-band) are used to extract information for crop status monitoring.

Figure 1-1: Recent and future earth observation optical satellite missions.

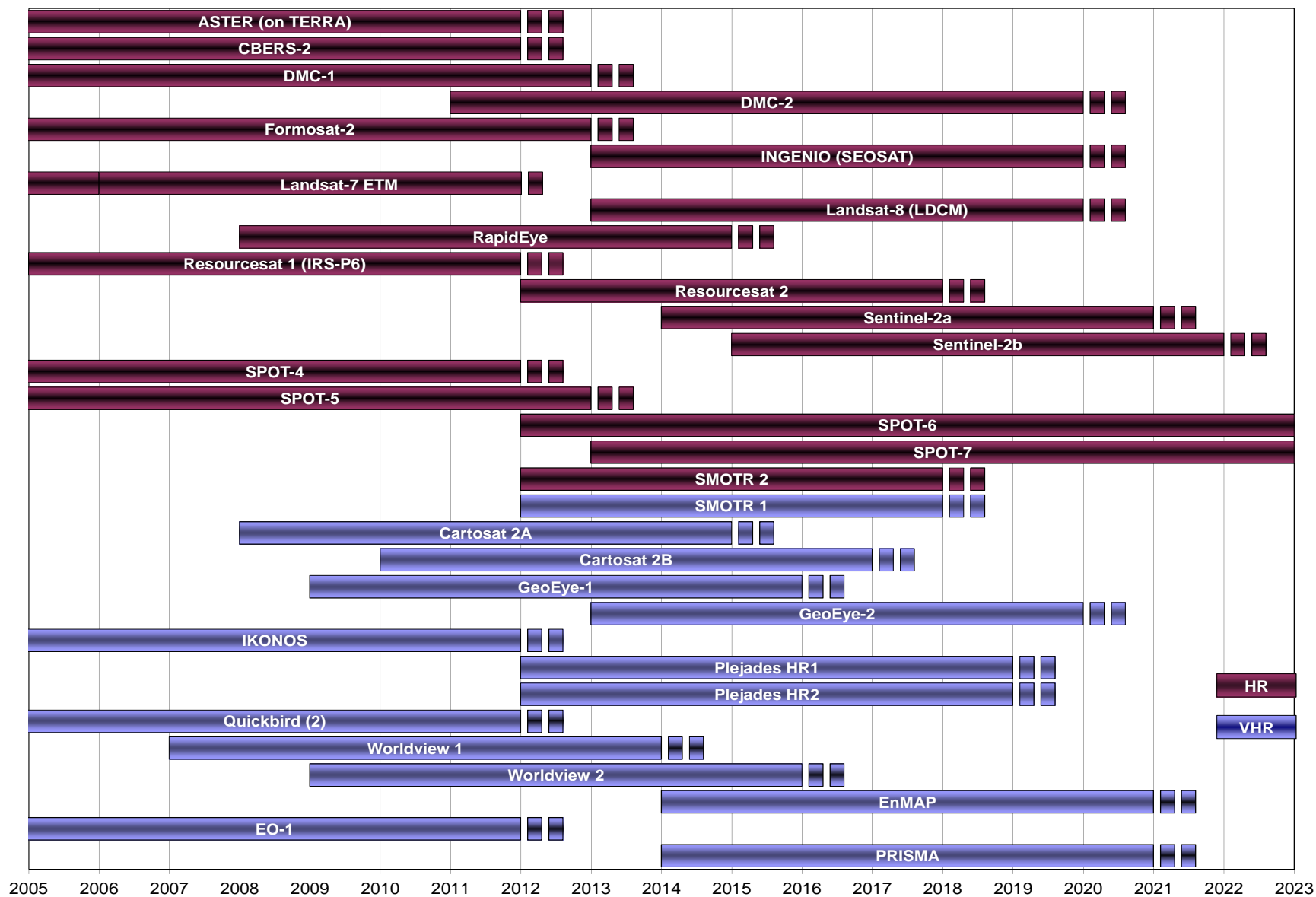
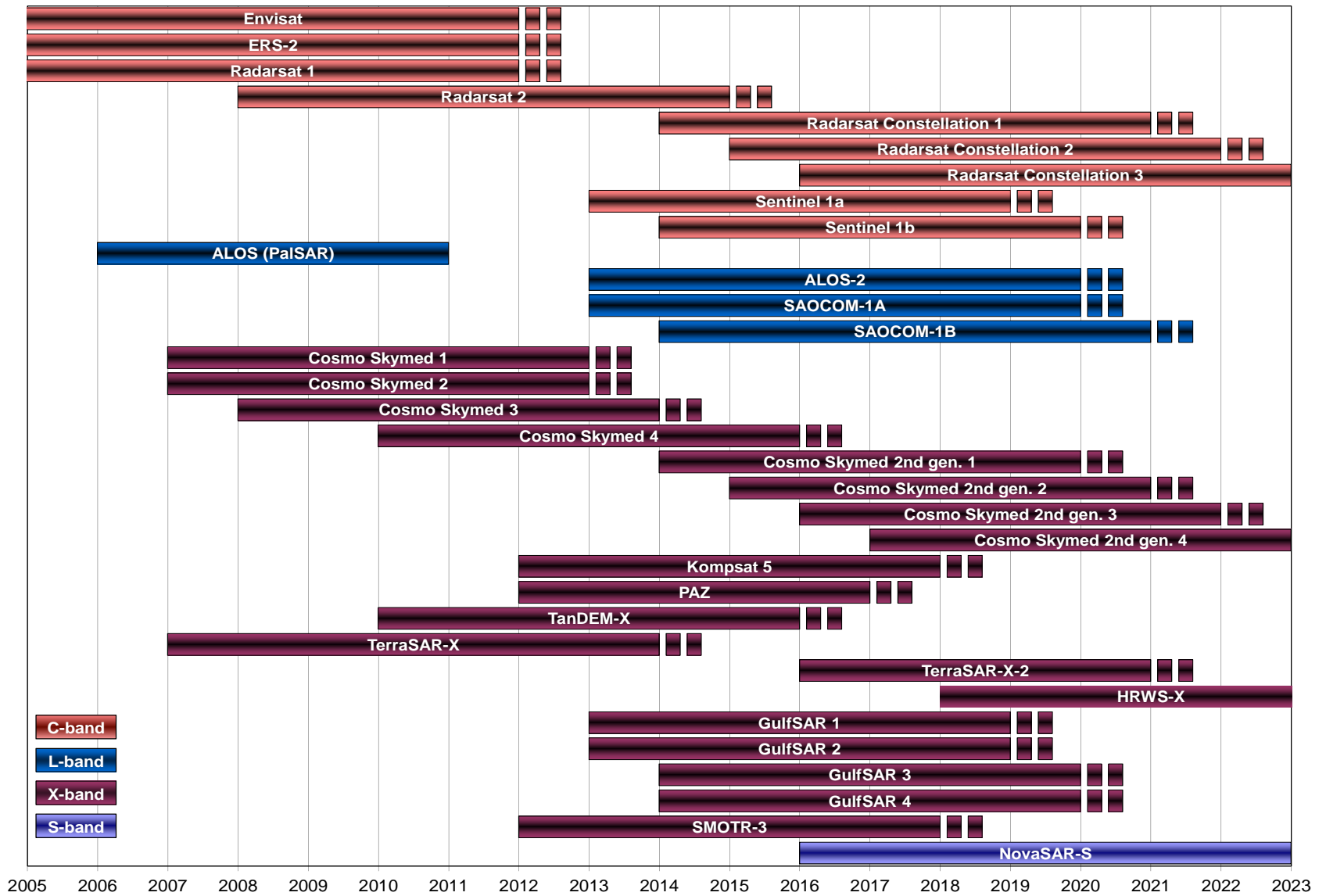


Figure 1-2: Recent and future earth observation SAR satellite missions.



Vegetation development during the growing period is based on physical and biochemical processes which interact with environmental conditions such as atmosphere or soil (Kumar et al. 2003). The material-specific characteristics of objects (e.g. vegetation) determine the interaction of incoming radiation and the object. Based on these characteristics, the incoming radiation is either reflected or absorbed, or penetrates the object. The illumination source can be the solar radiation or in case of an active system the sensor itself (Albertz 2009). As remote sensing sensors measure the electromagnetic radiation reflected by an object, one can infer the physical properties of the object. In vegetation science, spectral algorithms such as vegetation indices were developed to extract biophysical parameters based on differential absorption, reflectance and transmittance of energy (Lyon et al. 1998).

In terms of agriculture, satellite remote sensing enables the acquisition of information that is essential for modern crop monitoring since large areas can be monitored with different sensor systems at regular intervals. The contribution of remote sensing to crop monitoring can be as follows:

- Land cover mapping. Land cover and land use mapping are among of the most important contributions of remote sensing to agricultural monitoring. Inventory map are used for assessing the dynamic change in an agricultural environment (Ran et al. 2010).
- Crop status monitoring. As reflected or backscattered energy from vegetation changes with changing plant phenological stage, remote sensing can be used to monitor plant development during the growing season (Albertz 2009).
- Crop growth modelling. Spatial remote sensing data can be linked to crop growth models to calibrate or re-initialize crop models on the one hand, or to upscale local simulations to a regional level (Dente et al. 2007).

1.4 Objective and Hypotheses

Although there are manifold recent and future earth observation missions, area-wide remote sensing based crop monitoring is still not implemented. To support crop monitoring systems by remote sensing, it is essential to acquire data at specific phenological stages to extract information that is relevant for agricultural monitoring. Furthermore, multi-temporal remote sensing acquisitions improve monitoring during the growing season in terms of land cover mapping, crop status monitoring and the calibration of crop growth models. Beside the cost component, factors that could prevent a timely monitoring are: availability of acquisition capacity, cloud cover problems or lack of appropriate methodologies for a synergistic use of different sensor systems. Thus, it is necessary to develop methodologies to retrieve biophysical information from different sources (multispectral, hyperspectral, microwave) which can be used to supply agricultural monitoring systems. Within this thesis, optical and SAR sensors for monitoring were under investigation to validate the advantages and synergies of the different systems. Especially the new generation of X-band SAR sensors offer new capabilities for crop monitoring, but up to now only a few number of research papers on rice crop monitoring based on space-borne X-band data has been published. Based on this, specific research objectives were identified that are subdivided into four parts:

Multispectral and Hyperspectral Remote Sensing

- to quantitatively describe hyperspectral reflectance signature of winter wheat canopy during the vegetation period
- to analyse, compare and evaluate satellite based multispectral and hyperspectral images in terms of broad band and narrow band vegetation indices for the estimation of winter wheat aboveground biomass, plant N concentration and plant height. It is assumed, that advanced narrow band vegetation indices perform better than standard vegetation indices based on multi-spectral data. Three different types of vegetation indices will be evaluated.

- standard broad band vegetation indices derived from multispectral sensor ALI
- standard narrow band vegetation indices derived from hyperspectral sensor Hyperion
- systematic identification of best waveband combinations in the Hyperion reflectance spectrum from 400 to 2500 nm
- to investigate the ability to predict crop standing biomass by different vegetation indices

C-band microwave remote sensing

- to quantitatively describe C-VV SAR backscattering of winter wheat canopy during the vegetation period
- to investigate the ability to predict crop standing biomass by Envisat ASAR

Synergy of Hyperspectral and C-band microwave remote sensing

- to explore the potential of complementary use of SAR and hyperspectral data for mapping crop and field conditions at a regional level

X-band microwave remote sensing

- to assess the potential of high-resolution and multi-polarization X-band SAR data in agricultural monitoring
- to study the sensitivity of X-band co-polar backscatter as a function of rice phenology stages based on multi-temporal acquisitions and different incidence angles
 - to evaluate the relationship between X-band co-polar backscatter and biomass of the different scattering layers (stem, leaf, and head)
 - to analyse to benefit of dual polarimetric X-band data for crop growth status monitoring

2 LITERATURE REVIEW

This chapter introduces the essential basics of multispectral and hyperspectral imaging, SAR systems, and agricultural vegetation. The section 2.1 serves as an introduction to the field of multispectral and hyperspectral data properties and its applicability to crop monitoring. The second section (2.2) deals with the description of the SAR system parameters, with the properties of imaging radar such as radiometry, geometry, and the monitoring of crop by microwave radiation.

As multispectral and hyperspectral remote sensing has been known well for decades and described in many review papers and textbooks such as Thenkabail et al. (2011), Kumar et al. (2003), Mulla (2012) and Schowengerdt (2007), the introduction to this topic is rather short and will only address elements that are of main importance for the recent study. Due to this, the focus of the literature review is put on radar and especially on polarimetric radar remote sensing.

2.1 Multispectral and Hyperspectral Imaging

Optical remote sensing records image data in different wavelength ranges across the visual and infrared part of the electromagnetic spectrum. If image data is captured simultaneously at several frequencies, it is called multispectral imaging. Usually the electromagnetic spectrum is sampled in dedicated wavelength bands, whereas each of these bands covers a wide frequency range. Compared to this broad-band sampling of dedicated wavelength ranges with low spectral resolution, multispectral imaging offers the opportunity to acquire high spectral resolution and narrow-band image data continuously across the electromagnetic spectrum (Albertz 2009).

2.1.1 Reflectance Properties

For biochemical processes of plants the main source of energy is the incoming solar radiation. Solar radiation is the driver of photosynthetic processes, where energy is converted to organic compounds. The interaction of the incident electromagnetic

radiation with objects of the surface can be divided into the main processes: absorption, transmission and reflectance (Kumar et al. 2003). Absorption describes a process in which energy of the incident radiation is taken by the pigments of the plants. The process of transmission, in turn, illustrates the passing of electromagnetic radiation through the vegetation without reflection or absorption. Furthermore, there is the surface reflection, whereas the incident illumination is reflected from the surface of the object. The reflectance spectrum is a function of absorption and scattering processes, determined by the biochemical composition, water content, incidence angle and geometrical characteristics of the canopy (Borengasser et al. 2007). The optical properties of the stand are therefore a complex combination of these parameters. They provide compositional information about the vegetation in the visible (VIS), near-infrared (NIR) and short wave infrared (SWIR). The reflectance curve of green vegetation has a characteristic shape from the VIS to the SWIR and is determined by vegetation attributes (Thenkabail et al. 2011).

The **VIS** range (400 to 700 nm) of vegetation reflectance spectrum is determined by strong absorption of foliar pigments, whereas reflectance and transmittance of energy is very low. Most of the energy is absorbed by chlorophyll *a* and chlorophyll *b* in the blue and red light of the spectrum; lower amounts of energy of the blue light are also absorbed by carotenoids (Lillesand et al. 2008). The slightly lower absorption in the green light induces a small reflection peak in the visible portion of the spectrum. The absorbed light of the VIS is used for electron transitions. The liberated energy of this transition is then used for photochemical reactions. With the senescence of the plants the reflectance behaviour changes due to chlorophyll degradation which results in an increase of red light reflectance (Kumar et al. 2003). The transition zone between the VIS and **NIR** is called the **red edge zone** (between 680 and 750 nm) and is characterized by a steep reflectance slope from the low chlorophyll reflectance to the high reflectance of the red edge shoulder. Especially the red edge inflection point, where the slope is at its maximum, is an important indicator for chlorophyll content (Mulla 2012). Due to the lower energy level of the NIR light compared to the visible range, most of the light is reflected or transmitted and not absorbed by the pigments. The reflectance curve is mainly determined by the internal structure and anatomy of the

leaves and the water content. In the NIR, part of the incoming light is transmitted by the first leaf layers and reaches a subsequent layer. This layer also reflects and transmits the light. As a result of the multilayer structure of a vegetation canopy, the total reflectance is an addition of multiple leaf layers (Kumar et al. 2003). Within the NIR range, there are two weak water absorption bands around 970 and 1200 nm. The **SWIR** is dominated by water absorption bands that are centred at 1200, 1450, 1940 and 2400 nm. Compared to this, the absorption of foliar pigments is insignificant, especially in fresh leaves (Schowengerdt 2007).

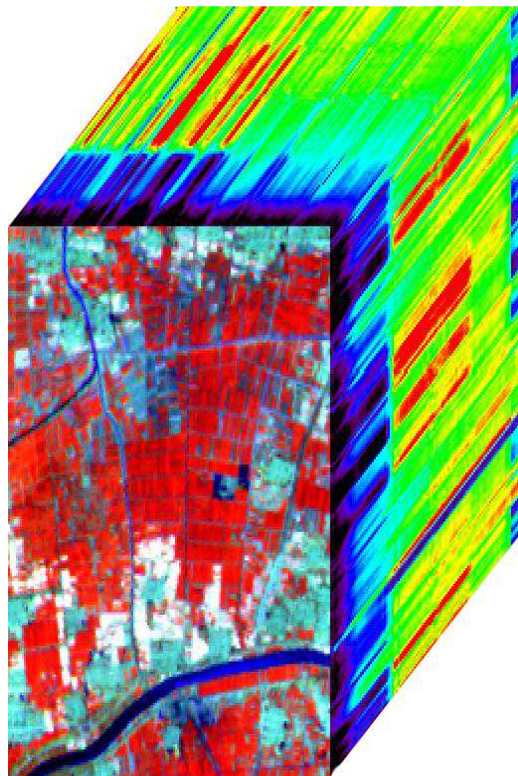


Figure 2-1: Hyperspectral image cube of EO-1 Hyperion extracted over the study site in Huimin County.

Hyperspectral imaging provides the opportunity to image the surface in a high number of narrow spectral bands to provide a continuous spectral curve. Figure 2-1 shows a 3D image cube of one test site of the study (Huimin County). The hyperspectral image cube is a three dimensional representation of the area; it emphasizes the high spectral resolution. The short wavelengths are displayed close to the border of the image plane, whereas to the back of the cube the wavelengths are increasing.

Figure 2-2 shows two average reflectance curves extracted from the test area. The first curve represents typical soil, the second a typical vegetation reflectance curve.



Figure 2-2: Typical reflectance curves (soil and vegetation) extracted from EO-1 Hyperion of Huimin County (April 19, 2006).

2.1.1.1 Atmospheric Effects

Hyperspectral imaging spectrometers acquire data in contiguous bands over a wide range of the electromagnetic spectrum in a passive way. The sun is the illumination source and the solar irradiance curve shows a decreasing trend with increasing wavelength. The recorded at-sensor-radiance curve in general follows the solar irradiance curve. Additionally, the measured at-sensor-radiance is affected by interactions of the atmosphere with the incident and reflected solar radiation (Gao et al. 2009). The illuminated and reflected energy is scattered and absorbed by atmospheric gases and particles which influences the measured energy that is reflected by the object and received by the instrument (Thenkabail et al. 2011). Major absorption features, approximately centred around 1400 nm and 1900 nm. They are caused by water vapour and carbon dioxide and diminish incoming and reflected solar radiation almost completely. Minor absorption bands that reduce the at-sensor-radiance are centred at 700 nm (O_2), 940 nm and 1140 nm (H_2O) and 2000 nm due to

the occurrence of carbon dioxide (CO₂) (Borengasser et al. 2007). Absorption elements causes distortions on the recorded radiance includes also ozone (O₃), carbon monoxide (CO), and methane (CH₄). All these absorption features affect the transmittance through the atmosphere in a range between 400 nm and 2500 nm. In contrast to absorption features reducing the amount of recorded energy, scattered light (path radiance) is added to the radiance measurement. Scattering processes that occur within the atmosphere are Rayleigh scattering in the case of smaller particles compared to the wavelength, Mie scattering of particles in size of the wavelength and not specified scattering on droplets (Gao et al. 2009). The total radiance measured at the sensor (L_{tot}) consists of direct reflection from the object and diffuse atmospheric scattering and can be expressed as follows (Lillesand et al. 2008):

$$L_{tot} = \frac{pET}{\lambda} + L_p \quad (2.1)$$

where p is the reflectance of an object, E the irradiance of an object, T the transmission of the atmosphere, λ the wavelength and L_p the path radiance.

2.1.1.2 Radiance and Reflectance

For hyperspectral imaging, radiance is an important parameter since it is measured by the optical instrument. Radiance is the total reflection or emission from a diffuse area and its unit is Watts per steradian per square meter ($W \cdot sr^{-1} \cdot m^{-2}$) when measured per unit wavelength (Borengasser et al. 2007). In the case of an optical instrument carried by a satellite, the electromagnetic energy has to pass the atmosphere. Within the atmosphere, the emitted or reflected light from the observed target is scattered or absorbed which will influence the measured radiance (Gao et al. 2009). The radiance values are therefore dependent on illumination intensity and direction. Compared to this, reflectance spectra are defined as the ratio of amount of light reflected from a target to the amount of incident light. This explains why the reflectance is independent from illumination. Spectral reflectance is unitless and ranges between 0 and 1.0 (Lillesand et al. 2008).

2.1.2 Hyperspectral Crop Monitoring*

Timely monitoring of crop growth status is important for dynamic in-season site specific crop management, detection of plant vitality, assessment of seasonal production as well as environmental pollution control and yield prediction (Miao et al. 2009, Laudien & Bareth 2006, Zhao et al. 2004, Hansen & Schjoerring 2003). Traditional techniques for the measurement of accurate crop parameters such as plant aboveground biomass and nitrogen concentration are destructive, extremely cost and labour intensive, and not able to provide spatial distributed data on regional level (Lu 2006). The estimation of these parameters can be done more efficiently by non-destructive spectral reflectance observations (Daughtry et al. 2000), obtained from field-, airborne- or satellite based sensors. For the linkage of crop parameters with spectral reflectance measurements, a lot of different vegetation indices were developed (Zhao et al. 2004, Haboundane et al. 2004, Broge & Mortensen 2002) that are based on the understanding of reflectance behaviour. Vegetation indices obtained from spectral reflectance measurements are designed to enhance the vegetation cover signal while minimizing the response of various background materials (Schowengerdt 2007). They are mainly based on the difference between low reflection due to strong absorptions by foliar pigments in the red spectrum and high reflection of structural components (cell walls) in the near infrared spectrum (Kumar et al. 2003, Lillesand et al. 2008). In the past decades, many attempts have been made to estimate crop parameters at regional level, either directly from remote sensing data or by assimilating remote sensing data into crop models (Schneider 2003). A lot of earth observation satellites carrying multispectral imaging sensors (Wooster 2007), which provide data that can be used for the calculation of broad band vegetation indices (Liu 2006). Vegetation indices calculated from the visible and near infrared bands of multispectral scanners have been used to estimate crop parameters such as standing biomass and grain yield (Tucker 1979, Thenkabail et al. 2000, and Doralswamy et al. 2003), leaf area index (LAI) (Cloutis et al. 1999) and plant nitrogen content (Reyniers & Vrindts 2004). At higher vegetation densities, standard broadband vegetation indices,

* This section is an extended version of the article: Koppe et al. (2010a).

such as Simple Ratio (SR) or Normalized Difference Vegetation Index (NDVI) are generally less accurate (Jongschaap & Schouten 2005) and tend to saturate (Haboudane et al. 2004, Mutanga & Skidmore 2004), which results in a limited prediction value of crop parameters when LAI exceeds two (Haboudane et al. 2004). Improvements could be achieved by using hyperspectral radiometers, which can acquire a continuous electromagnetic spectrum for each pixel between 350 and 2500 nm (Hansen & Schjoerring 2003). The sensitivity of hyperspectral vegetation indices for estimation of crop parameters has already been demonstrated with significant improvements compared to broad bands by several authors during the past several decades (Fillela et al. 1995, Strachan et al. 2002). A selection of standard vegetation indices used for analysing and monitoring of spatial and temporal variations of vegetation stands are summarized in Appendix A.1. Beyond narrow band standard vegetation indices, imaging spectroscopy provides the opportunity of using more adequate wavebands or waveband combinations to estimate biophysical parameters (Ceccato et al. 2002). According to this, different approaches for index calculation based on all waveband combinations were developed and successfully used for estimation of wheat grain yield (Xavier et al. 2006), wheat biomass and Nitrogen content (Hansen & Schjoerring 2003, Thenkabail et al. 2000) as well as land cover classification (Thenkabail et al. 2004). Also, Ferwerda et al. (2005) used waveband selection method successfully for the estimation of leaf nitrogen content across different species. Mutanga & Skidmore (2004) reported, that waveband combinations different from the standard NDVI could overcome saturation effects of biomass estimation at full canopy cover. Narrow band vegetation indices other than standard NDVI were successfully used for biomass and nitrogen estimation of winter wheat in the Northern China Plain (Koppe et al. 2010a); whereby the saturation effect at full canopy cover was reduced. Improvements concerning plant parameter estimation with different waveband combinations were also reported by Thenkabail et al. (2000). However, Darvishzadeh et al. (2008) and Jamer et al. (2003) demonstrated that biophysical parameters could be better estimated by multivariate methods such as partial least square regression because 2-channel vegetation indices make only use of a small subset of the available spectral information. Beside the advantages and

robustness of vegetation indices for biomass estimation, a drawback is the necessity of reference data for model calibration. Alternative and more complex quantification approaches are physically based radiative transfer models (Cho et al. 2008). These models simulate the hyperspectral signature and remotely sensed data can be used for model recalibration (Richter et al. 2009).

A lot of studies have been conducted on improving the performance of hyperspectral vegetation indices both on excised leafs and in situ measurements, but there are only a few studies dealing with hyperspectral imaging on regional level (e.g. Smith et al. 2003, Galvão et al. 2005, Datt et al. 2003). By using high spectral resolution space born radiometers (e.g. Hyperion sensor on Earth Observation-1 satellite), detailed variation in the electromagnetic spectrum between 400 and 2500 nm can be measured over a wide area (Broge & Leblanc 2000), making this approach more efficient for large scale precision crop management.

2.2 Synthetic Aperture Radar

Microwave systems can be distinguished on a general level into active and passive instruments. Because this thesis focuses on active imaging RADAR (Radio Detection and Ranging) systems, properties of passive systems will be neglected.

Active radar systems illuminate a target area with electromagnetic energy by sending microwave pulses at a certain rate. This rate is named the pulse repetition frequency (PRF). The transmitted signals are scattered at the surface by the different targets and their echoes are recorded with the antenna (Woodhouse 2006). The returning echoes provide information about magnitude, phase, polarization and Doppler frequency of the target. The time delay of the received microwave pulses provide the two-way travel time and hence the distance from the antenna to the target. In general, the earth surface is illuminated by the transmitted pulses perpendicular to the flight direction (range) while the satellite is moving along its orbit path (azimuth). The resulting image is composed by the motion of satellite passing by the area being covered (Massonnet & Souyris 2008). Space-borne imaging radar systems are so called “side-looking systems” in contrast to radar altimeters which have a nadir look

direction. The side-looking geometry allows the spatial separability of backscattered signals which is essential for a two-dimensional representation of the target area (Bamler & Schättler 1993). The resolution of the side looking system in range and azimuth is defined by the bandwidth of the transmitted pulse and the antenna length, respectively. Since the azimuth resolution strongly depends on the distance to the target for systems with a real aperture, real aperture radar (RAR) systems are not appropriate for high altitudes. To overcome low azimuth resolution, a synthetic aperture radar (SAR) can be formed by using the satellite's motion along the orbit path. As the moving platform passes by the area being covered pulses are reflected from a given target. These distinctive coherent signal-variations (Doppler spectrum variations) can be processed to obtain a higher azimuth resolution (Klausing & Holpp 2000). The imaging geometry of a SAR system is generalized in Figure 2-4.

2.2.1 SAR System Parameters

2.2.1.1 Frequency

Conventional radar remote sensing systems utilize frequencies between 0.3 GHz and 30 GHz, which corresponds to a wavelength between 1 and 70 cm. Frequency and wavelength are related to each other as follows (Henderson & Lewis 1998):

$$\lambda = \frac{c}{f} \quad (2.2)$$

where λ is the wavelength, c the speed of light and f the frequency (Woodhouse 2006). The inter-relationship between frequency and wavelength is provided in Figure 2-3. The radar systems are classified into different wavelength-frequencies bands with a letter code according to IEEE-Std-521-1976 (Henderson & Lewis 1998). Typically used wavebands of space-borne SAR systems are X-, C- and L-band.

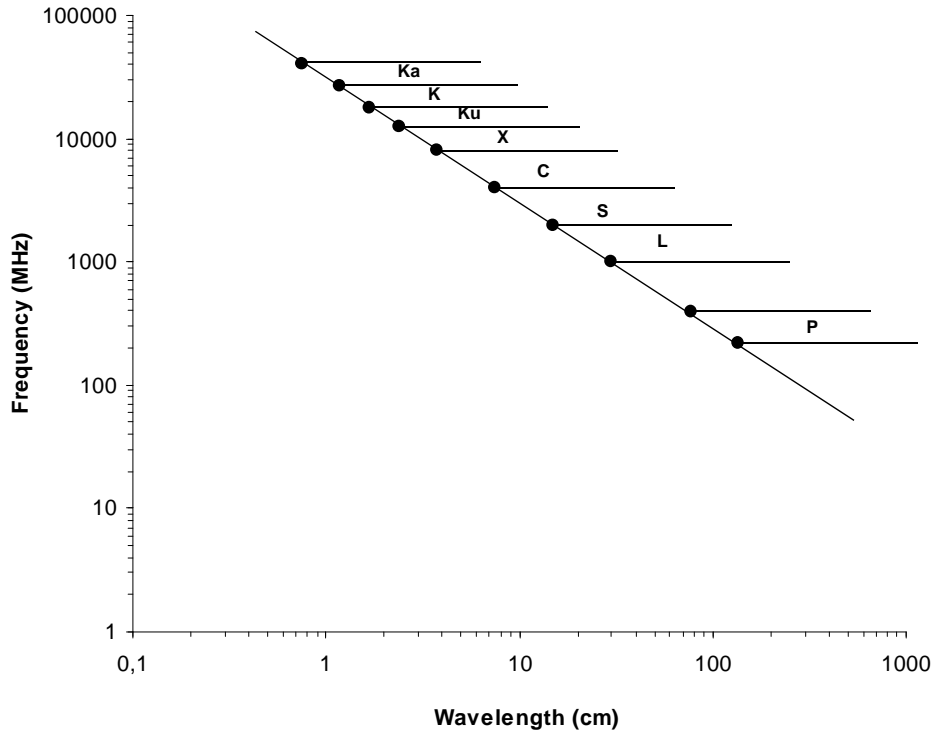


Figure 2-3: Inter-relationship between wavelength and frequency for the most common SAR systems on a log scale (modified after Henderson & Lewis 1998).

2.2.1.2 Radar Equation

The radar equation describes the fundamental physical relationship between radar system parameters, transmitted and received power from the target, and propagation properties of the electromagnetic wave (van Zyl 2011). The power density P_r represents the energy per unit area of an active radar system backscattered from a target at ground. The radar equation is a general equation since it does not consider polarization characteristics. Furthermore it is limited to surface scattering and radar cross section is not confined to a particular target type (point or distributed target) (Ulaby et al. 1986).

$$P_r = P_t(\sigma^0 A) \left(\frac{G^2 \lambda^2}{(4\pi)^3 R^4} \right) \quad (2.3)$$

where P_t is the power transmitted, G the gain of the antenna, λ the wavelength of the radar system, A the target's receiving area, R the range distance from the antenna to the target and σ^0 is defined as the radar cross section per unit area. The term $1/4\pi R^2$ involved in the denominator is the spreading loss, which is defined as the power density reduction around the antenna over a sphere with the radius R (Ulaby 1989).

2.2.1.3 Range and Azimuth Resolution

For interpretation of microwave imaging data, an understanding of parameters determining the resolution is fundamental since it is quite different compared to optical systems. The resolution of side looking radar systems (SLAR) can be distinguished into the directions parallel (azimuth or along track) and perpendicular (range or across track) to the flight path. The resolution in a SAR image is defined by the separability of adjacent objects in either azimuth or range direction (van Zyl 2011).

The range resolution can be divided into slant range and ground range resolution and is directly linked to the transmitted pulse length. The resolution for slant range R_{sl} is as follows (Klausing & Holpp 2000):

$$R_{sl} = \frac{c \cdot \tau}{2} \quad (2.4)$$

where τ is the duration of transmission and c is the speed of light and the denominator accounts for two-way travel time of the wave. According to equation 2.4, a shorter pulse length, which is a product of c and τ , implies a finer resolution in range. But coinciding with the reduction of the pulse length the total energy illuminating earth's surface is diminishing, too.

This requires a trade-off between resolution and strength of the signal. Compared to the constant slant range resolution R_{sl} from near to far range, the ground range resolution R_{gr} is variable across the range direction. To calculate ground range resolution R_{gr} , the denominator of equation 2.4 is amended by the sine of the look angle θ ; i.e. ground range resolution improves with increasing slant range distance (Maitre 2013).

$$R_{gr} = \frac{c \cdot \tau}{2 \sin \theta} \quad (2.5)$$

As already stated earlier in this chapter, the limited azimuth resolution of RAR systems can be overcome by the synthetic lengthening of the real antenna. With the motion of the satellite along the orbit path, several echoes of a target are received at different positions of the synthetic aperture (Massonnet & Souyris 2008). During SAR processing, the different signals of a dedicated target are composed by using the

recorded Doppler frequency of each signal. The azimuth resolution A of a SAR system is defined as (Klausing & Holpp 2000):

$$A = \frac{L}{2} \quad (2.6)$$

where L is the antenna length. This means, that the azimuth resolution is constant and independent from sensor height and slant range distance. The shorter the real antenna, the longer the synthetic antenna and hence the better the azimuth resolution (Henderson & Lewis 1998).

2.2.2 Properties of Imaging Radar

2.2.2.1 Speckle

Speckle is an unwanted and dominating noise that degrades SAR images interpretation capabilities. SAR is a coherent imaging technology, recording both the amplitude and the phase of the back-scattered radiation. Because of this, it suffers from a noise-like phenomenon known as speckle. Each resolution cell of the system contains many scatterers; the phases of the returned signals from these scatterers are randomly distributed and speckle is caused by the resulting interference. Based on this, the image has a grainy appearance. This imposes a significant limitation on the accuracy of the measurements that can be made: the brightness of a pixel is determined not only by properties of the scatterers in the resolution cell, but also by the phase relationships between the returns from those scatterers. In single-look images, the uncertainty is equal to the expected value (Klausing & Holpp 2000).

To reduce this noise for automatic image processing and interpretation a lot of speckle filters were designed to enhance scene texture elements. Regarded physically, the speckle is based on constructive and destructive interference due to multiple scattering within a resolution cell. The pattern of the speckle appearance in the image is chaotic and not predictable. The total backscatter of each resolution cell of a distributed target is the coherent sum of these many individually reflected signals (Woodhouse 2006).

2.2.2.2 Image Geometry and Geometric Distortions

As a basis for discussion of imaging geometry and distortion effects, the most important names and parameters characterizing a side looking SAR system are shown in Figure 2-4.

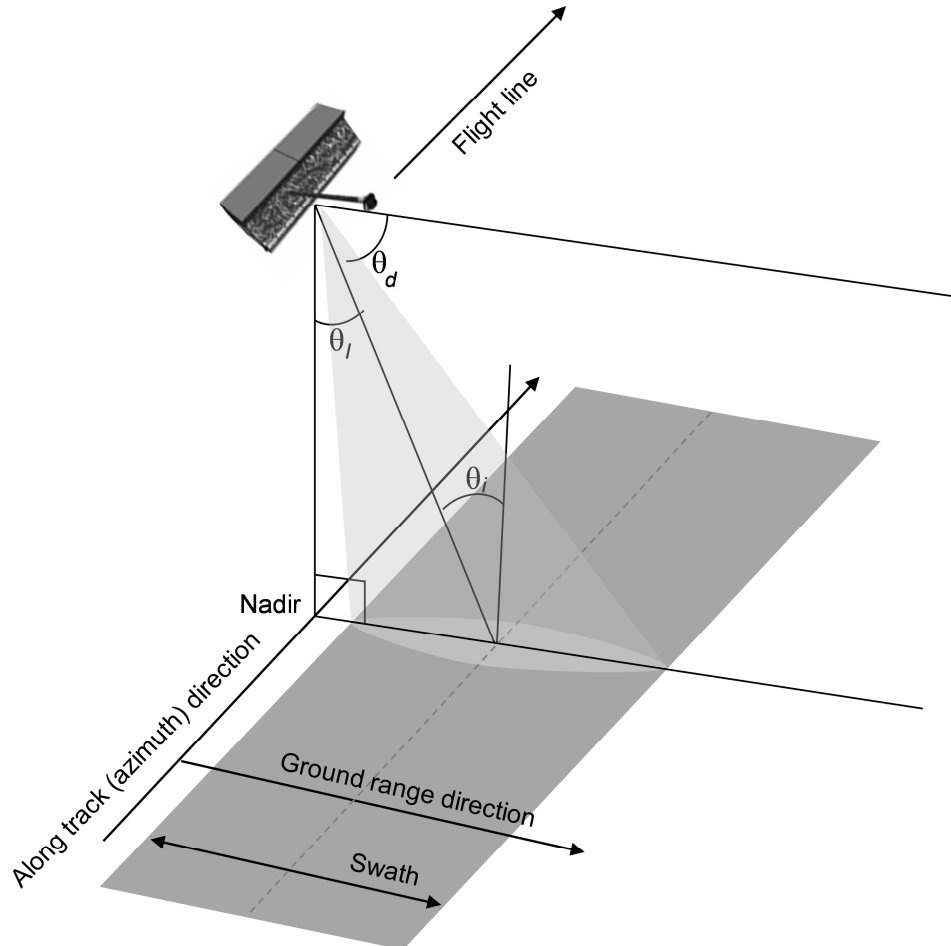


Figure 2-4: Imaging geometry of side looking SAR (modified after Woodhouse 2006).
 θ_l is the look angle, θ_d is the depression angle and θ_i the incidence angle.

Due to the side-looking geometry of spaceborne SAR systems, radar images show geometric distortions depending on the terrain such as foreshortening, layover and shadow. For flat areas these distortions are irrelevant and the link between slant and ground range can be described by equation 2.5.

With the appearance of mountainous terrain within the illuminated area, the imaging geometry becomes more complex and results in the mentioned local distortions (Massonnet & Souyris 2008).

As the slant range distance between sensor and target is measured as a function of time, all targets with equal travel times are located on the same range circle around the satellite. Depending on the relief, different targets with varying ground range distances could have the same slant range distance. The effect of **foreshortening** means the shortening of distances of terrain slopes facing the sensor in the radar imagery. It can be observed in all cases if the local incidence angle is lower than 90° . Only if the local incidence angle is 90° , the imaged slope length is the same as the length of the real terrain, taking image scaling factor into account. The effect of foreshortening can be corrected by means of orthorectification which uses elevation information (Oliver & Quegan 2004).

Layover in SAR images occur as an extreme case of foreshortening if the incidence angle is lower than the terrain slope facing the satellite. In this constellation, the top of a mountain has a shorter slant range distance than the bottom and is consequently recorded earlier which results in an inverse terrain geometry. As a third geometric ambiguity **shadow** areas can occur as a consequence of missing radar illumination of back-slopes due to occlusion by the terrain features. The relationship between incidence angle (θ), angle of the backslope (α) and occurrence of radar shadow (S_r) in the image can be described as follows:

$$S_r: \text{if } (90 - \theta) < \alpha \quad (2.7)$$

In the case of steep terrain or dense urban areas with high buildings, all three types of distortions are related to each other and may mask one another (Oliver & Quegan 2004).

2.2.2.3 SAR Interaction with the Target

The interaction of a SAR signal with a target on earth surface is affected by several factors. As the study is about agricultural monitoring, the main focus is set on the interaction with a vegetation canopy. In the following only the impact on target interaction is pronounced, due to the system parameters already described. Firstly, the system parameters affecting the surface interaction are addressed; subsequently the

scattering mechanisms that are influenced by the target characteristics are discussed in section 2.2.2.4.

Important SAR system parameters which are determining target interaction are **frequency**, **polarization** and **incidence angle** (Oliver & Quegan 2004). **Frequency** is an important parameter, since interaction of wave and plant parts (leaves, branches, stems, etc.) is dependent on wavelength and size of the plant parts. With increasing wavelength, plant scatterers like branches and leaves become smaller in relation to wavelength, which reduces interaction with these targets (Soria-Ruiz et al. 2009) and the target becomes “smoother”. If scatterers are in the size of the wavelength, their contribution to total backscatter of a resolution cell could become significantly dependent on shape and orientation of the plant parts. In general, lower frequencies like L- and P-band are more suitable for subsurface monitoring since they penetrate deep through the vegetation and the soil component is emphasized in total backscatter. Higher frequencies like X-band are attenuated within the vegetation volume and the signal is mainly backscattered from the canopy. Penetration characteristics also depend on the dielectric properties, which in turn is a function of water content. Moisture content determines the dielectric constant of the vegetation. Assuming the same vegetation moisture content, the reflected energy from the target varies with different frequencies (van Zyl 2013).

Also an important factor when discussion target interaction is the transmitted and received **polarization**, which determines the orientation of the electric field. The combination of transmit and receive polarization affect the target interaction and hence the energy scattered back to the sensor (Mott 2006). The orientation of the vegetation is important as vertically oriented plants attenuate vertically polarised waves to a higher degree than horizontally oriented waves do. Multi-polarization (dual-polarimetric, quad-polarimetric) provides additional information about the vegetation and can improve interpretation and analysis (Mott 2006).

A third system parameter which is subject of the study is the **incidence angle** of the incoming illumination. Especially for the interaction of microwaves with an agricultural environment the relationship between geometry of crop features and SAR geometry is important. Depending on the viewing geometry of the SAR system different vegetation

layers or soil components are pronounced since the path length through the vegetation volume is varying. Steep incidence angles minimize the path length within the vegetation whereas also the attenuation is minimized. Attenuation is based on the extinction coefficient κ_e , which is a function of multiple scattering κ_s and absorption κ_a (Henderson & Lewis 1998):

$$\kappa_e = \kappa_a + \kappa_s \quad (2.8)$$

With increasing incidence angle, the path length within the vegetation increases and hence the multiple scattering diminishes. Such a viewing geometry pronounces canopy backscatter.

2.2.2.4 Scattering Mechanism

The understanding of the signal-target interaction (scattering mechanism) is essential for interpretation of environmental information extracted from the backscattering. In general, the scattering of the target can be divided into surface, double bounce and volume scattering (Henderson & Lewis 1998). In the case of **surface scattering** the radar wave is reflected from the surface.

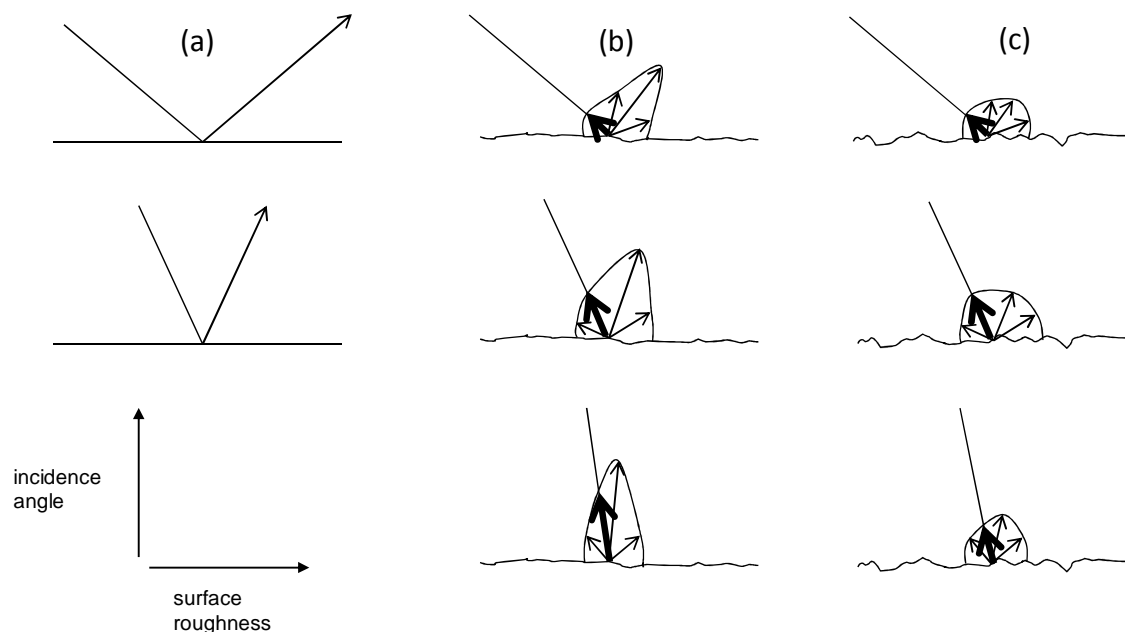


Figure 2-5: Backscatter as a function of surface roughness (after Woodhouse 2006).

One of the most important target characteristics affecting the backscattering coefficient is the **surface roughness** (Richards 2009).

The magnitude of radar backscatter of a rough surface is strongly dependent on the degree of roughness, wavelength and partially on the look angle of the SAR system. To neglect system parameters, the influence of roughness on radar backscatter is shown in Figure 2-5. In case of a smooth surface (Figure 2-5a), the energy is reflected away from the illumination source in a specular reflection manner. The reflection angle is similar to the incidence angle of the incoming wave and the reflection can be labelled as coherent. An increase in roughness of the surface (Figure 2-5b) increases also the diffusivity of the backscattered energy and the behaviour is less predictable (Massonnet & Souyris 2008). The backscattered energy has a coherent and a scattered (diffuse) component. In the case of an isotropic or Lambertian surface, the influence of the incidence angle approaches zero and the energy is reflected more or less equal in all directions. As mentioned previously, the consideration of a surface roughness depends on wavelength and incidence angle. The approximations whether a surface is considered as rough are manifold. The “rule of thumb” defines the roughness by $\lambda/10$ (λ is the wavelength). According to the rule of thumb, systems with higher frequencies are more sensitive to surface roughness. The Rayleigh criterion approximates the surface as a diffuse scatterer and relates wavelength and the local incidence angle for modelling the average height variations (Henderson & Lewis 1998). The surface is considered as rough if

$$h_{rms} > \frac{\lambda}{8 \cdot \cos \theta} \quad (2.9)$$

where h_{rms} is the root mean square of the height variation, λ is the wavelength and θ is the local incidence angle (Woodhouse 2006). For the TerraSAR-X acquisitions in 2009 ($\lambda = 3.14$ cm, $\theta = 39^\circ$, see chapter 3.2) of the Jiansanjia test site (chapter 3.1.2) the surface appears rough in the SAR image if the average height variation of the surface is greater than 0.5 cm. Two smooth orthogonal surfaces act as a dihedral corner reflector if the surfaces are parallel to the flight direction and aligned to the illumination source.

This dihedral reflector permits a **double bounce scattering** with a strong backscatter return to the sensor. In the context of vegetation science and this study, a natural corner reflector is the water surface in combination with the vertical stems of the rice plants (Lopez-Sanchez et al. 2011).

Surface scattering described above occurs only at the boundary surface of two media. If the underlying medium is inhomogeneous such as a vegetation canopy, i.e. consists of different materials and different dielectric properties, the transmitted wave may penetrate into the lower medium (van Zyl 2011). Inside this medium **volume scattering** occurs as the transmitted radar wave is reflected with multiple bounces by multiple components; i.e. it is a scattering in a three-dimensional space compared to a two dimensional space of the surface scattering. The multiple scattering inside the volume causes a loss or attenuation in energy of the transmitted wave, which is referred to as extinction. The extinction consists of scattering losses and conduction losses. Depending on system parameters such as frequency, polarization and incidence angle, as well as target parameters such as density and moisture content, the depth of penetration of the transmitted wave can vary greatly. The amount of energy crossing the border to the upper medium and scattered back to the sensor determines the increase or decrease of backscatter coefficient and hence image brightness (Oliver & Quegan 2004).

Such as the surface roughness, the **dielectric properties** of the target influence brightness of the pixel in the SAR image. The dielectric properties affect the interaction of the electromagnetic wave with the target by influencing the absorption and propagation of the wave. The dielectric constant ϵ is highly dependent on the frequency of the SAR system and the moisture content of the illuminated target. The complex number ϵ can be subdivided into the real ϵ' and imaginary part ϵ'' , whereas the real part is related to the permittivity of the medium and the imaginary part is related to the energy loss within the medium (Klausing & Holpp 2000). Metals and water have a very high dielectric constant compared to other natural dry materials. With increasing moisture content, the penetration depth of the electromagnetic wave into the medium (e.g. vegetation canopy) is reduced and hence the reflectivity is high.

But for a discontinuous vegetation canopy increasing permittivity also increases the volume scattering (Richards 2009).

2.2.2.5 Polarization

As polarization analysis is an important part of the study, polarimetric properties and analysis are discussed in more detail.

Electromagnetic waves can be considered as transversal waves with three vector fields that are mutually orthogonal. The three vectors are the direction, the electric and the magnetic field. Electric and magnetic field oscillate perpendicular to the direction of the wave. The polarised component of the radiation is defined by the electric field, which can be linear, circular or elliptical. In the linear case, the oscillation is a straight line (Mott 2006). Since most common polarization schemes of space-borne SAR systems are linear, circular and elliptical polarization are not treated here. Linear polarised radar pulses are transmitted and received having either displacement in x-direction or in y-direction perpendicular to the direction of propagation in z-direction. X- and y-direction are usually known as horizontally and vertically with reference to earth's positional relationships. As SAR systems are active systems, microwave radiation is transmitted and received. The radar pulses are transmitted either horizontally (H) or vertically (V) polarised and received in the same manner in one of the both polarizations (van Zyl 2011). This allows the mixing of the linear polarizations to provide a quad polarization scheme (HH, HV, VH and VV). There are two like-polarizations (HH and VV) where transmit and receive are filtered in the same plane and two cross-polarization (HV and VH) where transmit and receive are filtered perpendicular to each other. The linear polarization can be effectively represented in a scattering matrix (S), since the echoes are measured orthogonal (Richards 2009):

$$S = \begin{bmatrix} S_{VV} & S_{VH} \\ S_{HV} & S_{HH} \end{bmatrix} \quad (2.10)$$

Each of the elements in this matrix is a complex number which describes amplitude and phase of the transmitted and received signal. The scattering matrix describes the fully polarimetric case; a subset of this matrix would be partially polarimetric, such as

the dual polarimetric case of TerraSAR-X. For the cross polarization terms the radar principle of reciprocity can be invoked ($S_{VH} = S_{HV}$) (Maitre 2013).

Based on the scattering matrix S of full the polarimetric data given in equation 2.10, a 3x3 covariance matrix C can be derived which represents the scattering properties in the power domain. The covariance matrix is a vectorised version of the scattering matrix (Richards 2009):

$$C3 = \begin{bmatrix} |S_{HH}|^2 & \sqrt{2}S_{HH}S_{HV}^* & S_{HH}S_{VV}^* \\ \sqrt{2}S_{HV}S_{HH}^* & 2|S_{HV}|^2 & \sqrt{2}S_{HV}S_{VV}^* \\ S_{VV}S_{HH}^* & \sqrt{2}S_{VV}S_{HV}^* & |S_{VV}|^2 \end{bmatrix} \quad (2.11)$$

Where $*$ denotes the conjugate of the matrix.

The covariance matrix represents the correlation of the elements of the scattering matrix, i.e. they describe the degree of correlation of the co-polarised (HH and VV), like polarised (HH or VV) and cross-polarised (HV or VH) channels (Mott 2006). Based on the covariance matrix, the scattering mechanism of surfaces can be extracted with the help of polarimetric decomposition methods. Beside the covariance matrix, the elements of the scattering matrix S can be vectorized in a different way resulting in the coherency matrix (Richards 2009):

$$T3 = \begin{bmatrix} |S_{HH}|^2 + 2\Re(S_{HV}S_{VV}^*) + |S_{VV}|^2 & |S_{HH}|^2 - 2j\Im(S_{HH}S_{VV}^*) - |S_{VV}|^2 & 2S_{HH}S_{HV}^* + 2S_{VV}S_{HV}^* \\ |S_{HH}|^2 + 2j\Im(S_{HV}S_{VV}^*) - |S_{VV}|^2 & |S_{HH}|^2 - 2\Re(S_{HH}S_{VV}^*) + |S_{VV}|^2 & 2S_{HH}S_{HV}^* - 2S_{VV}S_{HV}^* \\ 2S_{HV}S_{HH}^* + 2S_{HV}S_{VV}^* & 2S_{HV}S_{HH}^* - 2S_{HV}S_{VV}^* & 4|S_{HV}|^2 \end{bmatrix} \quad (2.12)$$

where $*$ denotes the conjugate of the matrix.

The coherency matrix is closely related to the covariance matrix as it contains similar information but in a different expression. Same as in the covariance matrix, its eigenvalues are used in polarimetric decomposition and classification (Mott 2006).

In the context of crop monitoring the characteristics of the horizontally and vertically polarised waves can be used for the retrieval of crop parameters. Depending on the

main orientation of the plants the HH and VV polarization interact in a different way; i.e. the coupling of the waves with the plant elements is more effective if they are aligned in the same direction. For a vertically oriented crop the interaction is much stronger at VV polarization, resulting in a stronger attenuation of the signal and a decreased backscatter (Mattia et al. 2003).

2.2.2.6 Compact Polarimetric Data

Compact polarimetric systems transmit a single polarization and receive two orthogonal polarizations. Compact polarimetric systems do not acquire the full polarimetric state of a target; however, such systems are attractive because of reduced pulse repetition frequency and data rate compared to fully polarimetric SAR systems (Reigber et al. 2008).

Compared to full polarimetric data, in compact polarimetry only one channel (H or V) is transmitted and the two orthogonal polarizations (H and V) are coherently received preserving their relative phase. This relative phase is very important for the further processing of the compact polarimetric data, as the 2x2 covariance matrix can be extracted. The coherent co-polarised 2x2 covariance matrix can be written as:

$$C2 = \begin{bmatrix} |S_{HH}|^2 & S_{HH} S_{VV}^* \\ S_{HH}^* S_{VV} & |S_{VV}|^2 \end{bmatrix} \quad (2.13)$$

It can be seen, that the compact polarimetric case of the covariance matrix is a subset of the covariance matrix of the full polarimetric case (equation 2.11) and is therefore a subject to certain restrictions. However, it is a great advantage to conventional dual-polarised radars such as Envisat, which do not contain the relative phase between the two receiving channels (Raney & Hopkins 2011).

2.2.3 State of the Art SAR Crop Monitoring

Retrieval of crop parameters by microwave remote sensing in a conventional manner is done by using one-dimensional data sets. Referring to the work of Lopez-Sanchez & Ballester-Berman (2009) it is evident that higher dimensionality SAR data is needed to

describe the complex nature. For this purpose higher dimensionality can be achieved by acquiring multi-frequency, multi-polarization, multi-angle or multi-temporal data. Multi-dimensionality increases the number of data layers that can be used for relation to crop parameters (McNairn & Brisco 2004).

2.2.3.1 Rice Crop Monitoring*

As a cereal grain, rice is the most important staple food for a large part of the world. For this reason, monitoring its biophysical variables is valuable for agricultural management and yield prediction. In 2009, about 1.61 million km² of the earth's surface was used for rice cultivation with a global production estimated at 679 million tons (FAOSTAT 2013). Beside its function as source of food, it is also important as a source of income. As population increases in most of the Asian countries, there is a great demand for effective rice monitoring with high reliability (IRRI 2011).

Information extracted from remotely sensed data can assist in estimating key plant growth parameters such as biomass, crop height and leaf area index (LAI). In the past, optical satellite data have been successfully used for rice plant parameter estimation (Tennakoon et al. 1992). For mapping rice cultivation in Asia, time series of vegetation indices (e.g., NDVI) derived from different sensors such as MODIS (Peng et al. 2011) were applied. However, operational crop monitoring and yield prediction based on optical remote sensing is hindered by unfavourable atmospheric conditions, which can lead to data gaps especially during critical growth stages.

As compared to optical sensors, spaceborne Synthetic Aperture Radar (SAR) instruments can overcome inherent limitations of optical systems owing to its all-weather, day and night acquisition capabilities. This allows a more reliable and consistent rice monitoring during the growing season. Especially short wavelength SAR (X- and C-band) interacts with the upper part of the crop canopy, thus offering the potential to retrieve crop biophysical parameters (Ulaby et al. 1984). Compared to this, longer wavelength (L-band) provides a deeper penetration into the vegetation and hence a higher sensitivity to overall plant biomass (Brisco & Brown 1998). To benefit

* This section is an extended version of the article: Koppe et al. (2013).

from both optical and SAR data, there are investigations that use complementary information from both systems, e.g., for crop type mapping (Blaes et al. 2005) or crop condition estimation (Koppe et al. 2010a).

A considerable number of research projects have been set up to investigate the capability of microwave data for agricultural monitoring since the first SAR satellites have been available for scientific and commercial use. Across all frequencies and crop types, the following aspects have been addressed:

- soil moisture retrieval (Gherboudj et al. 2011, Koyama et al. 2010)
- SAR backscatter analysis as a function of crop biophysical parameters and their temporal change (Bouvet et al. 2009, Shao et al. 2001)
- theoretical modelling of backscatter to support interpretation of the observations (Chen et al. 2005)
- development of methods for crop type mapping (Ribbes & Le Toan 1999a, Zhang et al. 2009)
- crop parameter estimation (Karjalainen et al. 2008, Jinsong et al. 2007)
- integration of SAR data in crop growth model for yield estimation (Shen et al. 2009, Ribbes & Le Toan 1999b)

Results of the mentioned studies confirm that microwave backscatter is highly sensitive to different crop types and to changes in the crop canopy due to increasing biomass during the growing cycle. The degree of sensitivity is strongly dependent on the applied polarizations, as identified by quadpol analysis (Wu et al. 2011). Despite good results in crop monitoring, it has to be considered that the recorded SAR backscatter from a vegetated surface is a function of several physical properties. These are crop type, surface roughness, soil moisture, vegetation structure and plant moisture content as well as sensor configuration (e.g., frequency, polarization and incidence angle). Furthermore, the different cultivation practices are important for rice monitoring. Lam-Dao et al. (2009) reported various backscatter behaviours for direct sowing of rice into wet soil in comparison to traditional transplanting techniques. Besides parameter estimation based on direct inversion from the recorded signal or

integrating SAR into growth modelling, there also have been promising results by using repeat-pass SAR interferometric coherence with one day offset for vegetation biomass estimation (Blaes & Defourny 2003). Reasonable results have been already achieved using Polarimetric SAR Interferometry (POLInSAR) for rice biophysical parameter retrieval with indoor wide-band polarimetric measurements (Ballester-Berman et al. 2005). In the near future, Polarimetric SAR Interferometry for crop monitoring with single pass will be demonstrated by the TanDEM-X mission (Hajnsek et al. 2010).

The scattering process and penetration depth into the canopy is highly dependent on the wavelength and the incidence angle (Lim et al. 2007). Inoue et al. (2002) identified typical multi-temporal backscatter signatures of rice for frequencies at around 35, 15, 10, 5 and 1 GHz and at different incidence angles. In terms of electromagnetic interaction between microwaves and canopy, the received radar backscatter is a sum of three main components, including volume scattering, the double bounce scattering from the vegetation–surface interaction and the contribution from the surface itself. At the X-band, experiments conducted by Kim et al. (2000) using ground-mounted scatterometer data have demonstrated that the co-polarised backscatter from a paddy rice field at the beginning of the growing season is dominated by double bounce scattering from the stem–surface (water) interaction. With increasing plant density, the double bounce scattering is replaced by a random scattering from the upper canopy. Inoue et al. (2002) mentioned a typical dual-peak trend for higher frequencies; the first peak at the maximum of double bounce scattering and the second peak with appearance of the top leaf and the heads in top layer of the canopy.

For rice crops, the temporal backscattering behaviour has been extensively reported and understood in a number of studies based on spaceborne C-band data mentioned above. Comparatively to C-band data, much less effort has been put on the use of spaceborne X-band data in rice application. This is mainly due to lack of spaceborne X-band systems in the last decades. With the launch of TerraSAR-X and Cosmo Skymed in 2007, X-band data gained interest for rice monitoring. Lopez-Sanchez et al. (2010) adapted an electromagnetic model to simulate X-band backscatter from rice field. It was used for interpretation of dual-polarised TerraSAR-X images over rice fields in

Spain. Suga & Konoshi (2008) investigated the temporal change of SAR backscatter during the rice growing cycle.

2.2.3.2 Winter Wheat Crop Monitoring*

China cereal acreage and production is one of the most important in the world, with a crop area of about 88 million ha and production estimated at 483 million tonnes in 2009, accounting for ca. 22% of total global production (Fao 2013). The North China Plain is one of the most important cereal production regions in China, accounting for almost 50% of China's winter wheat cultivation (National Bureau of Statistics of China, 2010). In agricultural issues, timely monitoring of crop growth status at an early stage is important for in-season site specific crop management, detection of plant vitality as well as assessment of seasonal production at local and regional level (Miao et al. 2009, Laudien & Bareth 2006).

Since the amount of energy backscattered towards the sensor strongly depends on dielectric properties and surface roughness, it is reasonable that SAR can be used for crop type classification, growth stage mapping and crop condition monitoring (McNairn & Brisco 2004). For different applications, knowledge of the interaction of the surface characteristics with sensor configurations such as resolution, frequency, incidence angle and polarization is of importance (Inoue et al. 2002). For C-Band SAR measurements, many studies dealt successfully with prediction of crop and soil parameters such as biomass, crop height and soil moisture (Brisco & Brown 1998), but the interpretation of the SAR backscatter has proven to be complicated.

In the past, quite a few experiments have been performed on wheat fields, either based on spaceborne SAR sensors or on ground-based scatterometers. Satalino et al. (2009) and Brown et al. (2003) acquired C-band spaceborne and scatterometer data over wheat fields and found that wheat biomass is strongly related to HH/VV backscatter during the whole growing season. The good performance of the HH/VV ratio is due to the differently attenuated vertically and horizontally polarised waves that propagate through a mainly vertical medium of wheat (Picard et al. 2003).

* This section is a modified version of the article: Koppe et al. (2012).

McNairn et al. (2004) differentiated zones of productivity of wheat fields also using scatterometer data. They reasoned that zones of higher productivity had higher backscatter for linear polarizations, with the greatest contrast for HV.

There are also many investigations on wheat's crop parameter retrieval and crop classification based on spaceborne C-band sensors (Baghdadi et al. 2010, Mattia et al. 2003). The results from these studies showed that the backscattering of crops is a complex combination of acquisition parameters (polarization, incidence angle) as well as crop and cultivation characteristics (crop geometry, density, canopy and soil moisture). The combination of these parameters controls the interaction of the incoming electromagnetic wave with the crop canopy and the underlying soil layer.

Because the backscatter is a function of SAR and crop related physical properties, the crop parameter estimation is an inversion of the recorded signal with many unknown parameters. Under consideration of these specifics of interaction, crop parameters related to crop growth could be reproduced by SAR backscatter, such as crop height (Chakraborty 2005), standing biomass (Liu et al. 2006) and LAI (Lin et al. 2009).

2.3 Synergism of Optical and SAR*

Optical remote sensing systems detect solar radiation from the visible and infrared part of the electromagnetic spectrum, which is reflected from different targets on the earth surface. Earth surface elements such as natural and manmade objects have variable reflections and absorptions properties. These object properties generate various spectral signatures captured by the optical instrument, which can be used for object differentiation or surface parameter retrieval. The spectral resolution is depending on the bandwidth and the number of spectral bands used. In contrast to optical systems, SAR is an active system that operates beyond the infrared part of the electromagnetic spectrum in the microwave region. Active illumination of earth surface allows data acquisition at day and night time and the longer wavelength permits data acquisition independently from cloud cover. The longer wavelength of

* This section is an extended version of the article: Koppe et al. (2012).

SAR systems also permits the penetration of the waves into the target such as vegetation canopy or soil (McNairn et al. 2009).

Optical remote sensing is widely used for operational crop type identification and estimation of growth conditions. In contrast to this, microwave remote sensing is sensitive to dielectric properties and structure. SAR can provide complementary information since its wave interaction occurs with different elements, characteristics and layers of the vegetation stand compared to VIS and IR waves. As a summary of hyperspectral and microwave crop monitoring, Table 2-1 reviews characteristics of vegetation influencing spectral reflectance in the VIS – NIR and backscatter in the microwave domain.

Table 2-1: Crop characteristics which influence remote sensing in the VIS – NIR and in the microwave domain (Kühbauch & Hawlitschka 2003).

VIS / IR <i>(λ, θ, ϕ)</i>	SAR <i>($\lambda, \theta, \phi, \rho$)</i>
Pigment composition	Volume (height)
Pigment concentration	Vertical and horizontal elements
Turgidity	Size, form and orientation
Cell structure	
Senescence	Distribution of fresh and dry biomass
Phenology	Phenology
Leaf areas index	Row direction
Soil pigmentation	Soil roughness
Soil moisture	Soil moisture

To move towards an operational crop monitoring approach, it is necessary to mitigate the risk associated with reliance on a single source. To meet these requirements and to improve crop parameter estimation and discrimination, methodologies that integrate optical as well as SAR data were developed (Brisco & Brown 1995). McNairn et al. 2009 performed crop inventories based on multitemporal and multisensoral satellite data with classification improvements of 3 to 18% when adding SAR data to single optical data. Also for classification purposes, Blaes et al. (2005) reported an improvement of crop discrimination of at least 5% when combining C-band SAR images (ERS, Radarsat) with optical images (Spot). Using Envisat ASAR and Landsat TM multispectral images,

Liu et al. (2006) achieved a significant improvement for yield estimation by combining both sources in the prediction model. Compared to the purely regression approach, Prévot et al. (2003) used microwave and optical data for simultaneous assimilation into crop growth models. The conclusion of this approach was that there was no significant improvement by using multi-source data compared to using only optical data.

The synergistic use of different sources was also successfully performed for the integration of hyperspectral optical data with SAR data, mainly for the enhancement of land cover classification based on an image fusion approach at the pixel level (Chen et al. 2003, Chang et al. 2004) and at the feature level (Held et al. 2003).

3 METHODS AND USED DATA

The following chapter describes the test sites, the ground truth data, the acquired satellite imagery and the data processing. In the first section, the preconditions of the study areas Huimin County and Jiansanjiang will be introduced and the sampling design as well as the ground truth data will be described in detail. In the subsequent section the acquired remote sensing data and their processing steps are described.

As a generic overview, Figure 3-1 shows the used remote sensing data and the processing steps carried out. The flow chart can be divided into the processing chains for monitoring winter wheat (Huimin test site) and the one for rice monitoring (Jiansanjiang test site). The used satellite data for Huimin test site are EO-1 Hyperion / ALI and Envisat ASAR. Additionally to satellite data, fieldspectrometer were acquired simultaneously with satellite overflight for calibration of Hyperion spectra. All remotely sensed data were pre-processed, which includes sensor specific calibration and georeferencing. For satellite optical data, standard broad-band vegetation indices were calculated and compared to narrow-band hyperspectral vegetation indices. Envisat ASAR and vegetation indices derived from Hyperion and ALI (2006) were bivariate related to ground truth measurement to establish prediction models for crop parameter estimation. Furthermore, Envisat ASAR and Hyperion (2006) were combined for multivariate regression analysis. For validation purpose, Hyperion bivariate regression model established in 2006 was applied to Hyperion acquisitions of 2007. Compared to the winter wheat monitoring, the rice monitoring is only based on X-band SAR data. The TerraSAR-X dual polarimetric data were pre-processed and the backscatter signatures plus polarimetric parameters were derived. The parameters derived from dual polarimetric X-band data were used for interpretation of physical backscatter of paddy rice fields. All data processing is aimed to improve the understanding of crop reflection behaviour in different parts of the electromagnetic spectrum and to support crop monitoring on a regional scale.

Major parts of the processing and results are published in three different papers: Koppe et al. (2010a), Koppe et al. (2012), and Koppe et al. (2013).

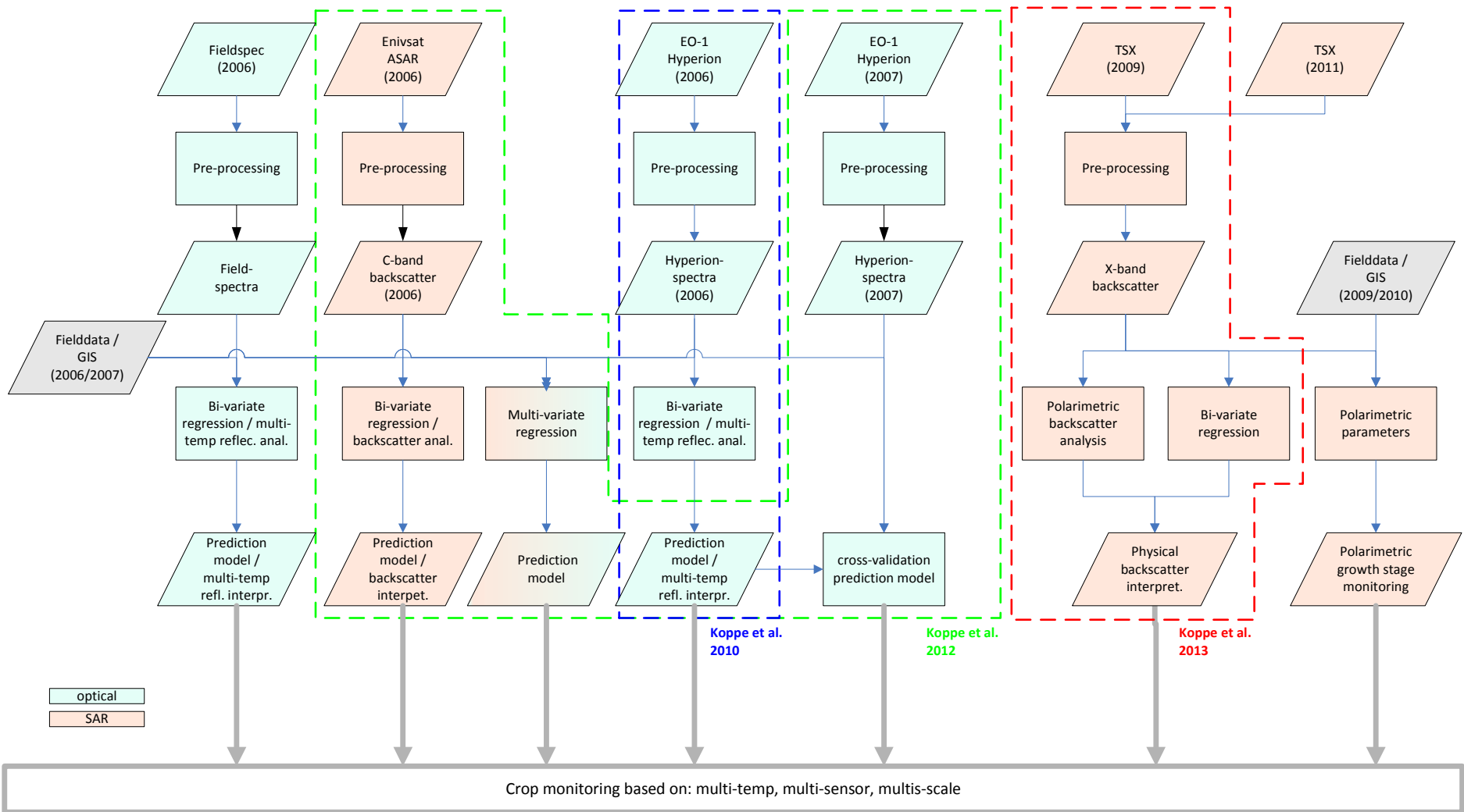


Figure 3-1: Overview of processing steps applied in the thesis.

3.1 Ground Truth

In the following section, the two test sites and the collected ground truth information will be described in detail. The Huimin test site, located in the North China Plain, is a large wheat cultivation area and well suited for monitoring of winter wheat on a regional scale. The second test site, Jiansanjiang in the Northeast of China, is widely covered by paddy rice fields and was therefore ideal for monitoring rice by spaceborne remote sensing. In both test areas, experimental stations are operated and supervised by the China Agricultural University. The Huimin test site is chosen for hyperspectral and SAR observation, in the Jiansanjiang the focus is on high resolution SAR data.

3.1.1 Huimin County Test Site*

The research was conducted in the North China Plain during the winter wheat growing season of 2005/2006 and 2006/2007. The test fields were located in Huimin County (37.3° North, 117.4° East), Shandong Province. Figure 3-2 shows the test site of Huimin County in the Shandong province. In the lower left of the figure, the study fields of different levels (L1 to L4) are overlaid over EO-1 Hyperion, acquired in 2007.

This area is characterized by a continental climate with precipitation maxima between June and September, typical for the warm-temperature sub-humid continental monsoon climate. The average temperature is 12.3 °C and annual average precipitation sums up to 580 mm, whereas more than 60% of the yearly precipitation occurs in June, July and August (Ju et al. 2006) out of the winter wheat growing season. Due to the less rain fall in the growing season, farmers have to irrigate their fields. The dominant crop rotation, up to 66% of the cultivated area, is winter wheat followed by maize enabling two harvests per year (Li et al. 2008). Huimin County was chosen because of the existence of long term field experiments managed by the Department of Plant Nutrition (CAU) and the opportunity of collecting ground truth data from selected fields.

* This section and sub-sections are an extended version of the articles: Koppe et al. (2010a); Koppe et al. (2012).

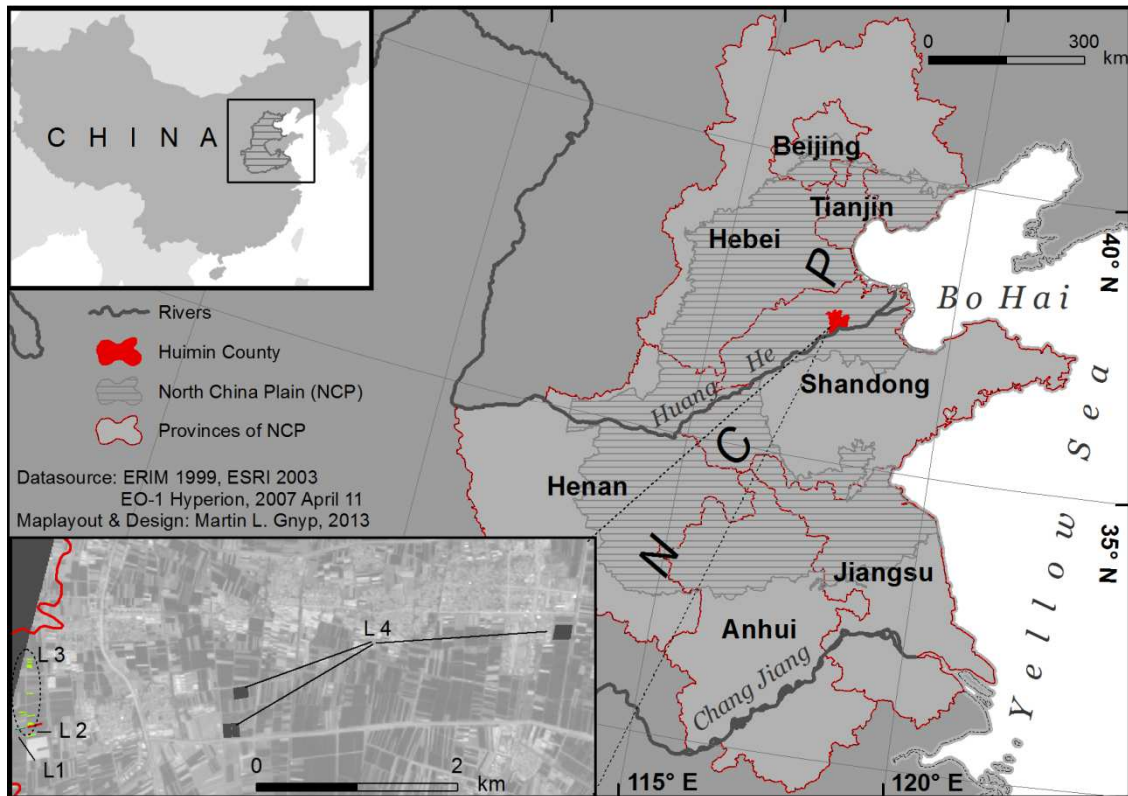


Figure 3-2: Test sites in Huimin County (Gnyp et al. 2013).

3.1.1.1 Experimental Design

The experimental design in Huimin included fields of different size, small experimental fields (level 1), large experimental fields (level 2), small farming fields (level 3) and large farming fields (level 4). The design is aimed to model biomass based on crop canopy reflectance with a multi-scale approach (Gnyp et al. 2013). For relating crop parameters with satellite based hyperspectral remote sensing on a regional scale, fields with a size between 2.5 to 4 ha were selected in the four different villages (level 4). The fields are located in the villages of Xili, Xujia, Dongjie and Shizhang in Huimin County (see Figure 3-3). All fields were managed by the farmers according to their common practices in terms of the varieties of winter wheat and the amount of N-fertilization. Each field consisted of various plots; being on average 10 m wide and 100-250 m long. A summary of the soil chemical properties and soil conditions of the farming fields in 2006 is given in Table 3-1. For the selected fields, the cultivated types of winter wheat were *Jimai20*, *Jimai21*, *Weimai8*, *Lumai23* and *Zimai12* which were sown from September to October in each growing season (2005/2006 and 2006/2007) and were harvested between early June and mid of June in the following year.

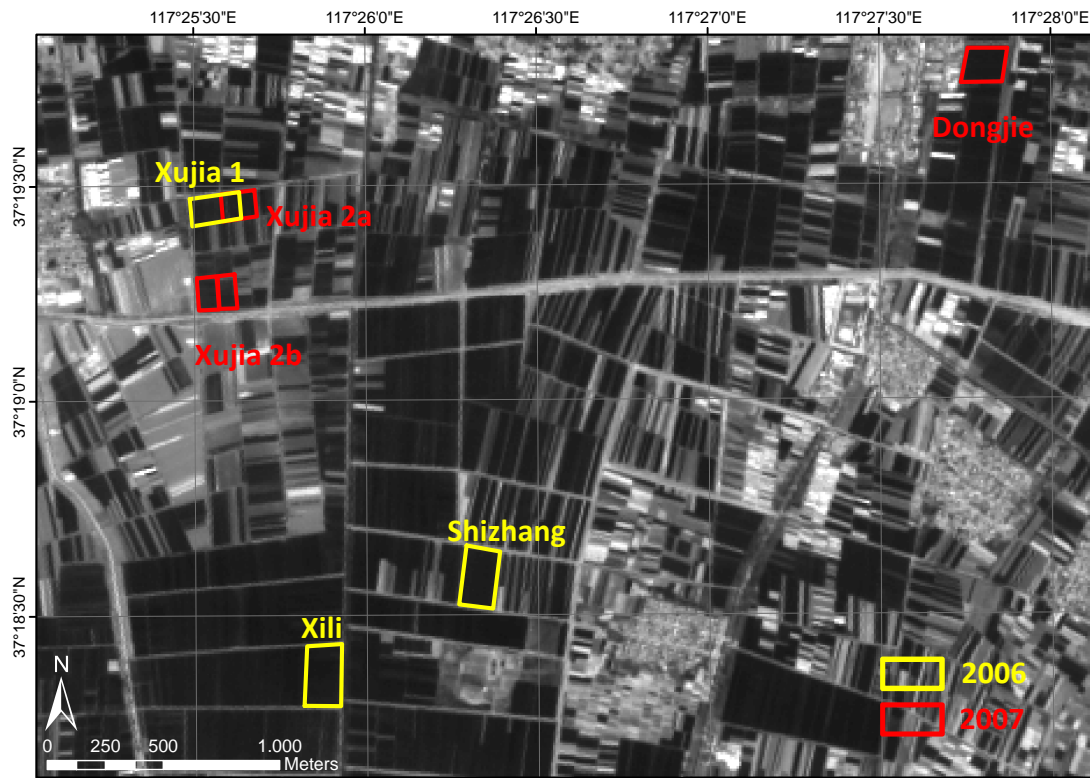


Figure 3-3: Farming fields in Huimin County.

Table 3-1: Soil chemical properties of the farming fields in 2006 (Li et al. 2008).

Village	Chemical property	Mean	Min	Max	STD
Shizhang	Total N (g/kg)	0.74	0.6	0.86	0.09
	Olsen-P (mg/kg)	27.7	14.8	48.1	13.1
	Exchangeable-K (mg/kg)	96.0	78.6	110.4	9.5
	Organic matter (g/kg)	11.8	9.5	14.4	1.7
Xili	Total N (g/kg)	0.89	0.72	1.03	0.08
	Olsen-P (mg/kg)	22.2	11.3	45.6	11.1
	Exchangeable-K (mg/kg)	123.4	86.6	166.1	23.3
	Organic matter (g/kg)	13.7	11.2	15.9	1.4
Xujia	Total N (g/kg)	1.0	0.79	1.32	0.11
	Olsen-P (mg/kg)	31.0	11.9	53.9	13.8
	Exchangeable-K (mg/kg)	146.6	86.2	222.0	29.4
	Organic matter (g/kg)	14.7	10.2	18.5	1.5
Dongjie	Total N (g/kg)	1.01	0.83	1.18	0.11
	Olsen-P (mg/kg)	45.4	32.9	56.6	8.0
	Exchangeable-K (mg/kg)	116.2	65.6	172.6	42.2
	Organic matter (g/kg)	15.1	11.5	17.9	2.1

3.1.1.2 Field Measurements

Spectral reflectance and agronomic parameter measurements were taken throughout the growing period of winter wheat from March to June in 2006 and 2007. The

measurements were carried out on a regular basis and were synchronized with the satellite overpass of EO-1 and Envisat.

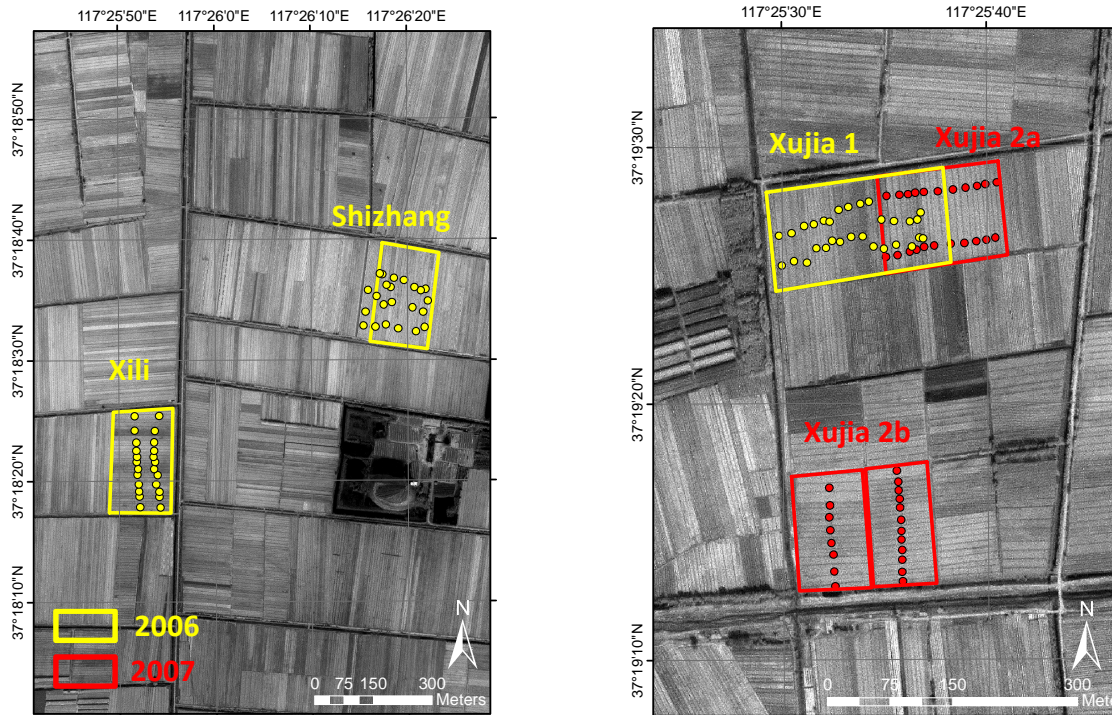


Figure 3-4: Farming fields in Huimin County with measurement points.

Five of the six measured fields are shown in Figure 3-4. In average 63 selected sample points were sampled at the fields (around 20 per field) at the different ground truth acquisition days (Table 4-1) to account for spatial variability. At these points, spectral reflectance, plant height and destructive biomass measurements were performed. To transfer point measurements to surface data, a continuous surface from the set of points was created by inverse distance weighting method. Taking the different image characteristics of EO-1 Hyperion and Envisat ASAR into account, the fields were prepared in a different way. For EO-1 Hyperion, regression analysis was performed on a pixel basis. After excluding mixed pixel on the field borders, 57 pixel in 2006 and 54 pixel in 2007 remained for further analysis. For Envisat ASAR data, the farming fields were separated into homogenous parcels to overcome speckle effect.

The canopy spectral reflectance measurements were obtained using high resolution spectrometers from Analytical Spectral Devices Inc. (ASD 1999). In 2006, a Handheld Fieldspec (range 325 nm to 1075 nm) was used and in 2007, a QualitySpec (range 350 nm to 1800 nm). The HandHeld Fieldspec device measures the visible (VIS) and near infrared (NIR) spectrum with 512 channels in the 325–1075 nm wavelength

domain. The Quality Spec measures reflectance values in 1451 channels with silicon photo diodes in the range between 350 to 1000 nm and with TE-cooled photo-diodes in the range between 1000 to 1800 nm. Reflectance values of both instruments are calculated by calibration with a barium sulphate (BaSO_4) white reference panel and a dark current measure (ASD 1999). These calibration measurements were repeated in regular intervals during the field measurement to respond to changes in solar illumination. To maintain consistent solar illumination conditions, measurements were taken between 10 am and 2 pm under mostly cloudless weather conditions. For measurement at the field scale, the ASD Handheld sensors were mounted on a tripod boom permitting a nadir acquisition 1 m above the canopy (see Figure 3-5). Based on this geometric constellation the acquisition radius r and the acquisition area A can be calculated as follows:

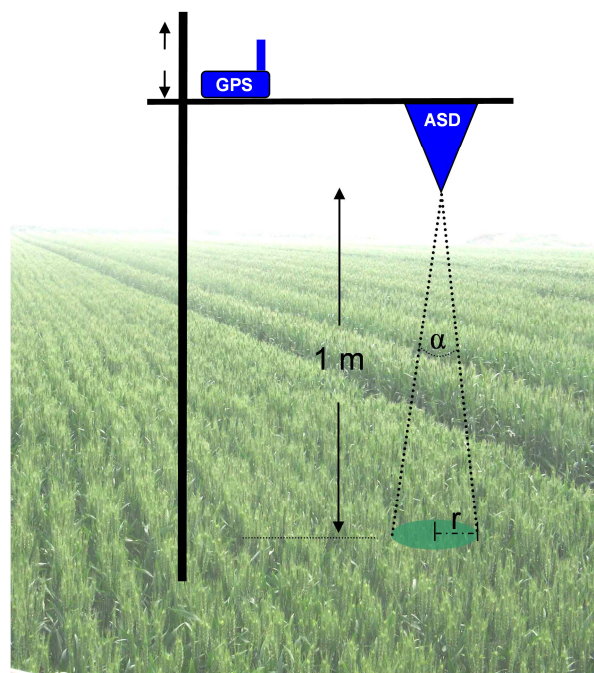
$$r = h * \tan\left(\frac{\alpha}{2}\right) \quad (3.1)$$

$$A = \pi * r^2 \quad (3.2)$$

where h is the height above the canopy and α the field of view. For a default fore optic with a field of view of 25° and height above the canopy of 1 m, the acquisition radius is around 22 cm and the acquisition area around 0.15 m^2 . Spectral measurements were repeated three times on different locations per each plot and averaged as one representative spectrum of this plot. This random sampling strategy within one plot takes account for varying conditions concerning plant density and plant orientation. During the post-processing of the acquired reflectance spectra, the values were interpolated to intervals of 1 nm by using the RS3 spectral processing software (Analytical Spectral Devices). Due to water absorption noise within the electromagnetic spectrum (leaf water absorption), the data ranges between 1346 nm to 1436 nm and 1800 nm to 1981 nm were excluded from further processing (this applies to ASD QualitySpec and EO-1 Hyperion). In the context of this research, the in-situ spectral measurements were used for calibrating satellite reflectance data.

Table 3-2: Sensor specifications of ASD Field Spec and Quality Spec (Analytical Spectral Devices 1999).

Parameter	ASD Field Spec®	ASD Quality Spec®
sensor type	passive	passive
spectral range	325 – 1075 nm	350 – 1800 nm
spectral bands	512	1450
spectral sampling interval	1.4 nm	1.4 nm (VNIR), 2.4 (SWIR)
FOV	8°, 18°, 25°	8°, 18°, 25°
detectors	Silicon (VNIR)	Silicon (VNIR) TE cooled (SWIR)

**Figure 3-5: Arrangement of canopy spectral reflectance measurements with ASD Handheld and QualitySpec (modified after Laudien 2007).**

After field canopy spectral data collection, crop samples were collected for aboveground biomass and plant nitrogen concentration determination on four dates in 2006: April 19, April 28, May 12, and May 30, with the corresponding growth stages from shooting to ripening stage. The measurements on April 19 and May 30 matched EO-1 satellite image collection very well; however, no ground measurements could match the EO-1 data acquisition on May 6. Therefore, agronomic measurements on April 28 and May 12 had to be interpolated to coincide with EO-1 acquisition on May 6.



Figure 3-6: Canopy spectral reflectance measurements at April 7, 2006 (Photo Martin Gnyp 2006).

In 2007, ground truth information was collected on three dates: April 11, April 21 and May 6. Aboveground biomass was destructively collected by cutting the vegetation on ground level within an area of 100 cm by 30 cm at the first date, 50 cm by 50 cm at second, and 30 cm by 30 cm on the last. The reduction of sample area was necessary to account for increasing biomass during the growing season. Contemporaneously with biomass collection, the plant height was measured non-destructively with a yardstick. The samples were weighed in order to obtain the plant water content (PWC) and the fresh biomass. Then the samples were dried at 70°C to constant weight to get the dry biomass. The measured biomass values were scaled to kilogram per square meter to achieve comparability with other measurements. The measured biomass values were averages over one plot and the standard deviation was calculated in order to make a statement about the homogeneity of the plot. Plant nitrogen concentration was determined for the 2006 samples by the Kjeldahl digestion method (Bremner 1960). Around 39 to 45 measurements per field were sampled.

Parameters such as seed date, harvest date, plant density, crop rotation, row direction and spacing, plant species and others were obtained from the local farmers or collected in the field during the vegetation period.

3.1.2 Jiansanjiang Test Site*

The study area is the Qixing farm, which is located in the Sanjiang Plain in North-Eastern China (47.2 N°, 132.8° E), at the downstream area of the Songhua River (Songhua Jiang). The area is approximately 60 km south of the Amur River (Heilongjiang) and 450 km west of the Pacific Ocean in the Northeast of Heilongjiang Province. The climate of this area is temperate sub-humid, with a mean annual precipitation of 500-650 mm; rainfall mainly occurs from July to September during the growing season of rice. Its topography is rather flat with an average elevation of around 60 m and is characterized by broad alluvial plains and low terraces formed by the three rivers (Heilong, Songhua, and Wusuli). The Sanjiang Plain is a major agricultural area of Heilongjiang Province. Cultivated land covers more than 50% of the area, where the most important crops are soybean, rice, and corn (Ganzezy 2005).

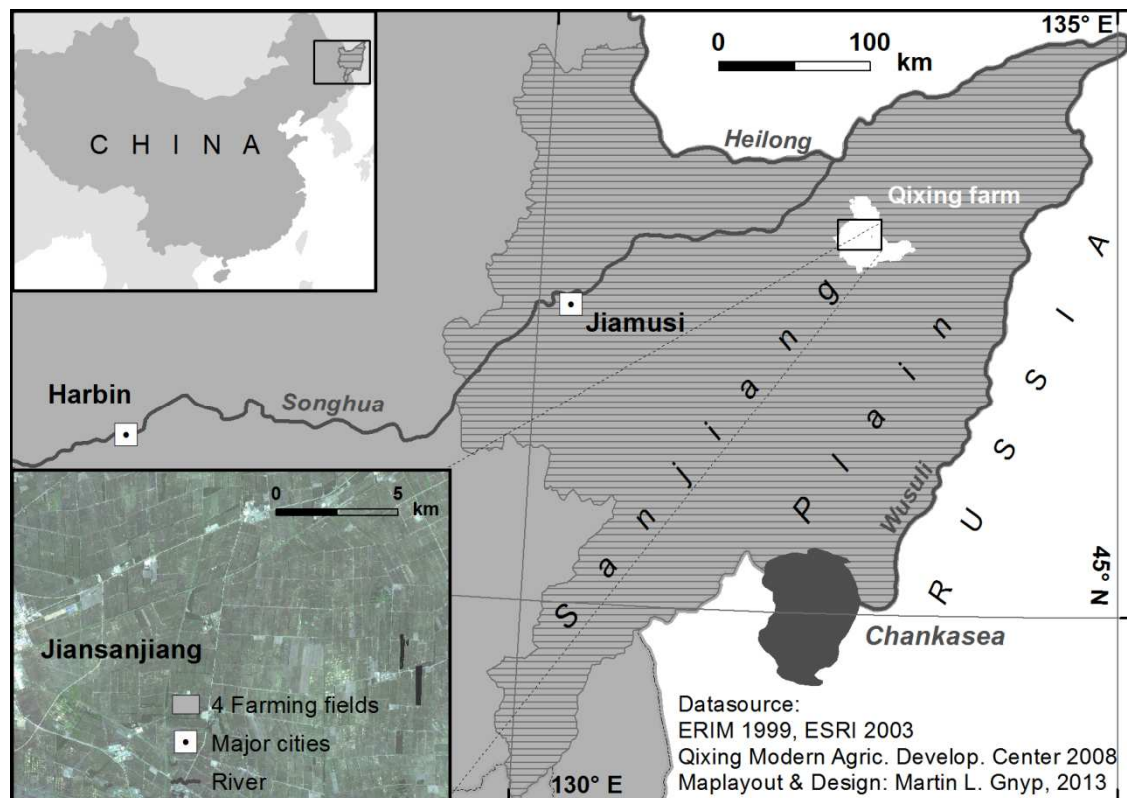


Figure 3-7: Test sites in Jiansanjiang (Gnyp et al. 2013).

The total agricultural area of Qixing farm is 51000 ha whereas 46000 ha are paddy rice. In Figure 3-7, the location of the Qixing farm and area around is shown. The dark

* This section and sub-section are an extended version of the article: Koppe et al. (2013).

patches are mainly rice cultivation; the brighter ones belong to other types of land use classes (Figure 3-7 bottom left).

3.1.2.1 Experimental Design

At Qixing farm, small rice fields (plots) of sizes between 100 to 6000 m² are grouped to larger fields. Every plot was bordered by 30-50 cm narrow and 30-50 cm high field banks which kept the water. The experimental design of the field experiments included 553 plots distributed over farmers' fields. Four of the fields (367 plots) are located within the HS footprint, whereas two fields were used for biomass measurements (see Figure 3-8). For 60 plots of the 367 plots, biomass was measured in regular intervals. For 24 other plots among the 367 plots (small experimental plots, approximately 0.02 ha), biomass was sampled in more detail.

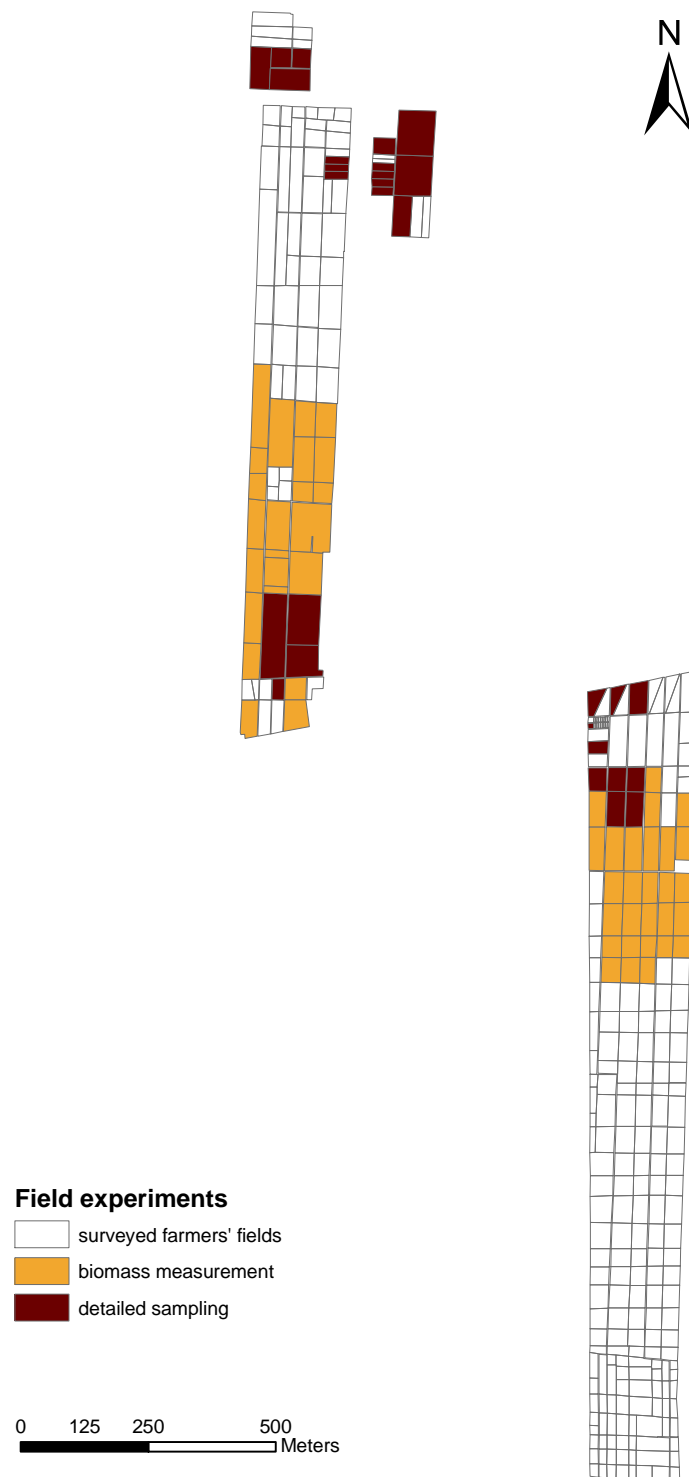


Figure 3-8: Experimental design of the Jiansanjiang test site.

The biomass samples of the 24 experimental plots were separated into stems, leaves and heads. 20 of these experimental plots are located within the High Resolution SpotLight images; four more fields are within the footprint of the SM scenes. To generate greater heterogeneity in growth rate and standing biomass, the plots were treated with three to four replications of different N rates: N0 with 0, N0.8 with 54-94, N1.2 with 81-141 kg/ha, and chemical control with 67-118 kg/ha. The dynamic N rates

were dependent on the different farmers and the management strategy of China Agricultural University. This experimental design induces a higher inter-field variability (see dynamic range of total biomass in Table 4-2). For this contribution, the field campaign of 2009 lasted for about five months, starting at the tillering stage, and ending with the harvest of the rice crop about DAT 135 (day after transplanting). As normal for rice cultivation in the Sanjiang Plain, the paddy fields were flooded before transplantation of the seedlings mid to end of May. Sets of three to five seedlings were planted to one hill, with a hill spacing of about 12 cm and a row distance about 35 cm, resulting in a planting density of 120 to 150 seedlings per m².



Figure 3-9: Small plots within larger rice fields (Photo Martin Gnyp 2009).

During the vegetation period, the rice total biomass increased steadily at vegetative and reproductive stages and reached the maximum value of about 15 t/ha before harvest. The heading date, when 50% of the heads were totally emerged, was around DAT 70.

3.1.2.2 Field Measurements

Agronomic and biophysical data of the crop such as plant height, tiller density and biomass were measured at regular intervals during the field campaign by destructive

and non-destructive sampling methods. Plant height was measured with a yardstick close to rice plants from water surface (later in the growing season from the soil surface) to the top of the canopy. More parameters such as leaf age and tiller number were also measured non-destructively. To achieve a representative height for every plot, several measurements were taken and averaged for every plot. For this, at each plot 20 hills in a row were selected and marked to be sure to measure the same plants. Aboveground biomass was collected by clipping three to five hills of representative vegetation at tillering, panicle elongation, booting, before heading and at heading stage. Five hills were used at early stages (tillering to panicle elongation) and three hills at later stages (from booting to heading) due to high biomass amount. The cut plants were separated into stems, leaves and heads, oven dried at 105°C for half an hour to stop the biophysical processes, then oven dried at 70° to constant mass and weighed.

As for the Huimin test site, the measured biomass values were scaled to kilogram per square meter to achieve comparability with other measurements. The measured biomass values were averages over one plot and the standard deviation was calculated in order to analyse the homogeneity of the plot.

Leaf area index (LAI) is an important canopy parameter which is defined by “one half the total green leaf area per unit ground surface area” (Watson 1947). It is expressed in area of leaf (m²) per area of ground surface (m²). LAI was estimated from destructively sampled leaves. For this, 3 cm were cut from 20 randomly selected leaves for each plot.

Parameters such as seed date, harvest date, plant density, row direction and spacing, plant species and others were obtained from the local farmers or collected once in the field during the vegetation period.

3.2 Satellite Data Acquisitions, Processing and Analysis

Remote sensing at different frequencies is a powerful method for gathering information about the vegetation. Satellite data were acquired for the test sites Huimin County in the years 2006 and 2007 and for the Jiansanjiang test area in 2009 and 2011. For Huimin County multispectral (EO-1 ALI) and hyperspectral (EO-1 Hyperion) satellite imagery as well as SAR data (Envisat ASAR) were gathered. For the

Jiansanjiang test site dual polarimetric TerraSAR-X in High Resolution SpotLight, SpotLight and, StripMap mode were acquired. In Table 3-3 acquired satellite data and specification are listed for the two areas.

Table 3-3: Acquired satellite data for the test sites Huimin and Jiansanjiang (modified after Koppe et al. 2012 and Koppe et al. 2013).

Test site	Satellite	Year	Mode	Date	DAT	Growth stage	Path direction	Pol.	Local inc. angle (°)
Huimin	Envisat ASAR	2006	IS5	March 25		tillering	ASC		39
			IS6	April 13		jointing	ASC		42
			IS6	April 29		booting	ASC	VV	39
			IS6	May 10		heading	DSC		40
			IS6	June 3		ripening	ASC		39
	EO-1 Hyperion	2006		April 19		jointing			
				May 6		heading			
				May 31		ripening			
		2007		April 11		jointing			
				April 21		booting			
Jiansanjiang	TerraSAR-X	2009	HS	June 24	35	tillering			
				July 5	46	stem elong.			
				July 16	57	booting	ASC	HH/VV	39
				July 27	68	heading			
				Aug 7	79	flowering			
				Aug 29	101	ripening			
			SM	June 26	37	tillering			
				July 7	48	stem elong.			
				July 18	59	booting	DESC	VV	36
				July 29	70	heading			
				Aug 9	81	flowering			
		2011	SL	June 15	29	tillering			
				June 26	40	stem elong.			
				July 7	51	booting	ASC	HH/VV	26
				July 18	62	heading			
				Aug 9	84	flowering			
				Aug 31	106	ripening			
				June 17	31	tillering			
				June 28	42	stem elong.	DESC	HH/VV	46
				July 9	53	booting			
				July 20	64	heading			

3.2.1 EO-1 Hyperion and ALI*

During the 2006 field campaign, three Hyperion and ALI images were acquired: on April 19, May 6 and May 31. In the subsequent vegetation period 2007, again three acquisitions of Hyperion and ALI were taken on April 11, April 21, and May 6. The optical sensors Hyperion and ALI are mounted on the Earth Observing One (EO-1) Satellite that follows the World Reference System-2 (WRS-2) with a 16 day repeat cycle for nadir mode. Both sensors are push broom imaging spectrometers that are capable of cross-track pointing (Earth Observation-1, 2003). The multispectral Advanced Land Imager (ALI) acquires information in nine discrete bands with a spatial resolution of 30 m. An additional panchromatic channel has a resolution of 10 m. The Hyperion hyperspectral sensor collects continuous data with a VNIR and a SWIR spectrometer in the 400-2400 nm wavelength domain. Each frame taken captures images in a 7.7 km wide and 42 km (resp. 185 km) long area. Similar to the multispectral ALI, Hyperion provides also a spatial resolution of 30 m. EO-1 Hyperion images are radiometric calibrated (Level 1R) and delivered in 16-bit radiance data (Pearlman et al. 2003).

Table 3-4: Technical specification of EO-1 Hyperion and ALI.

	Hyperion	ALI
Start	November 21, 2000	
Orbit	Sun-synchronous, 705 km	
Inclination	98.2°	
Spectral range	242 spectral bands (400-2500 nm)	1 Pan, 9 Multi-spectral bands (400-2500 nm)
Spectral resolution	10 nm	variable
Spectral coverage	continuous	discrete
Spatial resolution	30 m	Pan: 10 m, Multi-spectral: 30 m
Repetition rate	16 days	
footprint	7.6 x 100 km	36 x 185 km

* This section and sub-sections are an extended version of the articles: Koppe et al. (2010a); Koppe et al. (2012).

The processing of EO-1 Hyperion consists of a pre-processing chain to prepare the raw hyperspectral data and a subsequent calculation of vegetation indices. Figure 3-10 depicts the main processing steps of the EO-1 Hyperion processing chain. The components are explained in detail hereinafter.

3.2.1.1 EO-1 Hyperion and ALI Processing

Satellite image pre-processing of Hyperion and ALI data included (a) a correction for sensor artifacts, (b) an atmospheric correction as well as (c) a geometric correction. The performed pre-processing steps (Lillesand et al. 2008, Khurshid et al. 2006) were aimed to improve the quality of the images for multi-temporal data analysis.

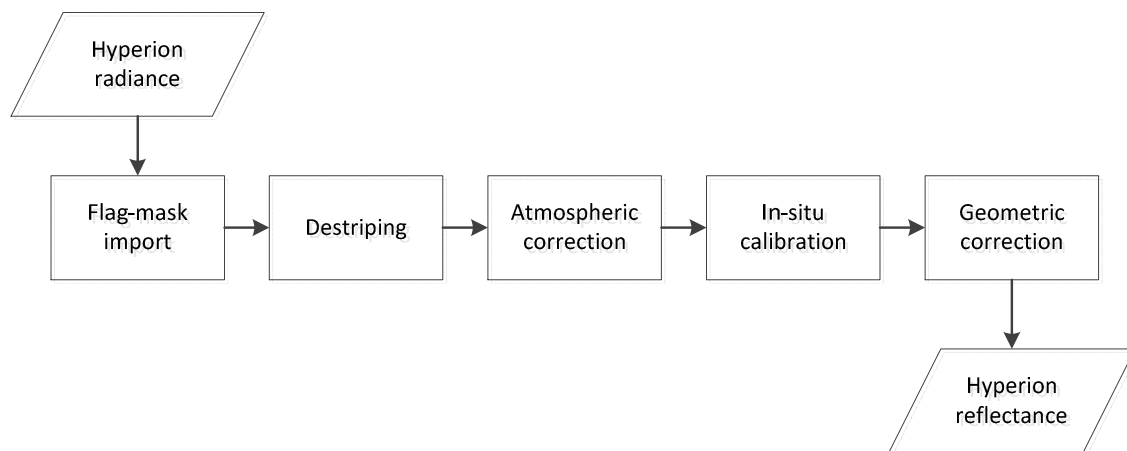


Figure 3-10: Pre-processing steps of EO-1 Hyperion data.

For correction of sensor artifacts, uncalibrated and corrupted Hyperion bands were eliminated by applying the Flag-Mask that was delivered with the data product. A Flag-Mask indicates detectors which are unresponsive and unreliable (USGS 2007). 158 of the original 242 bands had remained for subsequent destriping (described in Datt et al. 2003). During the destriping process, periodic along track stripes in image data caused by detector errors, were removed. Since some of the bands were not repairable, another 17 bands had to be excluded. The destriping and exclusion of image channels was performed with ENVI software (ITT 2011). For some application using single satellite observations, it is of no importance to atmospherically correct image data (Schowengerdt 2007). However, in the present work, the focus was set on multi-temporal analysis as well as on matching image data to canopy spectral reflectance that was measured using a portable spectroradiometer (Fieldspec® Pro by ASD). The measured at-sensor radiance L of Hyperion and ALI data consists of reflectance from

the surface and scattering from the atmosphere. Major sources of distortions of remotely sensed imagery are water vapor and aerosols (Cairns 2003).

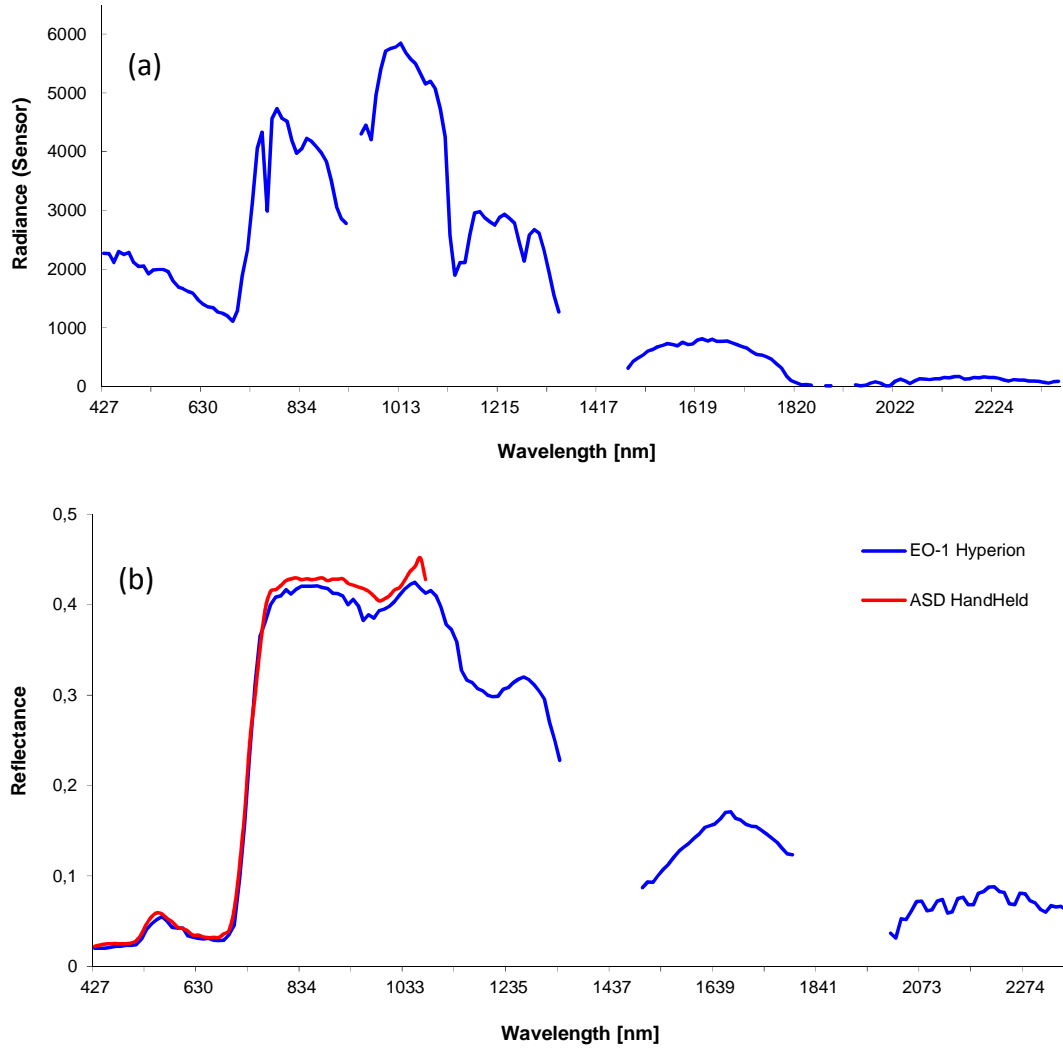


Figure 3-11: Comparison of single pixel spectra before (a) and after (b) atmospheric correction. Spectra were acquired on April 19, 2006 (modified after Koppe et al. 2010a).

To convert the Hyperion and ALI at-sensor radiance data to surface reflectance data, the MODTRAN-based radiative transfer algorithm implemented in the FLAASH module of ENVI software was used. The radiative transfer algorithm that applies for Lambertian materials, converts the at-sensor radiance L to surface reflectance ρ on a pixel-by-pixel basis as (Berk et al. 2000):

$$\rho = \frac{L - L_a}{(L - L_a)S + T_2 \frac{E_s * \cos(\theta_s)}{\pi}} \quad (3.3)$$

where L_a is the radiance caused by atmospheric scattering; T_2 is the two-way transmittance; S is the albedo of the atmosphere; θ_s is the solar zenith angle and E_s is

the exoatmospheric solar irradiance. The radiative transfer algorithm is described in Berk et al. (2000). Atmospheric scattering effects were compensated and a surface reflectance spectrum for each pixel was retrieved. The comparison of single pixel at sensor radiance and surface reflectance from fully developed winter wheat is shown in Figure 3-11. As standard atmosphere used in the radiative transfer algorithm does not exactly reflect conditions at the time of acquisition, it was necessary to calibrate initial reflectance with in-situ spectrometer measurements. In Figure 3-11 a comparison of EO-1 Hyperion calibrated reflectance spectrum and ASD field measurements is shown. Additionally, the 158 spectral bands of Hyperion are overlaid.

The last step of the Hyperion and ALI pre-processing chain is the geometric correction, which was undertaken to rectify geometric distortions using ground control points (GCPs), sensor parameters and a digital elevation model. For orthorectification process of each scene, 25 GCPs distributed across the area of interest were selected and the image rectification was carried out by bilinear resampling method using ENVI. For evaluation purpose, other 20 independent check points were used, which resulted in overall RMSE of around 0.5 pixels (15 m) for each image.

3.2.1.2 Analysis of Hyperspectral EO-1 Hyperion Data

Hyperspectral imaging allows data acquisition of a target with a large number of information layers, which implies the collection of a high amount of useful but also redundant data. The analysis of hyperspectral data is primarily the reduction of information depth and extraction of required information. For the analysis of hyperspectral data different approaches can be applied. The reflectance spectra of contiguous wavebands allows for distinguishing targets, phenological stages of vegetation or anomalies through the calculation of spectra differences, vegetation indices or derivations (Kumar et al. 2003).

Spectral vegetation indices can be used to identify plant development at different phenological stages during the growing season. For calculation of vegetation indices and subsequent regression analysis with ground truth data, the spectral profile for each pixel of the test fields of 2006 and 2007 was extracted. After excluding mixed pixel on the borders, 57 pixel in 2006 and 54 pixel in 2007 (ca. 14 per field) remained for further analysis.

Table 3-5: Standard vegetation indices evaluated in this study (Koppe et al. 2010a).

Index	Name	Formula	References
SR	Simple Ratio	ρ_{NIR} / ρ_R	(Baret & Guyot 1991)
NDVI	Normalized Difference Vegetation Index	$(\rho_{NIR} - \rho_R) / (\rho_{NIR} + \rho_R)$	(Rouse et al. 1974)
OSAVI	Optimized Soil-adjusted Vegetation Index	$(1 + L)(\rho_{NIR} - \rho_R) / (\rho_{NIR} + \rho_R + L)$	(Huete 1988)
TVI	Triangular Vegetation Index	$0.5 * (120 * (\rho_{NIR} - \rho_{Green}) - 200(\rho_R - \rho_{Green}))$	(Broge & Leblanc 2000)

Pixel based reflectance spectra were then used for the calculation of (1) standard broad band vegetation indices, (2) standard hyperspectral vegetation indices, and (3) narrow band Normalized Ratio Indices (Schmidt & Skidmore 2003, Sims & Gamon 2002). Within this study, broad band vegetation indices are based on multi-spectral bands, whereas the bands cover wide spectral range. In the case of the EO-1 ALI Sensor, the spectral span of one band is around 80 nm. In comparison, the narrow bands of EO-1 Hyperion cover a spectral range of around 10 nm. To compare the prediction power of broad band and narrow band crop parameter estimations, the following vegetation indices were calculated: Simple Ratio (SR), Normalized Difference Vegetation Index (NDVI), Optimized Soil Adjusted Vegetation Index (OSAVI) and Triangular Vegetation Index (TVI). The SR, NDVI and OSAVI vegetation indices are based on the difference between strong absorption of solar radiation in the red, caused by chlorophyll pigments and the high leaf cellular reflection in the near infrared. Unlike the Simple Ratio Index, the NDVI is normalized which reduces the effects of variable illuminations and limits the NDVI to values from -1 to 1 (Baret & Guyot 1991). The OSAVI is intended to minimize influences due to soil optical properties. The included background factor L depends on vegetation density and requires information about the relationship between soil background and vegetation (Huete 1988). The TVI was developed by Broge & Leblanc (2000) and is defined additional to red and near infrared reflectance by the magnitude in the green region. The detailed expressions and the notable references of the mentioned vegetation indices are provided in Table 3-5. A full list of vegetation indices under consideration is provided in Annex A.1.

In addition to standard vegetation indices, a specific waveband selection method suggested by Thenkabail et al. (2000) and Sims & Gamon (2002) was used to determine best band combinations suitable for crop parameter estimation (see also Schmidt & Skidmore 2003). The two-band Normalized Ratio Index (NRI) is defined as (Sims & Gamon 2002):

$$NRI_{(band\ 1, band\ 2)} = \frac{(\rho_{band\ 1} - \rho_{band\ 2})}{(\rho_{band\ 1} + \rho_{band\ 2})} \quad band\ 1 \geq band\ 2 \quad (3.4)$$

where $\rho_{band\ 1}$ and $\rho_{band\ 2}$ are reflectance of Hyperion narrow bands in the wavelength range between 400 and 2500 nm. The hyperspectral Hyperion Sensor allows the calculation of a total number of 9870 ($141 \times 140 / 2$) possible two-band combinations for each agronomic parameter. A linear regression between each vegetation index and crop parameter was performed.

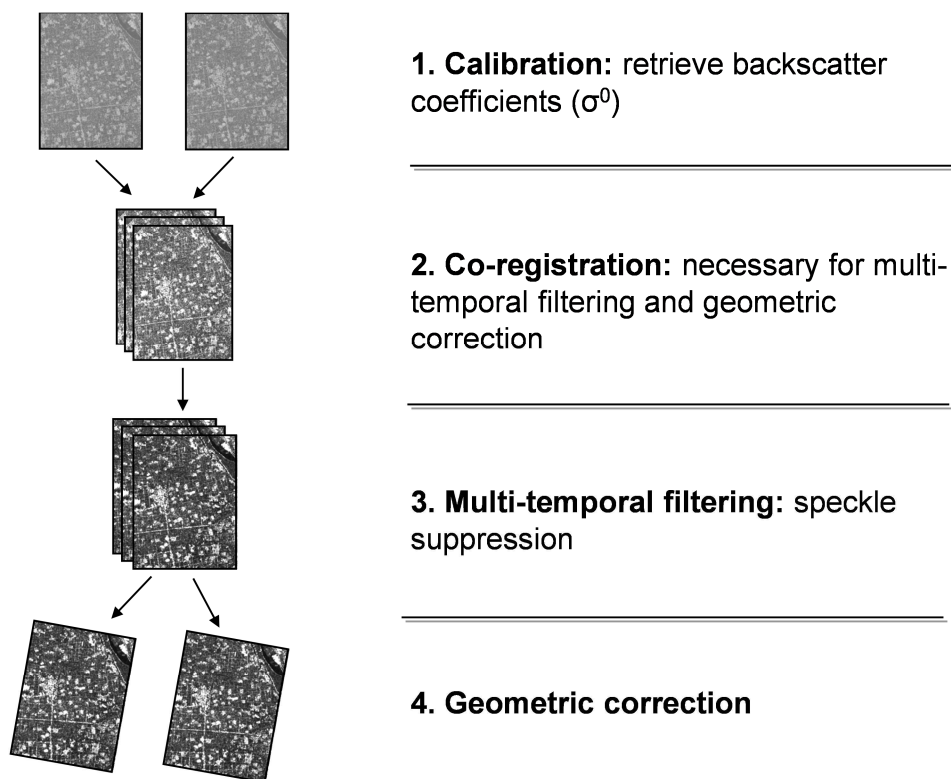
3.2.2 Envisat ASAR Processing*

During the first field campaign in 2006, Envisat ASAR (Advanced Synthetic Aperture Radar) data were acquired for the test area. Envisat ASAR operating at C-band has an active phased array antenna which is equipped with transmit and receive modules allowing data acquisition in StripMap and ScanSAR mode. For this study, Envisat ASAR IMP VV intensity precision images with a pixel spacing of 12.5 m and a nominal spatial resolution of 30 m were selected. The imaging modes of the ASAR data were acquired in IS5 and IS6 mode with an incidence angle range between 39° to 42°. To get a larger area covered and to shorten time between acquisitions, different relative orbits were chosen. The four test fields for the recent study are located in the overlapping area of all acquisitions. The processing of Envisat ASAR consists of a pre-processing chain to prepare the raw SAR data and a subsequent extraction of backscatter values. Figure 3-12 depicts the main processing steps of the Envisat ASAR processing chain. The components are explained in detail hereinafter.

* This section is an extended version of the article: Koppe et al. (2012).

Table 3-6: Technical specification of Envisat ASAR.

Envisat ASAR	
Start, site	March 1, 2002, Kourou
Launch mass	8200 kg
Orbit altitude	790 km
Inclination	98.5°, Polar orbit
Frequency	5.3 GHz
Height	26 m
Diameter	10 x 5 m
Polarization	Single pol, dual pol
Resolution	30 m x 30 m, 150 m x 150 m, 1000 m x 1000 m (depending on mode)
Repetition rate	25 days
Life time	5 years (plus extension)
Modi	Image, altern. polarisation, Wave, Wide Swath, Global Monitoring

**Figure 3-12: Processing chain of Envisat ASAR.**

Prior to data analysis, Envisat ASAR images were pre-processed in a four step approach. At first, the image DN were converted to averaged backscattering intensity (dB, squared amplitude) expressed in sigma nought. The normalization of the ASAR images facilitated the multi-temporal backscatter analysis of the winter wheat. Based on the header file information and an ellipsoid model, the ASAR images can be converted to sigma nought as follows (Rosich & Meadows 2004):

$$\sigma_{ij}^0 [dB] = 10 * \text{Log}_{10} \left(\frac{DN_{ij}^2}{K} \sin(\theta_{ij}) \right) \quad (3.5)$$

where DN is the pixel intensity of the i, j pixel, K the absolute calibration constant and θ the incidence angle of the i, j pixel. Finally, sigma nought values were transformed to logarithmic scale. Since the test area in Huimin is rather flat, an elevation model to account for topographic distortions is not necessary.

After normalization, the images acquired with the same geometry (same orbit and incidence angle) were co-registered to each other. For this, the first acquisition was defined as the master and subsequent images were treated as slaves and were co-registered to the master image. For the co-registration, the orbit parameters were used as an initial rough localisation, followed by cross-correlation in order to register the images in a coarse way. A fine registration was performed as a final step by maximizing the coherence between master and slave images.

Next, speckle noise caused by interference of different elementary scatterers was filtered by a 5x5 Gamma adaptive filter which showed acceptable results for the trade-off between edge preservation and speckle reduction. The reduction of the noise level was evaluated by visual inspection and statistical measurement of effective number of looks (ENL) as suggested by Oliver & Quegan (2004):

$$ENL = \frac{\mu^2}{\sigma^2} \quad (3.6)$$

where μ is mean value (noise mean value) and σ the standard deviation of the measured area (noise variance). ENL is obtained by calculating the mean and variance

intensity over a homogenous area. The higher the value of the quotient, the lower the speckle noise in the area. The Gamma Map filter with a 5x5 kernel yielded an ENL of 29 compared to around 15 of the noisy images. Co-registration of the slave images to one master image of the same relative orbit with the same imaging geometry was performed with the ESA toolbox NEST. The co-registration process is based on orbit parameters for an initial registration and a subsequent cross correlation of master and slave images.

In a last step of pre-processing, the co-registered and calibrated image stack was geo-referenced using well distributed GCPs. The residual error was 0.6 pixel in range and 0.9 pixel in azimuth direction. The test parcels, for which ground truth measurement was performed, were buffered by a one-pixel zone in order to exclude pixels near the boundaries since they could contain information from neighbouring fields.

3.2.3 TerraSAR-X Processing

Time series of TerraSAR-X data were acquired during the year 2009. The satellite was launched in June 2007 and operates in a sun-synchronous near polar orbit in 514 km height above earth surface. In June 2010, an identical satellite (TanDEM-X) was launched, operating within the TerraSAR-X mission as single satellite and in constellation with the first satellite within the TanDEM-X mission for interferometric 3D generation. TerraSAR-X and Tandem-X satellites operate at a frequency of 9.6 GHz (X-band) and provide high resolution SAR images in SpotLight, StripMap and ScanSAR modes with varying spatial resolution between 0.25 (slant range) and 35 m. Six High Resolution SpotLight (HS) images were acquired with an incidence angle of about 39° in ascending orbit direction. In addition to the HS data, StripMap (SM) data with an incidence angle of about 36° in descending orbit direction were acquired to cover the complete test area. The HS images have a ground range resolution of around 1.2 m for the incidence angle of 39° whereas the SM images have a coarser resolution of 3.5 m. The HS and SM data were acquired in repeat pass with 11 day intervals in order to obtain a multi-temporal data stack with constant acquisition parameters.

Table 3-7: Technical specification of TerraSAR-X and TanDEM-X.

	TerraSAR-X	TanDEM-X
Start, site	June 15, 2007, Baikonur	June 21, 2010, Baikonur
Launch mass	1230 kg	1350 kg
Orbit altitude	514 km	
Inclination	97.4° (sun synchronous)	
Frequency	9.65 GHz	
Length	4.88 m	
Diameter	2.4 m	
Polarization	Single pol, dual pol, (quad pol, scientific)	
Resolution	0.8, m1.1 m, 3.3 m, 18 m, 35 m (depending on mode)	
Repetition rate	11 days	
Life time	5 years (3 years parallel operation of both satellites)	
Modi	Staring SpotLight, High Resolution SpotLight, SpotLight, StripMap, ScanSAR, Wide ScanSAR	

The processing of TerraSAR-X consists of a pre-processing chain to prepare the raw SAR data, a subsequent extraction of backscatter values and a calculation of polarimetric parameters. The derived parameters can be generalized into groups which analyse the power, the correlation and the compact polarimetric decomposition. The class power contains the backscatter extraction and the calculation of the co-polarimetric ratio. Both parameters are based on the amplitude data. The second group contains correlation of the magnitude and correlation of the phase (PPD – Polarimetric Phase Difference) of the coherent co-pol channels. The correlation parameters are calculated on the complex data. The last class contains the compact polarimetric decomposition, based on the partial coherency matrix (T). Figure 3-13 depicts the main processing steps of the three classes of the TerraSAR-X processing chain. The components are explained in detail hereinafter.

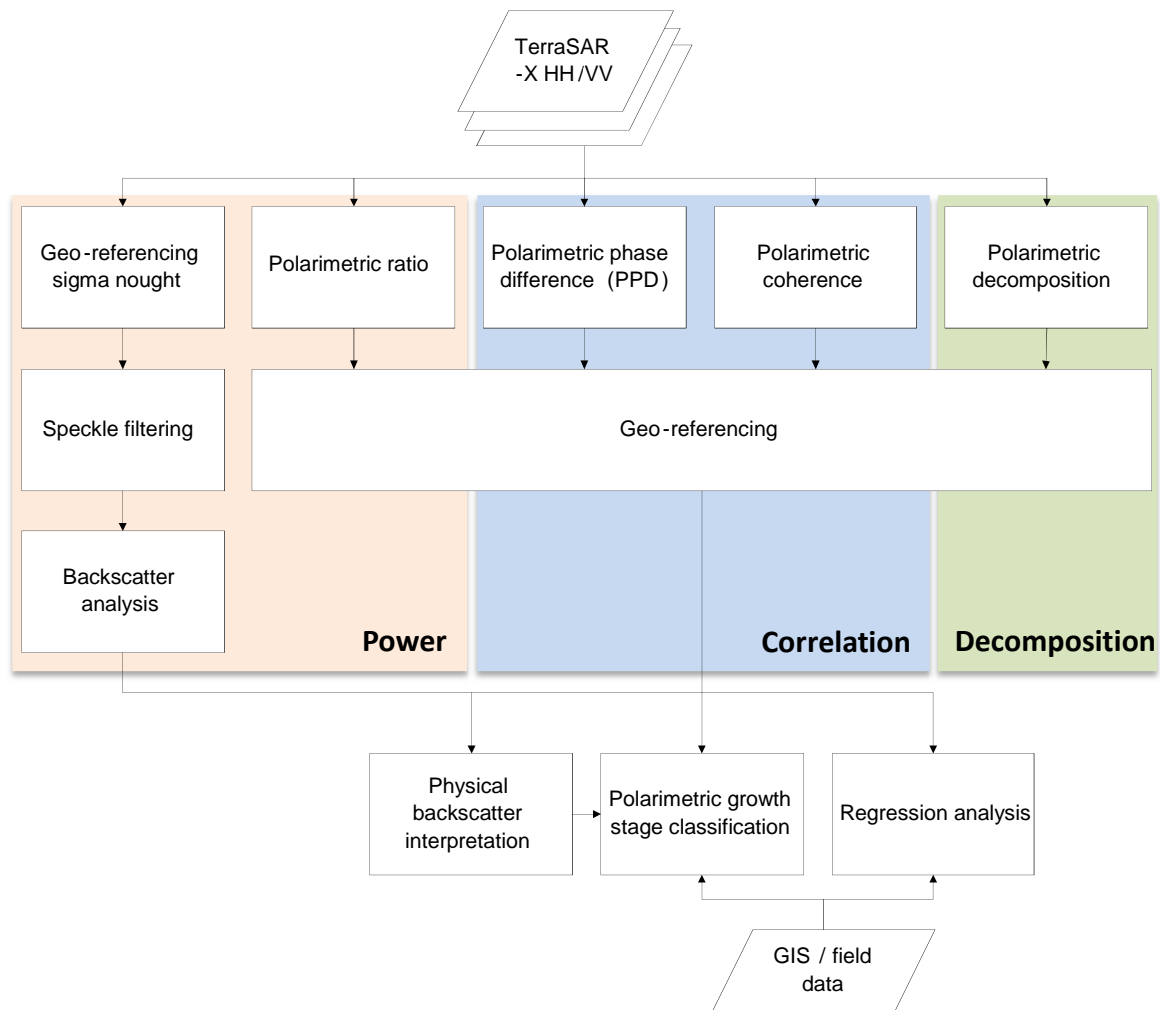


Figure 3-13: Processing chain of TerraSAR-X.

3.2.3.1 Speckle Suppression

Especially the high resolution TerraSAR-X data are affected by speckle, which affect the qualitative image information extraction. To overcome the unwanted noise, different standard and experimental speckle filters were tested for the TerraSAR-X HS data. The main idea of a speckle filter is to reduce the noise while maintaining the edges and line features. Standard adaptive filters such as Lee, Gamma-MAP and Frost are based on the assumption that the mean and variance of the pixel of interest are equal to the local mean and variance of all pixels within the user-selected moving window. They are well described in textbooks (Massonnet & Souyris 2008, Henderson & Lewis 1998).

Furthermore, three different experimental filters were implemented: Anisotropic Diffusion (Perona & Malik 1990), Modified Normal Distribution, and Level Bell for evaluation purpose. The first filter is implemented in the Orfeo-toolbox (OTB

Software); the latter two were advanced and adapted in cooperation with the Terrapid3D project (Koppe & Kiefl 2010).

Anisotropic Diffusion (also called non-uniform or variable conductance diffusion) provides a high level of regularization in homogenous areas and preserves edges. The filtering is based on a nonlinear diffusion process (Perona & Malik 1990):

$$\frac{\partial g(x, y, t)}{\partial t} = \nabla \cdot \nabla g(x, y, t) \quad (3.7)$$

where $g(x, y, t) = f(x, y)$ is the input image, $g(x, y, t) = G(\sqrt{2t}) \otimes f(x, y)$, $G(s)$ is a Gaussian with standard deviation σ .

The **Modified Normal Distribution** filter is a simple, light-weight smoothing filter that uses a moving window to get average values weighted according to the normal distribution. Weighting is applied according to the differences in intensities; higher contrast features are less smoothed (Koppe & Kiefl 2010).

Intensity at p_0 :

$$p_o = \sum i_p \cdot N(0, \sigma^2) \left(\frac{p - p_0}{r} \right) \cdot \log_2(\|i_p - i_{p_0}\|) \quad (3.8)$$

where σ^2 is the standard deviation, for p moving window of radius r .

The aim of the **Level Bell** filter is to try to remove noise by estimating the intensity of each pixel without noise, thus improving the contrast between higher and lower intensity areas of an image. If the pixel is in an area containing many dark pixels, the following algorithm is used (darkening factor at p_o):

$$p_o = \sum_{p_1, p_2} \frac{((p_1 - p_0) \cdot (p_0 - p_2))^4}{(\|p_1 - p_0\| \|p_2 - p_0\|)^6} \quad (3.9)$$

for blocks at p_1, p_2 in moving window

The window of neighbouring pixels is scanned for 3x3 blocks containing more than a threshold number of dark pixels. The vectors between the central pixel and each pair of blocks are then compared using a scalar product, to determine if a pixel is between dark areas (Koppe & Kiefl 2010):

- If the pixel is in an area containing many bright pixels, the same algorithm is used but looking for bright pixels. In the case that the area contains many of both dark and light pixels, only the higher factor is used.
- If the pixel is in an area that doesn't contain many dark or bright pixels, the intensity is averaged with the closest out of the local and global mean intensities.

The unfiltered SpotLight image has a lot of noise, which is clearly visible in the image (Figure 3-14 left). The homogenous area is very noisy, represented by low and high backscatter values. All filters resulted in an overall smoothing of the image. The smoothing intensity depends either on the kernel size (standard filters) or on the iteration (Anisotropic). Smoothing is very strong in the level bell result, but losing a lot of detail and structure. To describe the smoothness of the images in a quantitative manner, the ENL for the selected homogenous areas was calculated (see Table 3-8). The original image has an ENL of 16; all filtered images have an ENL above 16. The values mirror the visual analysis. Level bell and Anisotropic with 20 iterations are very smooth, but very blurry. The best compromise is the Frost 5x5 filter with focus on edge preservation and the anisotropic 8 iterations, which shows a satisfactory smoothing with a slightly better edge preservation than the frost filter.

Table 3-8: Quantitative measurement of noise for standard adaptive and experimental filters.

Filter typ	ENL
unfiltered	16
Lee 5x5	29
Frost 5x5	27
Gamma Map	25
Level bell	146
Modified Normal Distribution	87
Anisotropic, 20 iterations	105
Anisotropic, 12 iterations	74
Anisotropic, 8 iterations	52

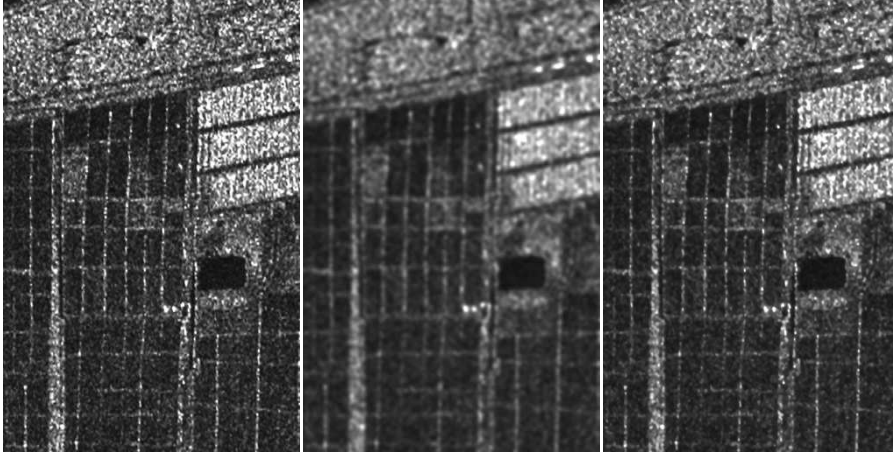


Figure 3-14: SAR filter results (based on HS, August 8, 2009). Left: Unfiltered. Middle: Level Bell. Right: Anisotropic, 8 iterations.

3.2.3.2 Power*

Level 1b complex data were converted to intensity (squared amplitude) since multi-temporal backscatter analysis and regression analysis with crop parameters were based on intensity values. In order to extract plot-level specific crop information, the images were registered to each other and to the additional existing vector data. Because SAR side-looking geometry causes geometric distortions when projecting slant range geometry on earth, a Digital Elevation Model (DEM) together with satellite orbit information were used for ortho-rectification of the images. The applied DEM was created with radargrammetric techniques based on stereo TerraSAR-X images. Due to high inherent slant range location accuracy of up to 0.5 m (Eineder et al. 2011), no ground control points are needed for orthorectification. After orthorectification, 18 ground control points were used for assessing the geo-location accuracy. The resulting errors were 1.5 pixels in azimuth and 1.8 pixels in range direction, which is in accordance with investigations by Koppe et al. (2010b) for medium accurate DEM in flat to rolling terrain. With orthorectification, a radiometric calibration to sigma nought was also carried out using the following equation (Fritz & Eineder 2010):

$$\sigma_{ij}^0 [\text{dB}] = 10 * \log_{10} (K * \text{DN}_{ij}^2 * \sin(\theta_{ij})) \quad (3.10)$$

* This section is an extended version of the article: Koppe et al. (2013).

where DN is the pixel amplitude of the i, j pixel, K the calibration factor, and θ the local incidence angle of the i, j pixel. The equation was used to transform the amplitude of the backscattered signal (DN) into the backscattering coefficient (σ_{0ij}) in decibel. The calibration factor for TerraSAR-X images varies between 10^{-6} and 10^{-4} depending on the incidence angle and polarization. The radiometric calibration is a requirement for multi-temporal analysis of different images.

In order to investigate the temporal backscatter behaviour of crop as well as for empirical modelling of biophysical parameters, sample plots of each test site were selected on the multi-temporal SAR data defining polygons around the plots. To avoid mixed pixel a buffer of two pixels to the plot border was maintained. The pixel values of each polygon were averaged and the multi-temporal SAR signature was extracted from the single polarization TerraSAR-X SM and dual polarization TerraSAR-X HS and SL data. Based on the backscatter values and the corresponding measured biomass (dry matter) values, a linear regression equation was derived for the multi-temporal data and for each polarization at each date (TerraSAR-X). For regression analysis, the closest acquisition date to the respective field measurements was chosen (see Section 4.5.4).

If multi-channel data are acquired, it is valuable to contemplate rationing of the polarimetric bands (**polarimetric ratio**). Based on the HH and VV channel powers the ratio between both channels is calculated according to Woodhouse (2006):

$$R = \left(\frac{|S_{VV}|^2}{|S_{HH}|^2} \right) = \frac{\sigma_{VV}^0}{\sigma_{HH}^0} \quad (3.11)$$

By calculating the ratio, the relative properties of both polarizations are accentuated. Rationing can be treated as an indicator of geometric properties. As vegetation, especially rice vegetation, acts as a depolarizing scatterer, the ratio could be used for indication the vegetation cover and phenological stage.

3.2.3.3 Correlation

The polarimetric channels of the dual polarimetric TerraSAR-X data are acquired coherently which preserves their relative phase. This allows the calculation of new

channels like polarimetric phase difference (PPD) or inter-channel coherence as well as the computation of polarimetric decomposition.

From the complex data (imaginary and real) amplitude and phase information can be extracted from the backscattered signal, whereas the availability of phase information enables the calculation of the **polarimetric phase difference** (PPD). The polarimetric phase difference $\Delta\phi$ is calculated according to Ulaby et al. (1987):

$$\Delta\phi = \phi_{VV} - \phi_{HH} \quad (3.12)$$

As the measurement on a single pixel is quite noisy, the measurement is based on a window where amplitude pixel values are coherently averaged. Then the phase angle between the coherently averaged amplitudes pixels of HH and VV channels is computed according to equation 3.12. A phase difference other than zero could be caused by time delay due to various scatterers dominating HH and VV backscattering or time delay due to different extinction coefficient of HH and VV in the vegetation canopy (Ulaby et al. 1987). Based on this, the PPD points to the different scattering centre locations in HH and VV polarization. Also, the PPD is an indicator for the number of bounces an electromagnetic wave practiced during its way through the media. A phase difference of zero degree indicates an ideal odd-bounce (single bounce) reflection whereas an ideal even-bounce reflection has a phase difference of 180°. In the case of an agricultural environment the variation in co-polarimetric phase difference will be quite high, depending on size, density and orientation of the canopy (Woodhouse 2006).

The **co-polarimetric coherence** γ describes the degree of correlation between the co-pol channels (HH and VV). It is calculated between the complex amplitude of HH and the conjugate of the complex amplitude of VV. The value of the coherence is between 0 (incoherent) and 1 (fully coherent) and describes the polarization of the wave. If co-polarimetric coherence is unity (for instance from an ideal trihedral corner reflector), HH and VV are linear related, i.e. the backscatter of one polarization can be derived from the other (Woodhouse 2006). The co-polarimetric coherence can be formed by:

$$\gamma_{vvhh} = \frac{\left| \langle S_{HH} S_{VV}^* \rangle \right|}{\sqrt{|S_{HH}|^2 |S_{VV}|^2}} \quad (3.13)$$

3.2.3.4 Compact Polarimetric Decomposition

Dual polarimetric data can be exploited more efficiently by compact polarimetric decompositions, such as Alpha-Entropy (H2 α) decomposition of the HH-VV polarization mode. The coherent dual-pol H2 α decomposition was proposed by Cloude (2007) and is a modified form of the alpha-entropy decomposition developed by Cloude & Pottier (1997) for full polarimetric data. Instead of the reconstruction of the complete scattering matrix for full polarimetric data, with the dual polarimetric case one column of the scattering matrix can be reconstructed. Based on this partial scattering matrix, a 2x2 coherency matrix can be reconstructed. The decomposition is based on the eigenvector analysis of the coherence matrix $[T]$. The compact polarimetric eigenvalue decomposition is shown in the following equations (Shan et al. 2011):

$$T = \begin{bmatrix} T_{11} & T_{12} \\ T_{12}^* & T_{22} \end{bmatrix} = U \begin{bmatrix} \lambda_1 & \\ & \lambda_2 \end{bmatrix} U^H = \lambda_1 u_1 u_1^H + \lambda_2 u_2 u_2^H \quad (3.14)$$

where

$$U = \begin{bmatrix} u_{11} & u_{12} \\ u_{21} & u_{22} \end{bmatrix} = \begin{bmatrix} u_1 & u_1 \end{bmatrix} \quad \text{and} \quad u_i = e^{j\phi_i} \begin{bmatrix} \cos \alpha_i & \sin \alpha_i e^{j\delta_i} \end{bmatrix} \quad (3.15)$$

where λ_i are the real eigenvector, u the corresponding complex eigenvectors, H is the conjugate transpose, and $*$ denotes the conjugate. Entropy and alpha are defined as (Shan et al. 2011):

$$H = -\sum_{i=1}^2 P_i \log_2 P_i \quad (3.16)$$

$$\alpha = \sum_{i=1}^2 P_i \cos^{-1}(|u_{1i}|) \quad (3.17)$$

where

$$P_i = \frac{\lambda_i}{\sum_{j=1}^2 \lambda_j} \quad i = 1, 2 \quad (3.18)$$

The entropy is a function of the eigenvalues with a value range between 0 and 1. It is calculated by the sum of the $P_i \cdot \log_2 P_i$ (equation 3.16), whereas P_i is defined as the eigenvalue λ_i divided by the sum of the eigenvalues (equation 3.18). It defines the randomness of scatterers of averaged pixel. Scattering can be considered as pure (single scattering mechanism, e.g. single bounce) if entropy is zero. Entropy values close to 1 indicate that scatterers are basically random (e.g. volume scattering); there is no dominant scattering mechanism. If entropy is high, it is believed that there are at least two scattering mechanism present.

The alpha angle ranges between 0 and 90° and is an indication about the dominant scattering mechanism present in averaged pixel. According to Touzi et al. (2004), the alpha angle value range can be divided into three main scattering mechanisms. An alpha angle close to zero represents an ideal odd-bounce (single bounce) scattering, alpha around 45° denote dipole scattering and alpha close to 90° represent even-bounce scattering (dihedral). In a natural environment the alpha angle remains vague as the transition between these distinct categories is smooth. According to the theory surface scattering from a smooth surface has an alpha angle close to zero, volume scattering can be between 30° to 70° and double bounce scattering is higher than 50°.

3.2.4 Statistical Analysis*

Beside the understanding of hyperspectral reflectance and microwave backscatter behaviour of crop during the vegetation period, a major objective of this study is the derivation of biophysical crop parameters by remote sensing data. For this, the recorded signal either by the hyperspectral instrument or by the SAR antenna is related to biophysical parameters by a linear regression of the form (Schoenwiese 2006):

$$y = ax + b \quad (3.19)$$

with y the random variable to predict, x the random variable y is predicted from, a is a coefficients corresponding to x and b a constant value. The linear regression function calculates the best fit of a straight line by using the least square method.

* This section is an extended version of the article: Koppe et al. (2013).

In this bivariate regression equation y is the biophysical parameter to be estimated (dependent variable) and x the independent variable provided by the remote sensing data (e.g. backscatter value or vegetation index). To relate several independent variables with one dependent variable, a multiple regression equation can be formed:

$$y = a_1x_1 + a_2x_2 + \dots + b \quad (3.20)$$

with y the random variable to predict, x the random variable y is predicted from, a is a coefficients corresponding to x and b a constant value.

The performance of the derived models; i.e. the strength of the relationship between the independent variables and dependent variable can be measured by the coefficient of determination (R^2). For R^2 the variability of the samples of the data set is measured by the sum of the squares and the range of values is between 0 and 1 (with 1 as the best fit).

$$R = \frac{SS_R}{SS_T} \quad (3.21)$$

where SS_R defines the regression sum of squares and SS_T defines the total sum of the squares. In addition, this performance was quantified by root mean square error (RMSE) and relative error (RE in %). The evaluation of the accuracy estimation was carried out using leave-one-out cross validation (Allen 1974). For this purpose, each plot was left out once from the reference data set and the crop variable estimates were calculated using the remaining plots. The higher the R^2 coefficient of the regression approach is, the higher the level of significance, resulting in a higher accuracy of the model. A RMSE of zero means that the model estimator \hat{y}_i predicts the observed parameter biomass y_i with best accuracy. The RMSE and RE are calculated using the following equations:

$$RMSE = \sqrt{\frac{1}{n} \sum_{i=1}^n (y_i - \hat{y}_i)^2} \quad (3.22)$$

$$RE[\%] = \frac{100}{\bar{y}} * RMSE \quad (3.23)$$

where y_i , \hat{y}_i and \bar{y}_i , are measured, predicted values, and the mean of the measured values, respectively.

4 RESULTS

4.1 Crop Phenological Development

4.1.1 Winter Wheat Growth*

As already mentioned, the dominant cropping system in the Huimin County is the summer maize – winter wheat rotation system. Following this system, the winter wheat is sown in October and harvested in June of the subsequent year. The growing period is between March and May, where the fields are irrigated by the farmers.

To describe and compare the phenological stages of the winter wheat, the growth status can be generalized to a standard winter wheat growth cycle. In the recent study, the phenological stages of winter wheat in the test area Huimin are assigned to the stages of the BBCH-scale (Biologische Bundesanstalt, Bundessortenamt and Chemische Industrie), which is uniform coding of phenological stages (Meier 2001). This standardized scale separates the development stages by a decimal code, which consists of a principle and a secondary growth stage.

The sowing time of the winter wheat for the vegetation period of 2006 and 2007 was in each case in September to October of the previous year. During the seedling development and early tillering the first plant leaves appear and the tillers start to emerge. Ground truth campaigns in 2006 and 2007 started at the end of the tillering when the wheat plants change from vegetative to reproductive stage. With the beginning of the jointing stage the internode region starts to elongate; later the flag leaf appears. Inside the hull of the flag leaf, the head develops and emerges at the booting stage. During the subsequent heading stage, the head emerges fully and development of the head is completed. Within the anthesis stage, the plants are flowering and pollination occurs. After this, the kernel forms, grows and accumulates a large part of the total weight of the plant. During the last stage, the ripening stage, which can be subdivided into milky and dough stage, the plant loses most of its moisture. The winter wheat is harvested at the beginning of June.

* This section is an extended version of the articles: Koppe et al. (2010a); Koppe et al. (2012).

Due to different farmers' management practices, the investigated fields were different in terms of seeding time, plant density, and nitrogen application rates. As expected, the differences in management practices resulted in a wide range of variation in crop parameters (aboveground biomass, plant nitrogen concentration, and plant height). In 2006, the within-field variation of plant height and aboveground biomass at the jointing stage (heading stage) ranged from 31.3 to 51 cm (70.3 to 90 cm), and from 0.19 to 0,79 kg/m² (0.72 to 1.55 kg/m²), respectively (see Table 4-1). Plant nitrogen concentration varied from 17.1 to 37.42 g/kg at the jointing stage and from 13.1 to 19.5 g/kg at the heading stage. The decrease of plant nitrogen concentration during the vegetation period is due to dilution effect.

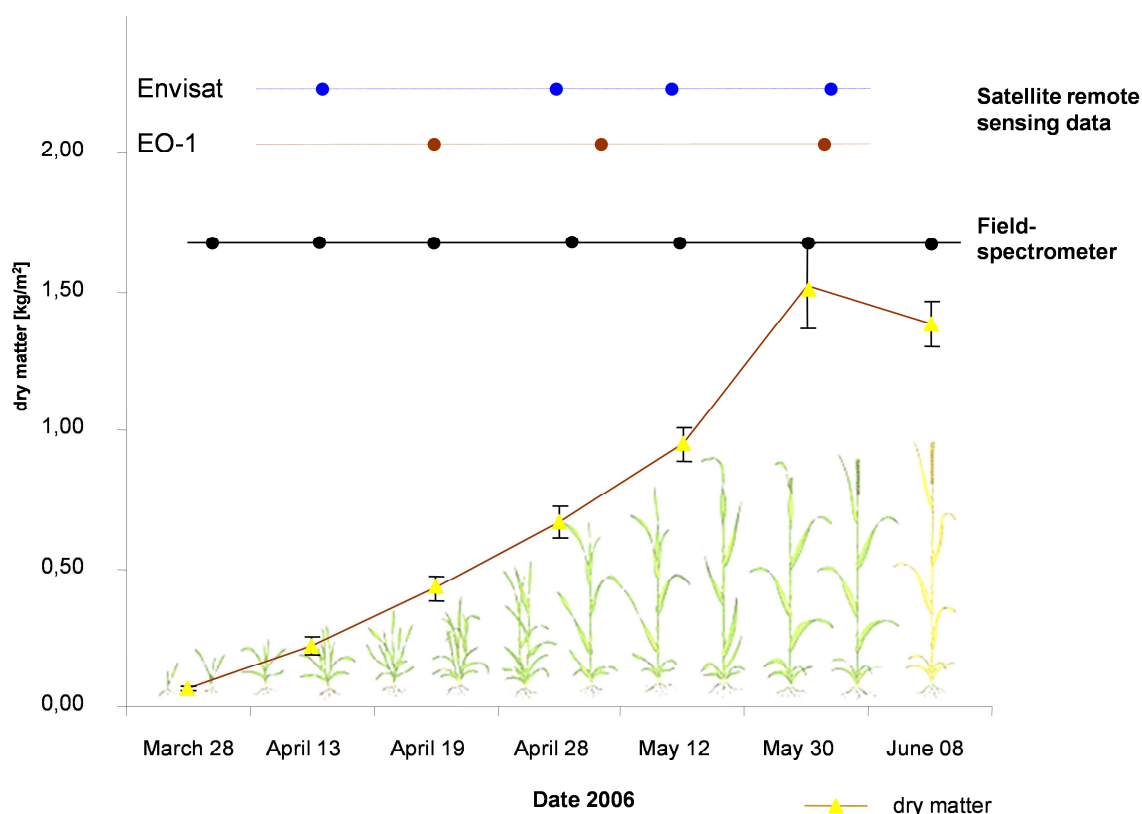


Figure 4-1: Biomass development of winter wheat in 2006 and dates of image and ground truth acquisition.

The average biomass development of winter wheat in the season 2006 from March to June is depicted in Figure 4-1. Additionally to the increase in dry matter, the satellite acquisition dates of Envisat ASAR and EO-1 Hyperion / ALI and the terrestrial spectral reflectance acquisition dates are shown.

Table 4-1: Crop growth variables measured at different dates in 2006 and 2007 (Koppe et al. 2012).

Date	BB CH	Growth stage	Biomass dry [kg/m ²]		Plant height [cm]		PWC*	
			Mean	STD	Mean	STD	Mean	STD
March 25, 2006	29	tillering	0.06	0.03	11.4	1.9	73.2	1.5
April 13, 2006	31	jointing	0.21	0.05	36.8	2.8	82.3	0.6
April 19, 2006	35	jointing	0.48	0.05	45.0	4.8	83.9	1.4
April 29, 2006	41	booting	0.74	0.09	54.9	5.6	83.5	1.2
May 12, 2006	51	heading	0.96	0.07	74.5	5.5	76.3	1.7
May 30, 2006	75	ripening	1.51	0.12	76.2	6.1	66.7	1.8
April 11, 2007	31	jointing	0.43	0.04	41.4	4.8		
April 21, 2007	35	jointing	0.62	0.07	64.6	6.0		
May 6, 2007	41	booting	1.05	0.08	93.4	5.8		

* Plant water content

As remote sensing is the focus in the recent study, the spatial temporal distribution of crop growth within the fields is an essential parameter. Figure 4-2 shows the winter wheat development at six different stages from March 2006 to May 2006.

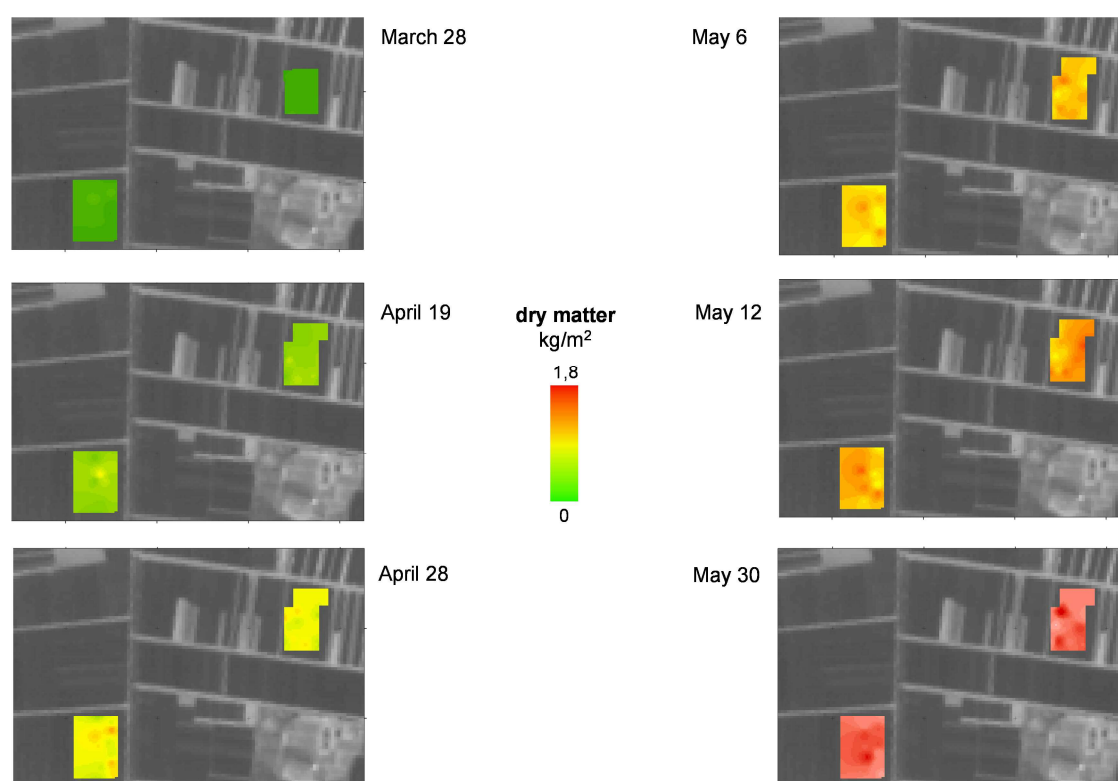


Figure 4-2: Spatial-temporal distribution of dry matter of two fields in 2006.

4.1.2 Rice Growth

The main management steps in rice cropping system of the Jiansanjiang test site are the planting, the transplantation and the harvesting (see Figure 4-3). The ground truth campaign at the Qixing farm lasted from the end of June to the end of August.

To interpret radar response from the rice at different growing stages, the understanding of phenology of rice plants is essential. In general, the complete life cycle of rice in the Sanjiang Plain region is passed through the germination in rice nurseries and growth in the greenhouse until leaf development within 25-30 days and the main growth in flooded paddies within 110 to 130 days. The growing period of rice is divided into three main sequences of growing (Yoshida 1981):

- the vegetative period, which includes the stages from germination and emergence, transplantation, tillering and stem elongation to panicle initiation
- reproductive period, which includes the stages booting, heading and flowering
- ripening period, which includes the stages milky, dough and maturity

The vegetative period starts with the sowing and continues until the beginning of the panicle initiation. Before transplantation, the plants are sown in rice nurseries and the fields are flooded with varying water depth between 5 to 20 cm. Around 25 to 30 days after germination, the seedlings are transplanted in clusters of 4 to 5 seedlings into the flooded rice fields. The vegetative period is characterized by the leaf development, the tillering and the panicle initiation. In this period a strong increase in height and density of the plants occurs and they stay mainly erectophile. The vegetative stage lasts until around DAT 50. The subsequent reproductive stage starting with the panicle initiation is characterized by a further strong increase in stem height by culm elongation until the heading stage. Also the flag leaf appears and the stem is slightly thickened. After heading stage when panicle emerged completely, increase in plant height is strongly reduced and flowering begins. The last sequence of rice growing period is the ripening stage, which is dominated by a decrease in moisture content, senescence of leaves and an increase in heads weight. In this period the orientation of the leaves is more

randomly than erectophile as in the previous sequences. The ripening stage ends with the harvest.

Table 4-2: Statistics of measured agronomic parameters during the field campaign 2009 (modified after Koppe et al. 2013).

			Date	Jun 27	July 9	July 25	Aug 5	Aug 25	Sep 24
			DAT	38	50	66	77	97	126
24 detailed sampled plots	Total biomass [t/ha]	Mean		1.8	3.0	6.1	7.9	12.4	14.8
		Min		0.7	2.2	2.3	6.1	9.9	10.6
		Max		2.4	4.4	7.6	10.6	15.7	20.3
		STD		0.47	0.64	1.1	1.2	1.4	2.0
	Stem [t/ha]	Mean		0.93	1.74	-	4.92	-	4.8
	Leaf [t/ha]	Mean		0.86	1.29	-	1.6	-	1.41
	Head [t/ha]	Mean		-	-	-	1.32	-	8.04
All other plots	Total biomass [t/ha]	Mean		1.2	2.5	-	5.3	10.5	14.7
		Min		0.4	1.0	-	2.0	4.6	9.4
		Max		3.0	5.9	-	12.1	18.0	20.3
		STD		0.6	0.9	-	2.5	3.0	2.6
	Plant height [cm]	Mean		43	55	76	87	97	95
		Min		31	43	61	75	82	80
		Max		52	69	83	97	105	101
		STD		4.0	6.6	5.8	6.4	6.1	6.0
	LAI	Mean		2.18	2.82	3.85	-	3.5	-
		Min		0.63	1.6	1.8	-	1.8	-
		Max		3.5	5.8	6.6	-	5.3	-
		STD		0.7	0.9	1.32	-	0.94	-
	Yield [t/kg]	Mean		-	-	-	-	-	7.9
		Min		-	-	-	-	-	4.5
		Max		-	-	-	-	-	13.2
		STD		-	-	-	-	-	1.5

Table 4-2 shows a summary of the measured crop parameters in 2009 of all 80 plots and separately the 24 plots which were sampled in more detail. Total biomass was acquired at six different dates, at four dates the plants were separated into sub plant organs. For DAT 38 and 50 the plants were separated into stems and leaves, after heading also the heads were treated separately at DAT 77 and 126. Additionally to biomass measurements, the plant height at all dates and LAI at four dates were measured. According to the measured values of the different parameters, the within-field and field-to-field variability of the plots is very high. From tillering to harvest the

total dry biomass increased from 1.2 t/ha to 14.7 t/ha whereas the standard deviation also increased.

Table 4-3: Information about field experiments in 2009 and 2011.

Year	Cultivar	Density (hills/m ²)	Plant date	Transplantation date	Harvest date
2009	8 different		April 4	May 20	September 26
2011	Kendao6	28	April 15	May 16	September 21

Also plant height is increasing from tillering (43 cm) to ripening (97 cm), whereas at harvest the plant height slightly decreased due to drying and hanging down of the panicle. The course of plant height and total biomass at the different phenological stages is also depicted in Figure 4-3. The growth of rice can be divided into three main phenological phases – the vegetative phase, the reproductive phase, and the ripening. The vegetative phase lasts from sowing to booting with further subdivision into transplantation, tillering, and stem elongation. With the heading the reproductive phase starts and continues until flowering around DAT 100. Thereafter the ripening completes the rice growth cycle. Spatial distribution and variation of total biomass at different dates and final yield in 2009 are shown in Figure 4-4.

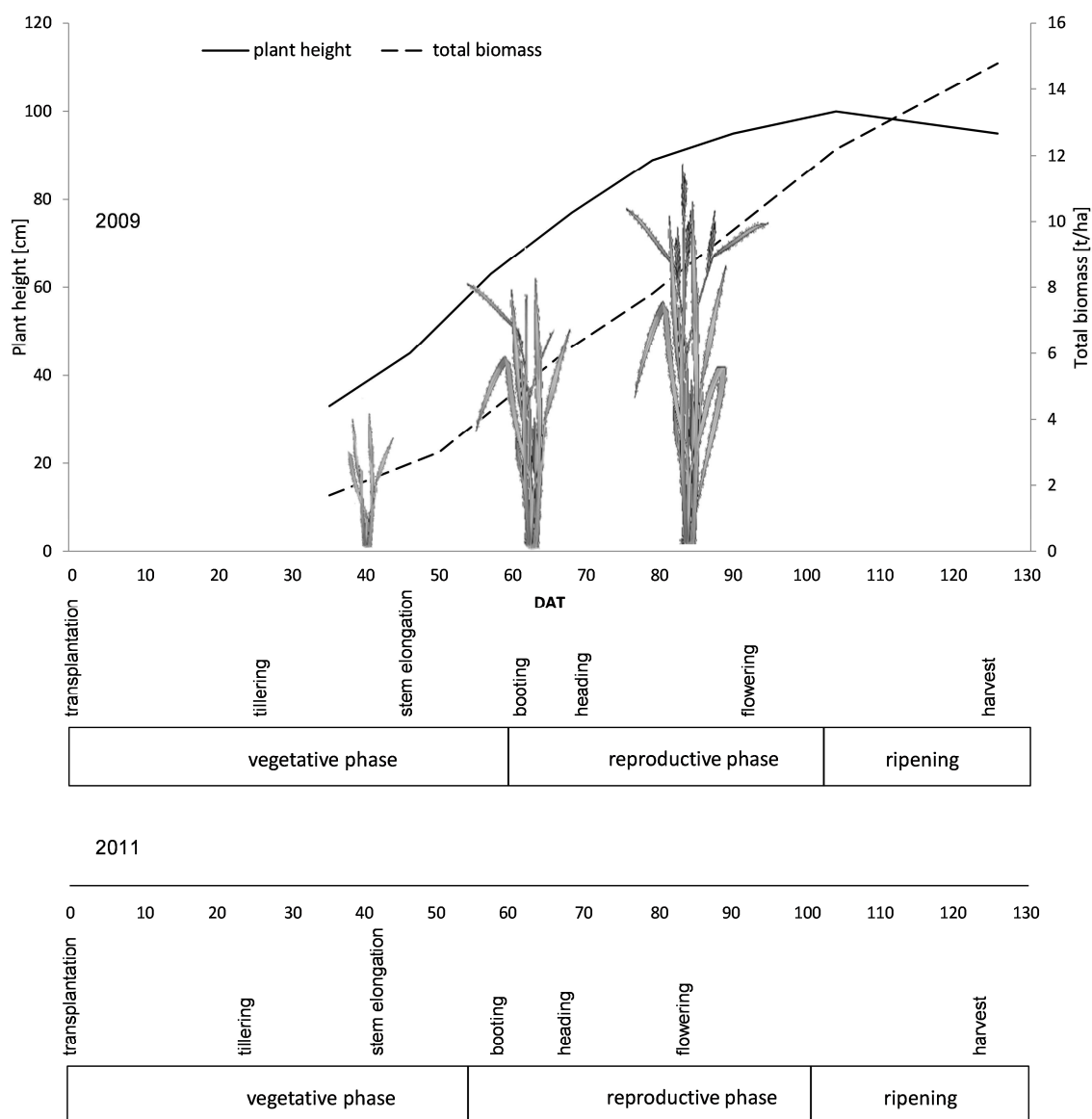


Figure 4-3: Rice growth stages, growth phases as well as plant height and total biomass graphs of the growing season of 2009 and 2011. Time is represented in days after transplantation (modified after Koppe et al. 2013).

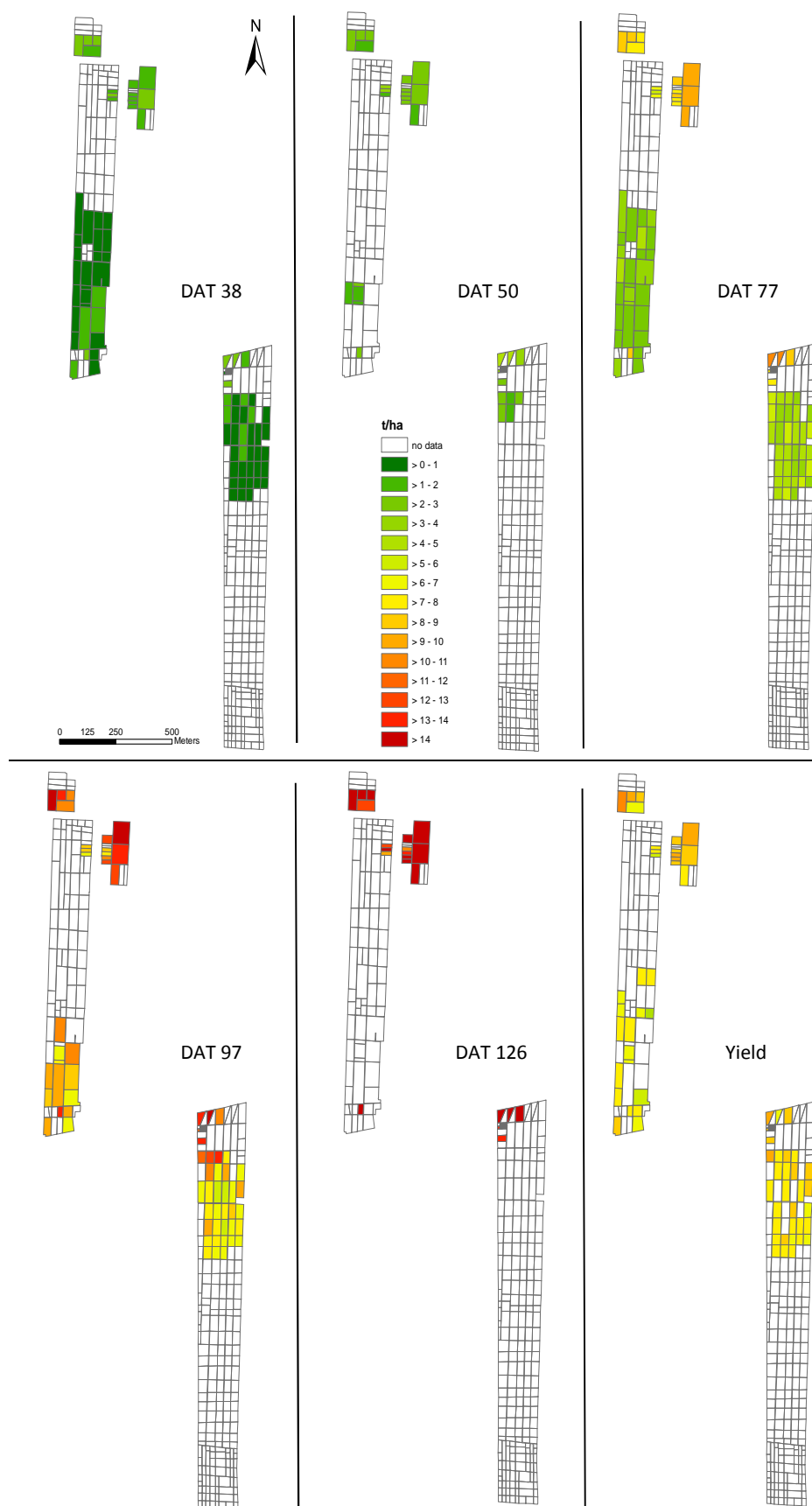


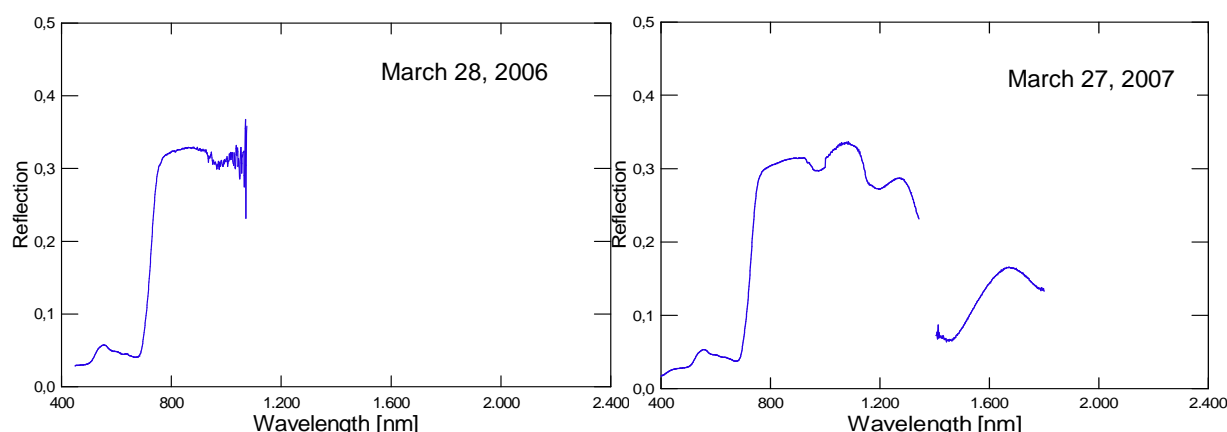
Figure 4-4: Total dry matter and yield measured at the farmers' fields. Fields with biomass measurements and plots with detailed sampling.

4.2 Hyperspectral Imaging of Winter Wheat

4.2.1 Spectral Reflectance as a Function of Crop Parameters*

The phenological development of winter wheat can be retraced by the multi-temporal reflectance profile. By using the results from regular in-situ spectral reflectance measurements with Fieldspec (ASD) in 2006 and QualitySpec (ASD) in 2007, the reflectance characteristic of winter wheat during the growing seasons was determined and is illustrated in Figure 4-5 (blue lines). Additionally, the reflectance signatures of EO-1 Hyperion acquisitions are drawn in the diagrams (red lines). Due to different satellite acquisition and field measurement dates in 2006 and 2007, the dates of the diagrams in the figure do not fit together properly. Because the QualitySpec measurements in 2007 cover almost the same spectral range as EO-1 Hyperion, the spectral reflectance of winter wheat is explained exemplarily by the 2007 data. The data of 2006 is for completeness.

The energy reflected by plants is influenced by crop conditions such as growth stage (biomass, plant density, plant height) and nutrient supply but also by leaf geometry, angle and shadowing. These parameters are varying during the growing season which has an impact on the reflected energy at different parts of the electromagnetic spectrum. At the beginning of the vegetation period in March, the soil is covered by small plants, whereas the percentage vegetation coverage is very low. The reflectance spectrum is a mixture of soil and vegetation reflectance.



* This section is an extended version of the article: Koppe et al. (2012).

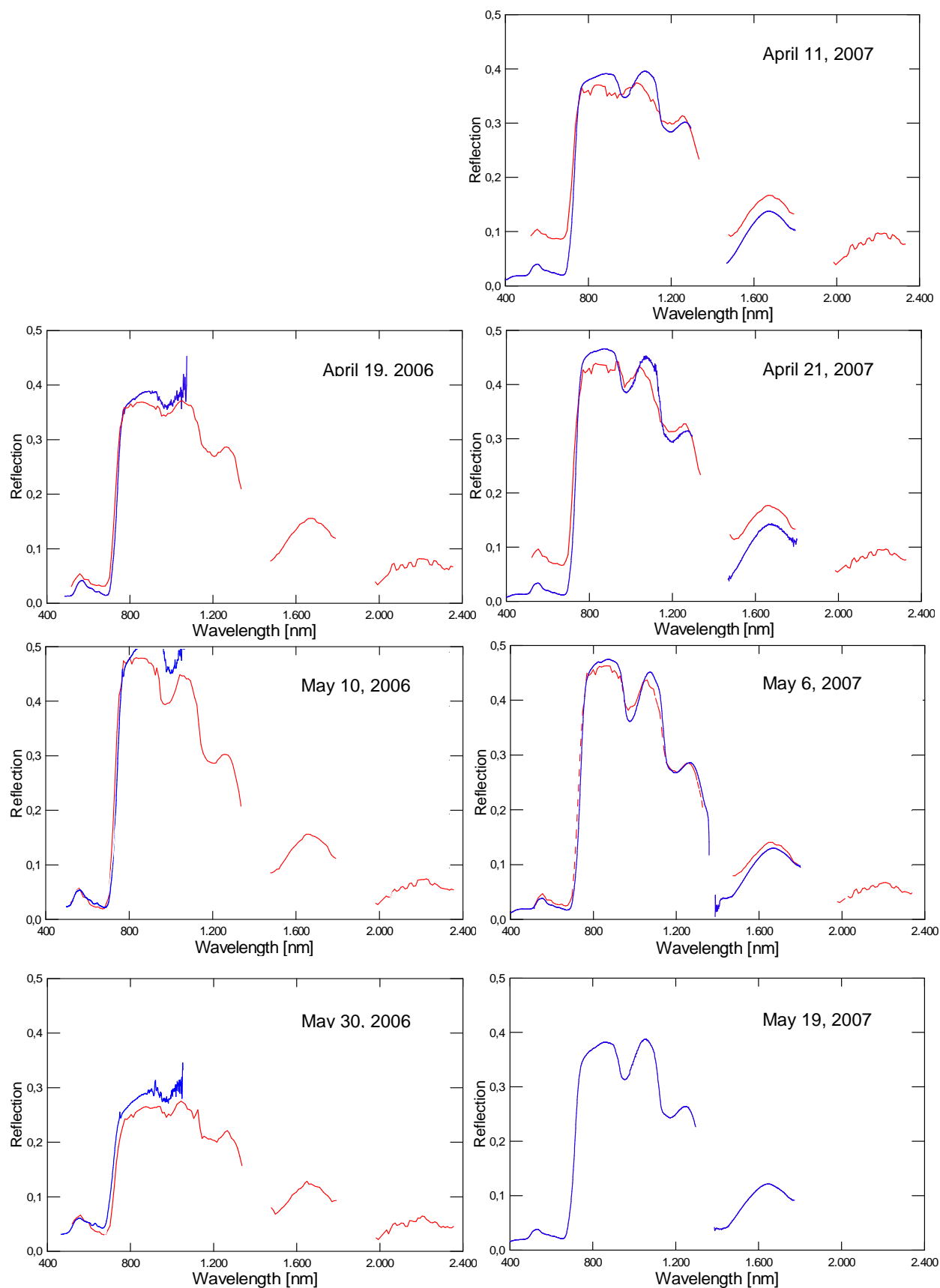


Figure 4-5: Reflection behavior of winter wheat (Xili). Left: recorded by ASD Fieldspec (blue) and EO-1 Hyperion (red) in 2006. Right: recorded by QualitySpec (blue) and EO-1 Hyperion (red) in 2007 (extended after Koppe et al. 2012).

Throughout the measurements from jointing (mid of April) to ripening stage (end of May), the reflectance behaviour alters due to structural changes as well as changes in foliar pigments (Kumar et al. 2003). Up to heading stage (beginning of May) the reflectance in the red spectrum (650 to 700 nm) decreases, which is due to increasing absorption by foliar pigments in the red spectrum. While reflected energy in the red spectrum reduces, reflectance in the near infrared (NIR) increases caused by the fast development of structural components of the plants (Thenkabail et al. 2000). The maximum reflectance difference between red and NIR is reached at the end of April (booting). With the beginning of May, the divergence of red and NIR reflectance decreases again. A slightly different behaviour of spectral reflectance is recorded between NIR (875 nm) and SWIR (1225 nm). The divergent trend between the two wavelengths continues up to the heading stage (beginning of May) which delays the saturation effect of crop parameter estimation at full canopy cover (Mutanga & Skidmore 2004). At the end of May, the reflection in NIR is strongly decreasing due to senescence (see Figure 4-5, lower right). The linear relationship of NRI with biomass is lost at this time.

The 2006 EO-1 Hyperion data is in good consistence with in-situ field spectrometer measurements (Koppe et al. 2010a) due to good atmospheric conditions during the satellite overpass. Also, the 2007 spectral reflectance from Hyperion and in-situ measurement matches well; the courses of both reflectance curves at a given date are similar in a certain range. Differences can be observed on April 11 and April 21 in the visible and near infrared parts of the spectrum. For these dates hazy conditions with different spatial intensities affected the acquisitions. As a consequence the high absorption (VIS) and maximum reflection (NIR) parts of the spectra are more damped. Especially in the VIS the spectra differ significantly. This part of the electromagnetic spectrum is particularly affected by hazy atmospheric conditions (Kumar et al. 2003), and atmospheric correction of the scenes phased problems. For the last satellite acquisition at the beginning of May, the measured spectra fit to the in-situ measurements.

4.2.2 Spectral Vegetation Indices and the Relationship with Crop Parameters*

In the following section the relationships between crop variables and different types of reflectance indices are presented. Among them are single band reflectance, standard vegetation indices with broad and narrow bands and narrow band Normalized Ratio Index (NRI), involving all possible two-band combinations. However, the focus is set on the NRI and its validation.

Table 4-4: Coefficient of determination (R^2) between ALI broad band, Hyperion narrow band vegetation indices and measured agronomic parameters (Koppe et al. 2010a).

Sensor	Index	ALI band / Hyperion wavelength			R^2		
		λ_1	λ_2	λ_3	Biomass	Plant N	Plant height
Hyperion single band		732			0.51		
		732				0.40	
		732					0.52
ALI broad band	SR	Red (4)	NIR (5)		0.35	0.25	0.41
	NDVI	Red (4)	NIR (5)		0.4	0.28	0.43
	OSAVI	Red (4)	NIR (5)		0.55	0.21	0.49
	TVI	Red (4)	NIR (5)	GREEN (3)	0.69	0.32	0.64
Hyperion narrow band	SR	671	803		0.41	0.3	0.41
	NDVI	671	803		0.41	0.29	0.4
	OSAVI	671	803		0.58	0.22	0.56
	TVI	671	803	549	0.71	0.33	0.65
Hyperion best waveband combinations	NRI ₁	874	1225		0.83		
	NRI ₂	732	1305			0.81	
	NRI ₃	763	1225				0.79

4.2.2.1 Single Band Relationship with Crop Parameters

As a first analysis, spectral reflectance of the 158 Hyperion individual bands was correlated with biophysical parameters. Figure 4-6 shows the correlation (r) between narrow Hyperion bands and standing biomass. High negative correlation values occur

* This section and sub-sections are an extended version of the articles: Koppe et al. (2010a); Koppe et al. (2012).

in the blue and in the red bands, but also between 2000 and 2400 nm. The blue and red part of the spectrum is characterized by high energy absorption due to the presence of chlorophyll. The absorption increases with increasing amount of chlorophyll (increasing LAI). In the red edge portion the reflection of green vegetation increases dramatically from red to the near infrared as chlorophyll absorption is not present. Related to this increase in reflection, correlation values change from negative to positive reaching highest r at the red edge inflection point (732 nm) as well. At the near infrared shoulder the correlation stays nearly constant. A minor decrease in r occurs near the moisture trough at 950 to 1040 nm. Beyond 1100 nm the correlation between single band reflectance and biomass decreases since also the amount of energy reflected off the crop canopy decreases.

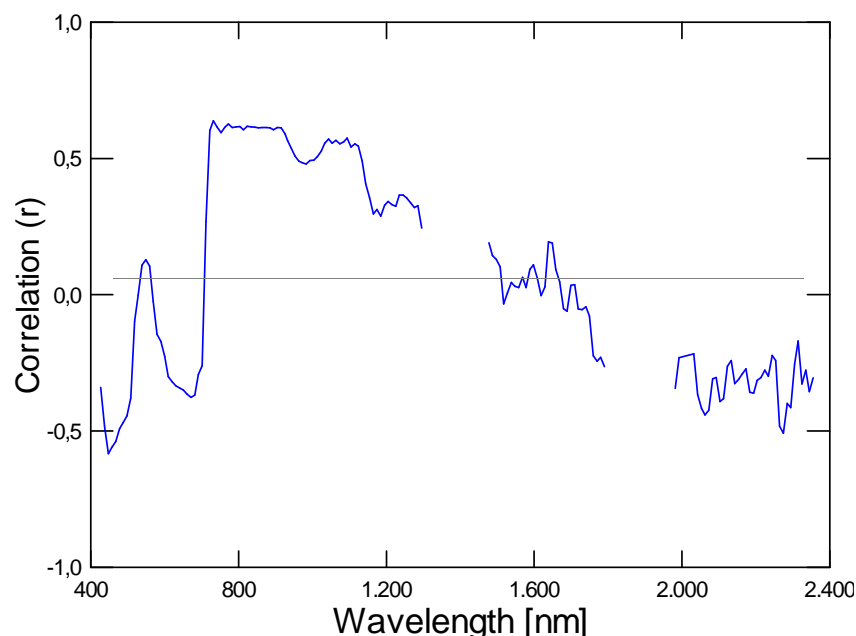


Figure 4-6: Correlation coefficient (r) between Hyperion single band reflection and biomass in the growing season of 2006.

4.2.2.2 Standard Broad Band and Narrow Band Vegetation Indices

Relationship of standard vegetation indices with crop parameters is well described in the literature. EO-1 ALI broad band indices serve as benchmark indices for comparison with narrow band standard vegetation indices and NRI, with the last two categories of vegetation indices based on EO-1 Hyperion data.

The relationships of the different vegetation index types (broad band and narrow band) with the three crop parameters showed different results. Best individual R^2 values for broad band and narrow band standard vegetation indices were achieved for TVI (Table 4-4). The narrow band TVI has high coefficient of determination values for aboveground biomass ($R^2 = 0.71$) and plant height ($R^2 = 0.65$), but low values for plant nitrogen concentration ($R^2 = 0.33$). NDVI generally has lower R^2 values than TVI. Narrow band vegetation indices did not improve the relationships significantly compared with broad band vegetation indices. None of the evaluated broad or narrow band vegetation indices performed well for plant nitrogen concentration, with R^2 being less than 0.35 (Table 4-4).

4.2.2.3 Relationship of Narrow Band Normalized Ratio Indices (NRI) with Crop Parameters

A total number of 9870 narrow band NRIs according to equation 3.4 were calculated from multi-temporal Hyperion data acquired in 2006. Correlation matrices between each agronomic parameter and two-band vegetation indices were constructed. In each correlation matrix, the wavelengths of the two bands were plotted on the x- and y-axes and the classified coefficients of determination (R^2) between crop parameters and all possible two-band vegetation indices were plotted on a colour scale (Figure 4-7).

The correlation matrices are only displayed below the diagonal because R^2 values are symmetrical. The R^2 values for aboveground biomass and plant nitrogen concentration ranged from 0.08 to 0.83, and several clusters of high R^2 values could be recognized in the two matrix plots (Figure 4-7). Wavebands used for broadband NDVI calculation from the red and near infrared spectrum (which match red and near infrared ALI bands), are labelled in the matrix plot. This area shows very low correlation coefficients R^2 compared to waveband pairs forming the clusters with high correlation coefficients. Best center wavelengths of band 1 and band 2 for these patches for aboveground biomass estimation were extracted from the matrices and listed in Table 4-4. Following the same approach, best waveband pairs and bandwidth were determined for the estimation of plant nitrogen concentration (Figure 4-7b; Table 4-4). Similar to aboveground biomass, best waveband centers were not located in the R and NIR spectrum. The best values of NRIs for aboveground biomass, plant N concentration and plant height were 0.83, 0.81 and 0.79, respectively. The selected wavebands were

centred at 874, 732 and 763 nm for band 1, and 1225 and 1305 nm for band 2 with bandwidth between 10 to 30 nm (Table 4-4).

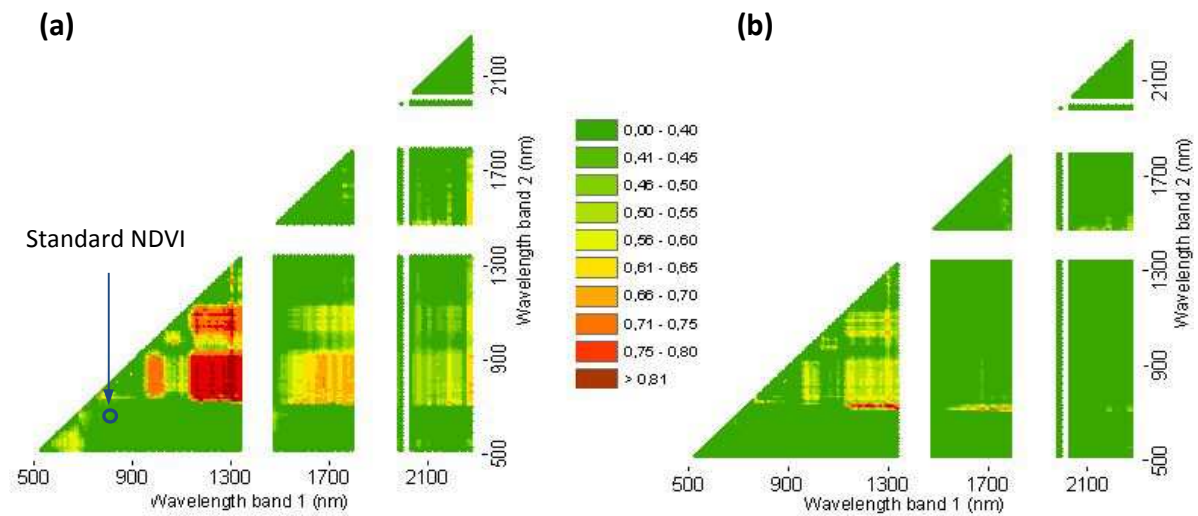


Figure 4-7: Coefficient of determination (R^2) between Hyperion narrow band vegetation indices calculated from all possible two-band combinations and biomass (a) and total nitrogen content (b) (Koppe et al. 2010a).

Similar approaches for different types of vegetation cover showed that band combinations of the red edge (Zhao et al. 2007) as well as NIR or SWIR (Mutanga & Skidmore 2004, Xavier et al. 2006) provided a close relationship with LAI and aboveground biomass. These approaches performed much better than spectral bands used in standard vegetation indices. Based on the best waveband combination, a model for biomass estimation was established according to equation 3.19 which resulted in a coefficient of determination (R^2) of 0.83:

$$BIOM_{2006} = 0.25(NRI_{2006}) - 0.01 \quad (4.1)$$

The scatterplots of narrow band NDVI and NRI is depicted in Figure 4-9.

4.2.2.4 Validation of NRI model

In order to prove the stability of the established hyperspectral model for EO-1 Hyperion data during the 2006 growing season (see equation 4.1) a validation analysis using EO-Hyperion data for the 2007 growing season was performed. For this, NRI was calculated based on the same waveband combination (875 nm and 1225 nm) that

were used in 2006. The resulting NRI values of acquired hyperspectral images in 2007 (April 11, April 21 and May 6) were used to predict biomass at the acquisition dates. The applied equation is the model developed in 2006 (equation 4.1):

$$BIOM_{2007(pred)} = 0.25(NRI_{2007}) - 0.01 \quad (4.2)$$

The validation results of the model are divided into mono-temporal and multi-temporal approach (see Table 4-5). For the model based on a single date, the correlation coefficients R^2 vary between 0.19 and 0.58 with relative errors between 45% and 18%.

The multi-temporal validation result of the model is shown in the 1:1 plot in Figure 4-8. The model developed for 2006 is able to predict also accumulated biomass in 2007, which is confirmed by a high coefficient of regression of the 1:1 plot ($R^2 = 0.84$). Furthermore, the result is clustered into three separate point clouds that correspond to the different acquisitions of Hyperion data. The acquisitions from April 11 and April 21 show a slight underestimation of the biomass in comparison to the last acquisition of May 6.

Table 4-5: Coefficient of determination (R^2) between biomass and NRI for the validation model based on multi-temporal and mono-temporal data (modified after Koppe et al. 2012).

Year	Input data typ	Input acquisitions (date)	n*	R^2	RMSE (kg/m ²)	RE (%)
2007	hyperspectral	Apr 11, Apr 21, May 6	113	0.84	0.12	17.2
		Apr 11	41	0.19	0.18	45.5
		Apr 21	33	0.58	0.18	29.8
		May 6	39	0.42	0.22	18.2

*n – number of used samples

This could be due to atmospheric distortions (haze) that affect the reflection from the surface. The difference between the used Hyperion wavebands (875 nm and 1225 nm) for the April scenes is lower than for field measurements (Figure 4-5). This lower waveband difference results in a lesser NRI that leads to an underestimation of the standing biomass in equation 4.2.

In spite of haze influence during the acquisition of EO-1 Hyperion data in April, the stability of the model established for 2006 and applied to 2007 can be regarded as applicable for winter wheat on regional scales in the North China Plain. Changing the scale from regional to local scale, a successful inter-year validation of the developed regression model using field spectrometer data from two years and different cultural conditions was performed by Li et al. (2008). These observations suggest an across scale validity of hyperspectral crop parameter estimation models in the North China Plain.

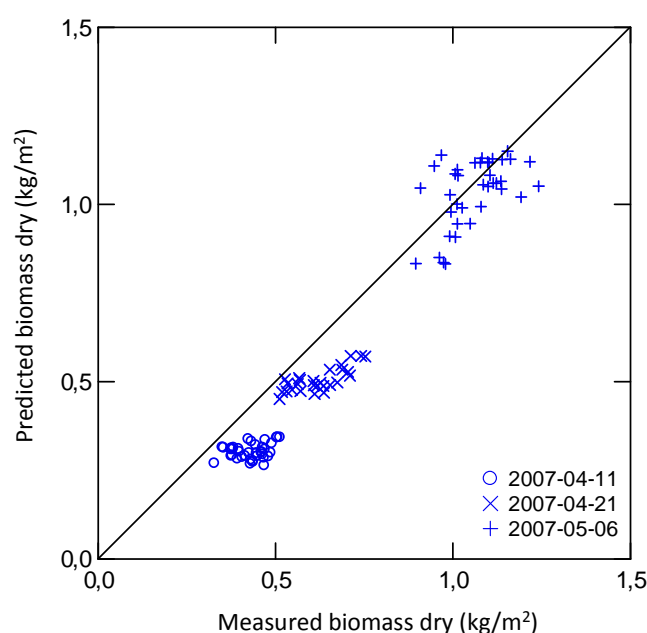


Figure 4-8: Measured versus predicted aboveground biomass using the regression model described in equation 4.2 (Koppe et al. 2012).

4.2.3 Discussion of Multispectral and Hyperspectral Data for Winter Wheat Monitoring*

4.2.3.1 Processing of EO-1 Data

For the presented study Hyperion and ALI Level 1R data were used which are radiometrically corrected with no geometric correction applied (USGS 2007). This low level of correction assures no resampling and gives the possibility to bear a complete pre-processing chain to retrieve surface reflectance from at-sensor radiance measured with ALI multispectral and Hyperion hyperspectral sensor. Several authors (Biggar et al. 2003, Datt et al. 2003, Coops et al. 2003) pointed out the importance of correction of

* This section and sub-section are an extended version of the article: Koppe et al. (2010a).

artefacts or atmospheric effects. A full processing chain for EO-1 Hyperion data was described by Khurshid et al. (2006). In comparison to Khurshid et al. (2006), the misregistration of VNIR and SWIR wavebands, which include spatial and angular shift, has been solved by a co-registration of the wavebands from the two VNIR and SWIR detectors. Due to the lack of detailed atmospheric information, the atmospheric correction was performed with a standard atmosphere implemented in FLAASH (ENVI). The applied atmospheric correction resulted in a good agreement with ASD field data that were taken close to satellite overpass. Similar correction method and observed results were presented by Datt et al. (2003) as well as by Chen & Tian (2006).

4.2.3.2 Single Band and Standard Vegetation Indices

In the first step, a correlogram of single EO-1 Hyperion bands against crop variable was constructed. The correlogram shows the individual performance of narrow bands by relating to crop variables. This is not a normalized index that can contribute to crop parameter estimation; however, it is an indication about sensitivity of individual bands and can be used for the reduction of the number of input bands for band combination calculation (Hansen & Schjoerring 2003).

Subsequent to this, three different two-band indices (SR, NDVI, OSAVI) and one three-band index (TVI) were compared in order to evaluate the capability of broad band and narrow band standard vegetation indices for crop parameter estimation. The narrow bands of Hyperion Sensor for these indices were centered at green (559 nm), red (681 nm) and near infrared (803 nm) with a bandwidth of 10 nm. The corresponding ALI broadband channels were 4, 5 and 6 with a bandwidth between 40 and 80 nm.

Comparing vegetation indices based on different sources (ALI and Hyperion), only a slight improvement of hyperspectral narrow bands was observed for the three measured crop variables compared to broad band indices. Similar results were found by Zhao et al. (2007) and Lee et al. (2004), who tested the ability of different multispectral airborne and orbital sensor data for LAI prediction in an agricultural environment. Also Hansen & Schjoerring (2003) found a slightly improved performance of narrow bands for biomass and nitrogen status of wheat crops. On the contrary, Broge & Mortensen (2002) and Broge & Leblanc (2000) showed that hyperspectral vegetation indices did not perform better than their simulated multispectral

counterparts. Whether broad or narrow bands were used, the standard vegetation indices had limited capability for crop parameter estimation due to canopy closure at high plant densities, which was also observed in the recent study. This saturation effect of standard vegetation indices at high canopy cover is evident for multispectral space based imaging (Tucker 1979), airborne hyperspectral imaging (Oppelt & Mauser 2004), and ground-based measurements. Due to this asymptotic saturation of spectral reflectance in the course of the vegetation period, standard vegetation indices become less effective measurements (Mutanga & Skidmore 2004). The small increase of the slope in Figure 4-9a for standard NDVI indicates the asymptotic saturation effect for biomass estimation. To overcome the saturation effect, narrow band vegetation indices based on different parts of the electromagnetic spectrum can be used in biomass modelling.

4.2.3.3 Narrow Band Normalized Difference Indices

The performance of calculated band ratios that are widely used and readily adaptable in vegetation studies (Schowengerdt 2007, Gong et al. 2003, Thenkabail et al. 2000) were evaluated. The results in Figure 4-7 show, that the two-band combinations respond in a wide range to variations in biomass. High coefficients of determination (R^2) between narrow band indices and aboveground biomass are mainly clustered in the red edge, NIR and the SWIR spectra domain. These wavebands are centered in the red edge (720 nm), the NIR peak (874 nm) as well as in the SWIR (1225 nm and 1750 nm) with varying spectral range between 10 and 180 nm. Similar findings for biomass estimation are summarized in Thenkabail et al. (2004) and Mutanga & Skidmore (2004). These spectral regions of the NIR peak and the SWIR in the electromagnetic spectrum are among others sensitive to plant water content (Kumar et al. 2003), and consequently they have a close relationship to biomass. The best waveband combination for estimating aboveground biomass was obtained using wavebands centered at 874 nm and 1225 nm. Similar approaches in different types of vegetation cover showed, that band combinations from the red edge (Zhao et al. 2007, Mutanga & Skidmore 2004) as well as NIR and SWIR (Mutanga & Skidmore 2004, Xavier et al. 2006) had a close relationship to LAI and aboveground biomass and performed much better than spectral bands used in standard vegetation indices. This could be

confirmed by the much stronger positive increase in slope of the scatter plot for NRI than for the standard NDVI (Figure 4-9b).

Analogue to biomass, the regression analysis between NRI and plant nitrogen concentration resulted in a wide range of R^2 values. The best correlation was achieved by combining bands from the red edge region (702 to 732 nm) with wavebands centred between 1138 and 1332 nm, which is in accordance to findings of (Smith et al. 2003). In addition to this, several authors showed that the VIS region had a close relationship to plant nitrogen concentration (Daughtry et al. 2000, Nguyen & Lee 2006). It is well known that canopy spectral reflectance of the VIS (400 to 700 nm) is mainly governed by foliar pigments such as chlorophyll which is induced by plant nitrogen concentration (Kumar et al. 2003, Oppelt & Mauser 2004). In addition to the VIS region some authors proved a sensitivity of red edge (Strachan et al. 2002) as well as NIR (Hansen & Schjoerring 2003) for nitrogen status detection, which is coincident with the best wavebands used for NRI index calculation in our study. Furthermore, the study of Ferwerda et al. (2005) indicated significant differences in the estimation potential of indices for nitrogen concentration across different species.

The inter-year validity of the Hyperion model was proven by applying the model established in 2008 to the acquisitions of 2009 (see Figure 4-8). In addition to the temporal validity on regional scale, Gnyp et al. (submitted) applied the NRI model to different scales. Experimental set-up included small experimental fields (ca. 4.5 m by 7.5 m), large experimental fields (ca. 10 m by 15 m), small farming fields (ca. 1500 m²) and large farming fields of around 1 to 4 ha. Results indicated, that NRI can explain about 73% to 89% of the biomass variability of winter wheat on different levels using hyperspectral spectroradiometer data. Compared to this, the best performing broad band indices (REP, OSAVI, TCI and NDVI) were able to explain only 37% to 52% of the biomass variability by using spectroradiometer data. Both experiments, which belong to the same project, demonstrate the advantage of hyperspectral narrow band indices (NRI) in terms of spatial and temporal validity.

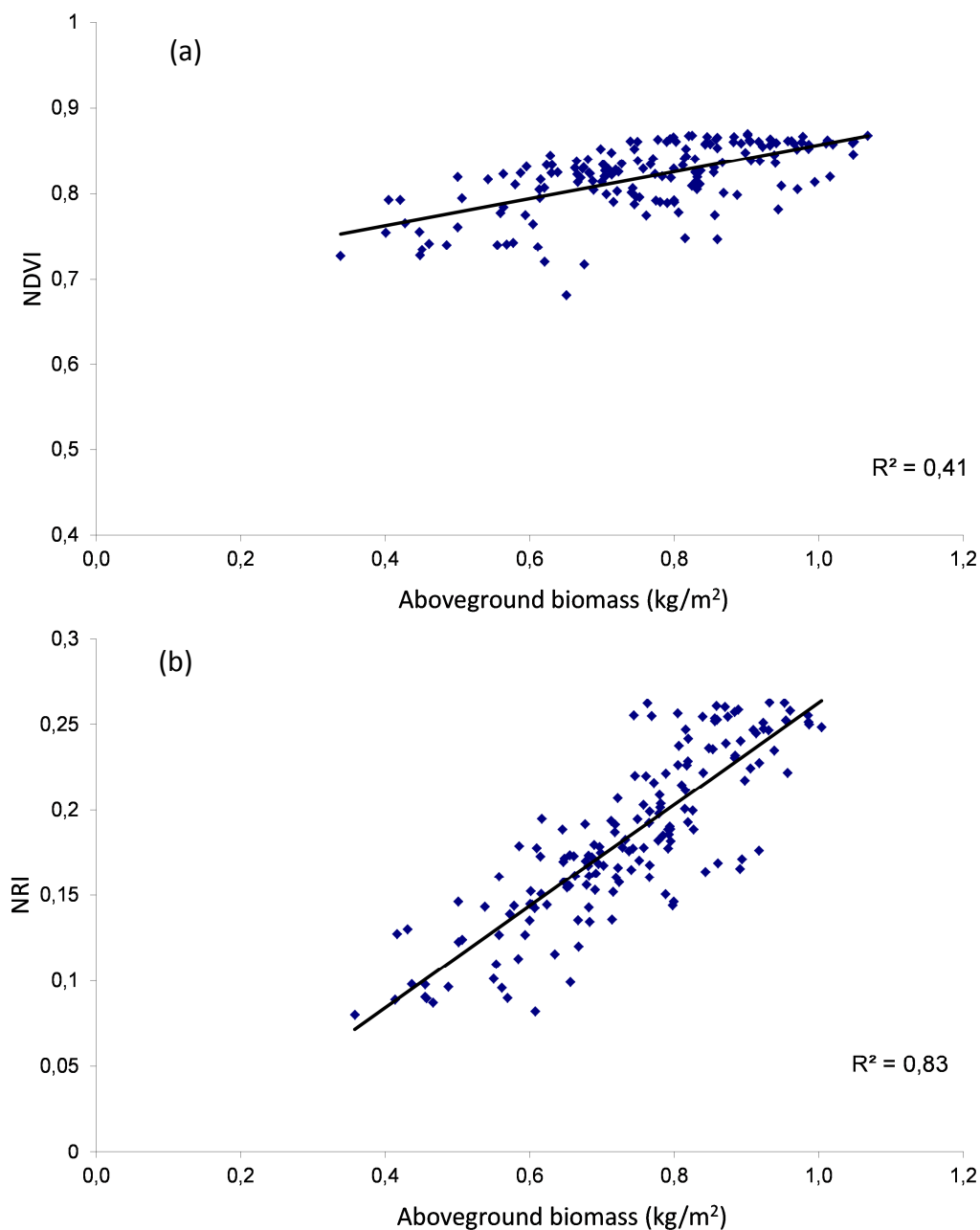


Figure 4-9: Scatterplot of (a) aboveground biomass against standard narrow band NDVI and (b) best waveband combination from NRI, 874 nm and 1225 nm (Koppe et al. 2010a).

4.3 Winter Wheat Monitoring with C-band*

4.3.1 Temporal Backscatter Behaviour of Winter Wheat

Averaged backscatter values of Envisat ASAR VV were extracted over crop fields in the test area. Figure 4-10 shows the temporal variation of winter wheat and the bare field backscattering coefficient σ^0 of ASAR VV expressed in decibel. In the box plot, the center horizontal line marks the median of the sample and the length of each box shows the range of the central 50% of the sample. In general, as the crop grows the number of leaves and the stem height increases, resulting in a corresponding increase in ground cover. This causes an increase in volume backscattering due to the increase of canopy constituents of wheat.

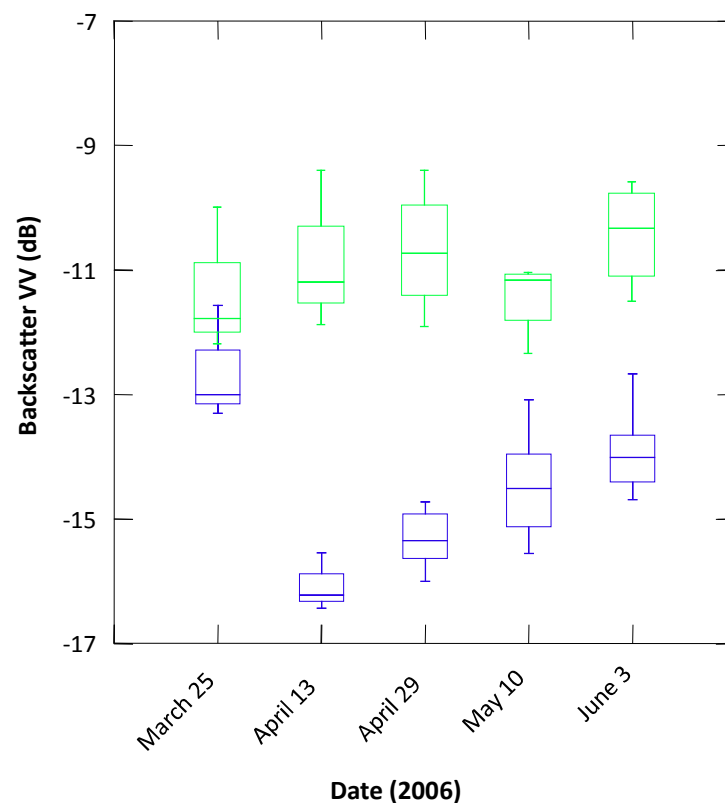


Figure 4-10: Temporal evolution for bare soil (green) and winter wheat (blue) of C-VV backscatter (Koppe et al. 2012).

* This section and sub-sections are an extended version of the article: Koppe et al. (2012).

At the beginning of the growing season in March, when stem height of wheat is about 9 to 13 cm, the VV backscatter of wheat fields is close to the backscatter from bare soil. The backscatter from ploughed fields is still higher, since soil surface roughness is higher than for the cultivated fields. Similar observations were described by McNairn et al. (2009) during the beginning of the growing season. At this growing stage, the backscatter is mainly driven by soil moisture and roughness parameters. When the crop is in the jointing stage on April 13 (stem height between 30 and 40 cm), the backscatter is significantly lower than at the tillering stage (decrease of about 4.5 dB), indicating a strong attenuation of the soil's backscatter by the wheat plants. As the wheat continued to grow through the stages jointing to ripening, the observed backscatter gradually increased by about 3 dB. This suggests a change in the dominant scattering mechanism from soil and roughness backscattering to canopy volume scattering, which is in coincidence with the findings of Mattia et al. (2003), who mentioned a change in scattering mechanism from soil to volume scattering for incidence angles greater than 40° of fully developed wheat. Also an Integral Equation Method (IEM) simulation carried out by Stiles et al. (2000) verified a lower sensitivity of higher incidence angles of VV polarization to soil properties.

In comparison to our observation of an increase in backscatter that begins at a stem height of 35 cm for VV polarization, Karjalainen et al. (2008) reported a gradual increase in backscatter for cross-polarization images that does not begin until a stem height of 50 cm is reached.

At the end of the growing season, the moisture content of plants decreases, while the contribution of soil and surface roughness upon the SAR backscatter increases. As the last Envisat data was acquired during the ripening stage of the plants, the increase in backscatter from mid of May (heading) to beginning of June (ripening) is also influenced by the soil component. Looking at the backscatter curve of bare fields, a similar increase as for the crop canopy is visible.

The results of field data and backscatter analysis show that the peak of volumetric moisture within the canopy (jointing stage) did not necessarily coincide with the peak in backscatter (see Table 4-1 and Figure 4-10). Besides volume scattering, the interactions between ground and stem for fully developed wheat seem to have an

important contribution to the cumulative backscatter value, as also mentioned by Picard et al. (2003).

Considering the whole vegetation period, the range of backscatter of about 3 dB is lower than measured by Karjalainen et al. (2008), but comprehensible if findings by McNairn et al. (2004) are taken into account. They detected a higher sensitivity of HV polarization to crop condition than for VV polarization.

During the growing season, the volumetric soil moisture was relatively constant (between 15% and 30%), thus the change in backscatter of about 3 dB on average of the test parcels was most likely caused by the accumulation of aboveground biomass. Despite the usage of different orbits with slightly different local incidence angles, a dependence of the backscattered signal on incidence angle could not be observed. A strong impact on radar backscatter based on incidence angle differences of about 5-6° was reported by Ban & Howarth (1998).

4.3.2 Relating Crop Condition to Envisat ASAR

The use of microwave data for crop monitoring is particularly attractive because of its weather and daylight independence on the one hand and its interaction with canopy structure as well as dielectric properties on the other hand. The sensitivity of Envisat ASAR signals was analysed as a function of wheat field characteristics. Based on the averaged backscatter values per parcel and the corresponding measured biomass (dry matter) values, a linear regression equation was derived. The bivariate correlation based on linear regression between SAR backscatter and standing biomass resulted in $R^2 = 0.75$ (Figure 4-11). The equation of the regression is:

$$BIOM_{2006} = 1.36(VV_{2006}) - 16.3 \quad (4.3)$$

The coefficient of determination suggests that Envisat ASAR multi-temporal imagery is sensitive to crop condition during the growing season of winter wheat. The statistical values are given in Table 4-6.

Table 4-6: Coefficient of determination (R^2) between biomass and Envisat ASAR backscatter (Koppe et al. 2012).

Year	Input data typ	Input acquisitions (date)	n*	Correlation coefficients (R^2)	RMSE (kg/m^2)	RE (%)
2006	SAR	Apr 13, Apr 29, May 10, June 3	23	0.75	0.24	25.5

* number of samples

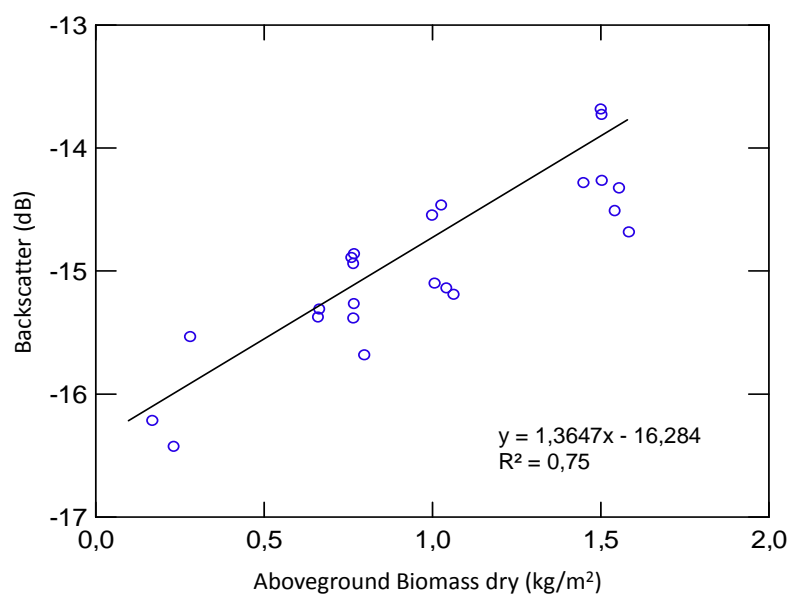


Figure 4-11: C-VV backscatter related to aboveground biomass (Koppe et al. 2012).

4.3.3 Discussion of C-band SAR Data for Wheat Monitoring

In an agricultural environment, the monitoring and prediction of biomass and grain yield is one of the most important objectives. Multi-temporal Envisat ASAR VV data at an incidence angle range from 39° to 42° were analysed as a function of wheat phenological stage. The results show a significant sensitivity to canopy developing stage and a general increasing trend in backscattering with winter wheat growth. During the vegetation period, soil moisture remained relatively constant (at least from one acquisition to another), consequently changes in backscatter are due to crop growth and less influenced by varying soil moisture. Figure 4-11 show that biomass is significantly positively correlated with C-VV backscatter over the growing season with a dynamic range of around 3 dB. For the relationship of C-VV backscatter to biomass, Mattia et al. (2003) also found an increase in backscatter following the increase in biomass, but only until the heading stage. After the heading stage, backscatter again

decreases which was explained by a change in canopy geometry during heading and booting stage (McNairn et al. 2004). At the same phenological stages, Liu et al. (2006) reported a negative correlation of backscatter with biomass and explained this phenomenon also with changes in crop canopy. However, observations of Karjalainen et al. (2008) also show a congenerous increase of backscatter with an accumulation of wheat biomass until the heading stage as was observed in this study. Beside the positive multi-temporal relationship between biomass and VV backscatter, it is also obviously that in this case microwave is not suitable for prediction of biomass at a given date (mono-temporal). This may be due to fewer sub-plots which reduce the random sample and dynamic biomass range.

Furthermore, it is worth mentioning, that there are unsolved problems limiting the value of the results achieved by Envisat ASAR data. First, the resolution of Envisat ASAR is very low compared to the field size, thus only large fields can be included in the analysis. Secondly, the analysis was performed with a small number of fields in a relatively homogenous agricultural environment. Within-field and inter-field variation of crop parameters at a specific acquisition date was too low.

4.4 Synergy of Hyperspectral and C-band SAR Data for Crop Parameter Estimation*

For a combined approach, the acquired hyperspectral and microwave data were used for modelling of biomass. This was done by considering only image pairs from EO-1 Hyperion and Envisat ASAR that were acquired within one week to ensure similar biophysical parameters of the fields in both images of the pairs. The correlation is based on a linear regression of wheat crop parameters against ASAR VV backscatter and NRI calculated from satellite data in 2006. For NRI, the best combination of wavebands (874 nm and 1225 nm) determined in chapter 4.2.2.3 and for ASAR backscatter, the calibrated values to sigma nought were used. The combined modelling of NRI and SAR backscatter was according to the following linear regression:

$$BIOM_{(Hyp / ASAR)} = a(NRI) + b(VV) + c \quad (4.4)$$

* This section is an extended version of the article: Koppe et al. (2012)

where $BIOM_{(Hyp/ASAR)}$ is the combined biomass estimate from optical and SAR image analyses, NRI is the normalized ratio index derived from equation 3.4, VV is the ASAR C-VV backscatter and a , b and c are constant parameters of the model.

In terms of bivariate analysis, best results for regression were achieved with narrow band vegetation indices derived from EO-Hyperion data ($R^2 = 0.83$). Lower coefficients of determination were achieved by using Envisat ASAR backscatter for relating with crop parameters for the 2006 SAR campaign ($R^2 = 0.75$). If the models derived from combined SAR and hyperspectral data based on multiplication, the biomass prediction could be improved to $R^2 = 0.90$ (RMSE 0.81 kg/m²). The applied equation is:

$$BIOM_{(Hyp / ASAR)} = 2.73(NRI) + 0.16(VV) + 2.68 \quad (4.5)$$

The statistical results for biomass retrieval of the combined model are listed in Table 4-7. The results show that crop parameters can be predicted by remotely sensed data from the different acquisition systems. Similar close relationships between crop parameters and satellite data has already been established by Thenkabail et al. (2004) and Xavier et al. (2006) for hyperspectral data and furthermore by Baghdadi et al. (2010) and McNairn et al. (2004) for SAR data.

Table 4-7: Coefficient of determination (R^2) between biomass and Envisat ASAR backscatter (Koppe et al. 2012).

Year	Input data typ	Input acquisitions (date)	n*	Correlation coefficients (R^2)	RMSE (kg/m ²)	RE (%)
2006	hyperspectral / SAR	April 19, May 6/ April 13, May 10	25	0.9	0.81	12.2

* number of samples

Beside the multivariate analysis based on multiplication, there are other types of combination that were not addressed. In this study, the multivariate analysis should only demonstrate the improvement of prediction power based on multiple data sources. Similar improvements for yield prediction were achieved by combining time series from SAR and optical data (Liu et al. 2006).

To achieve high prediction accuracy of wheat's crop parameters based on a single source (ASAR or Hyperion) and combined analysis of SAR and optical data, it is important to select suitable dates for satellite data acquisition. Based on the satellite multi-temporal and multisource data analysis as well as on analysis of field spectrometer data (Li et al. 2008), certain acquisition periods of SAR and hyperspectral data for winter wheat in the North China Plain seem to be convenient. For the acquisition of Hyperion data, the optimized acquisition window is from the beginning of April after tillering to the heading stage before saturation effect of reflectance occurs and flowering begins. In comparison to multispectral imagery, hyperspectral data can improve the performance early and late in the season (Xavier et al. 2006), which enlarges the acquisition window (Strachan et al. 2002). The use of hyperspectral narrow band vegetation indices can reduce saturation effects at the end of the growing season, which was confirmed for winter wheat by Koppe et al. (2010a). For SAR data, observations suggest that a relationship between backscatter and crop parameters can be established between jointing and heading/flowering. Almost similar optimal temporal range from tillering to heading stage for crop parameter estimation is reported by Mattia et al. (2003) and Picard et al. (2003).

4.5 Polarimetric Rice Monitoring with X-band

The polarimetric parameters for rice crop monitoring are described and discussed based on the image series of 26°. For completeness, in Appendix A.4 polarimetric parameters for 26° and 46° for rice and non-rice areas are comparatively depicted.

4.5.1 Power: Backscattering Signature and Ratio

The acquisition period of TerraSAR-X starts one month after transplanting, contemporaneously with the field campaign. Because of this, no acquisition at the early stages after transplanting the seedlings is available. The backscatter signatures of HH and VV co-polarization have a unique pattern that depends on the growth stage of the plants. Figure 4-12 and Figure 4-13 illustrate the temporal evolution of the backscattering coefficient sigma nought (σ^0) of the rice fields at the X-band as a function of number of days after transplanting at HH and VV polarization. For each

acquisition, the backscatter values of TerraSAR-X were extracted over paddy rice fields and averaged at plot level.

4.5.1.1 Incidence Angle Differences

For comparison, the backscatter signatures of the different incidence angles are shown in Figure 4-12. The figure (a) shows a steep incidence angle of 26° acquired in ascending mode, figure (b) depicts a medium incidence angle of 36° (descending) for SM and 39° (ascending) for HS and figure (c) shallow incidence angle of 46° (ascending).

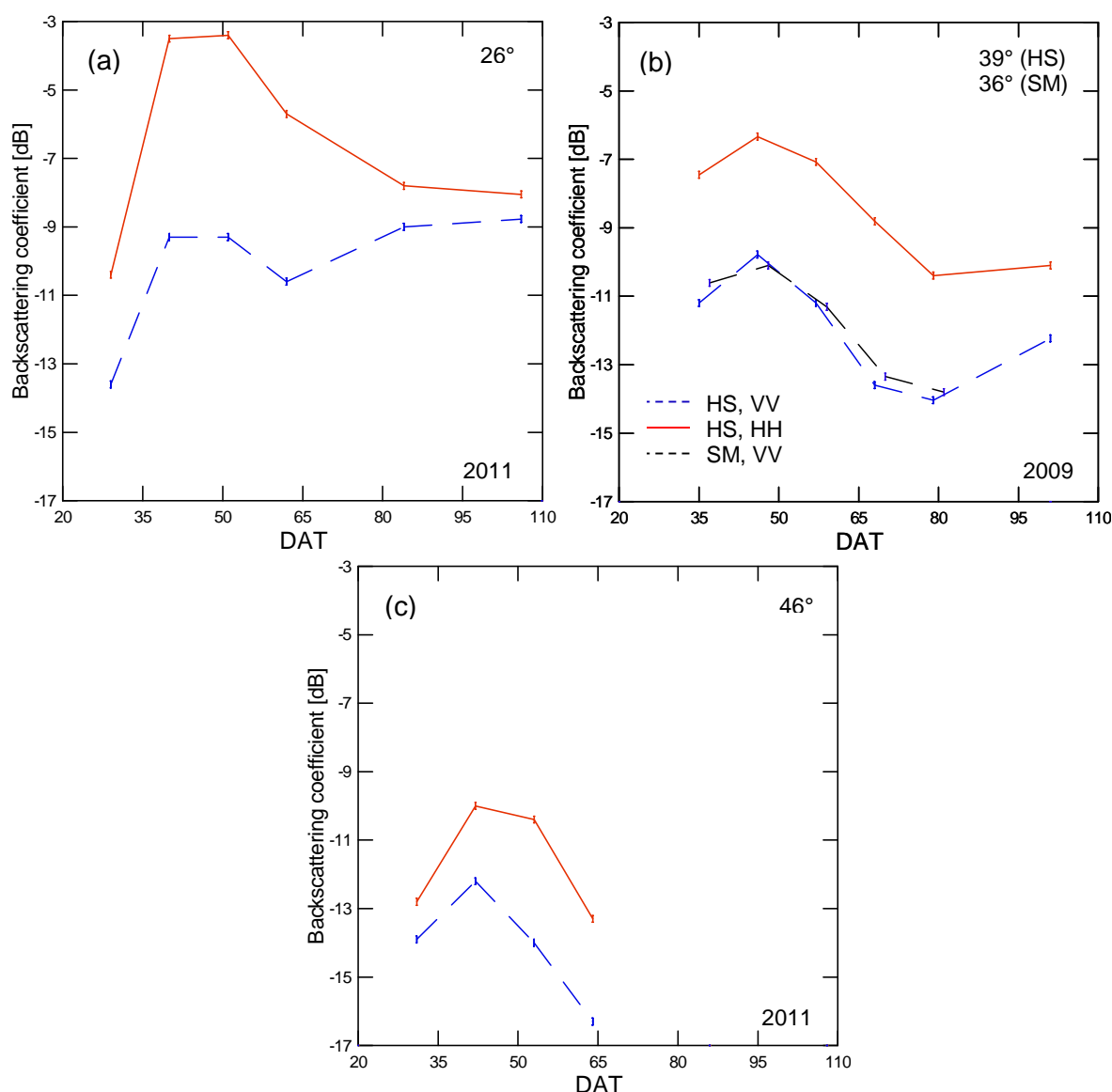


Figure 4-12: Mean temporal backscattering coefficient (sigma nought) for different incidence angles of VV and HH of rice during the vegetation periods in 2009 and 2011. (a) SL, 26° . (b) HS, 39° and SM, 36° . (c) SL, 46° .

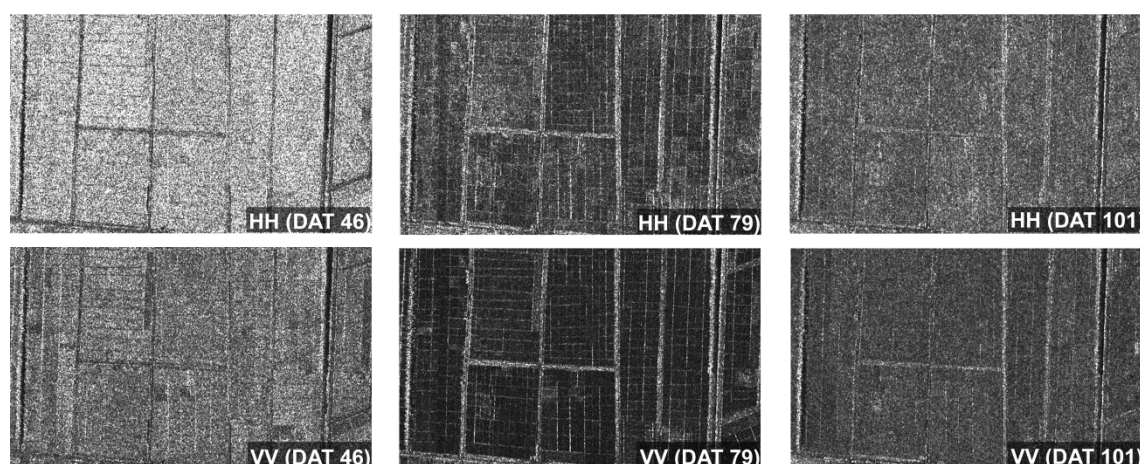


Figure 4-13: TerraSAR-X Spotlight images at HH (top), VV (down) at three acquisition dates in 2009 (modified after Koppe et al. 2013).

The steep incidence angle shows a high dynamic range for both polarization (7.5 dB for HH and 5 dB for VV) compared to 3 dB for HH and 4 dB for VV at shallow incidence angle. A higher dynamic range enables a better differentiation of growth status or growth problems of different parcels.

4.5.1.2 Typical Backscattering Signature*

To ease subsequent general description of backscattering signature of rice, detailed characterization is based on the 2009 acquisitions (39°). In general, the backscattering from the paddy rice field before transplantation is close to the noise level (between 18 and 21 dB) for both polarizations. Due to the flooded fields, the incident waves are scattered specularly away from the sensor. After transplantation, the backscattering coefficient of HH and VV increases up to DAT 46 with a successive decrease until DAT 80 (heading stage). From DAT 80 (heading stage) to the last acquisition, a second increase in σ^0 can be observed. For all acquisitions, the backscattering coefficient of HH is higher than for VV. Through the whole vegetation period, the HH polarization provides a higher backscatter than the VV channel. From the first to the second acquisition, a significant increase in σ^0 for both polarizations can be observed. The age of the rice plants at the maximum backscattering coefficient is between DAT 40 to 50 and the height is around 55 cm. Although height and the biomass of the plants increases further after DAT 50 (Table 4-2), the backscatter of both polarizations decreases until DAT 80, whereas the slope of both polarizations is almost the same.

* This section is an extended version of the articles: Koppe et al. (2011); Koppe et al. (2013).

The backscatter from the fields is lowest at around DAT 70 to 80 for VV and HH. The paddy fields are very dark and the dams separating the parcels are clearly visible due to double bounce scattering from the water – dam interaction (see the two central TerraSAR-X images in Figure 4-13 compared to the left ones). With the beginning of the ripening stage (later than DAT 80), the increase in biomass of stems and leaves stopped and the plants get drier. Also the orientation of the leaves changed from mostly vertical to a random distribution. Coinciding with these changes in the canopy of the rice fields, the decrease in backscatter of both polarizations stopped. At the last acquisition, a slight increase in backscatter can be observed. This increase is more obvious at VV polarization than at HH.

4.5.1.3 Co-pol Ratio (HH/VV)

Additionally to the investigation of the backscattering power of HH and VV, also the ratio of the power (HH/VV) was analysed as a function of days after transplantation. Figure 4-14 shows the evolution of co-polar ratio from tillering to ripening stage at 26° incidence angle. The ratio increases from the first acquisition at tillering to booting stage to more than 5 dB, whereas the largest difference between minimum and maximum is around 4 dB. The increase of the ratio is coincident with increasing backscatter of HH and VV, whereas the maximum of the ratio is reached later at the booting stage. The strong increase of the ratio is attributable to the presence of double bounce reflection and the greater VV extinction due to the vertical orientation of the rice plants. After this, the ratio decreases down to a value range between 2 to 3 dB at the beginning of the ripening stage. At the last acquisition the value range stays constant and there are no significant changes.

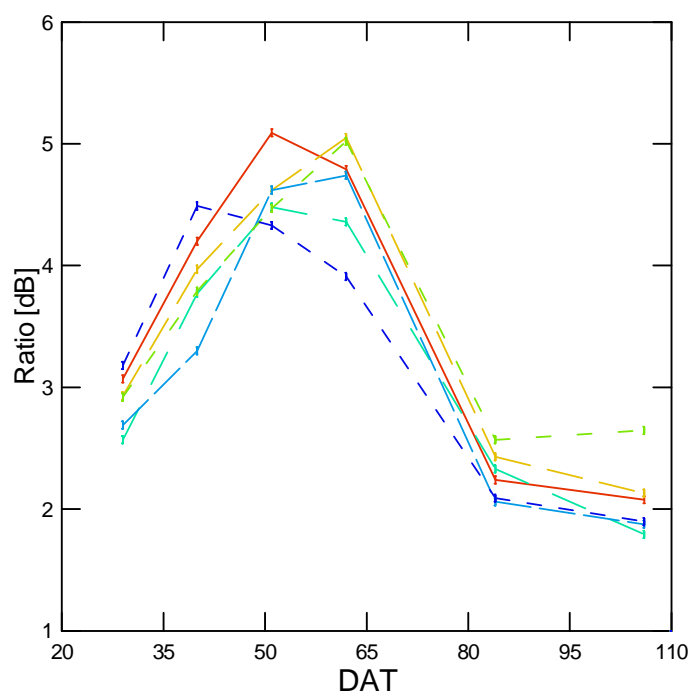


Figure 4-14: HH/VV ratio of six rice parcels as a function of time at 26° incidence angle.

4.5.2 Correlation: Polarimetric Coherence and Phase Difference

Correlation between the co-polar channels HH and VV is shown in Figure 4-15. Unfortunately, there is no acquisition at the flooded stage and the early beginning of the vegetative stage. During the flooded stage surface scattering is the dominant scattering mechanism of rice fields. This specular reflection, which occurs also at open water surfaces in the study area at any time, is characterized by a high polarimetric coherence between HH and VV. Coherence values of water surfaces are above 0.7, depending on the roughness of the water surface. From the flooded stage the coherence drops down and remains constant within the value range between 0.3 and 0.5 with no significant variation due to changing phonological stage. Low coherence between the co-polar channels is caused by the strong attenuation of the VV backscatter compared to HH backscatter (differential extinction) (Lopez-Sanchez et al. 2011).

The co-polar phase difference of HH and VV is also shown in Figure 4-15. For a flooded surface, the phase difference is close to zero due to dominating specular reflection which is associated with no time delay between the HH and VV phase (evaluated on open water surfaces in the study area). From tillering on, the phase difference drops

continuously to its minimum of around -30 degrees. Differential extinction causes a phase delay and hence a phase difference other than zero. Interpreting this behaviour, it can be stated that double bounce scattering is dominating and the contribution of surface scattering is reduced. After booting stage the phase difference values increase and approach zero value finally. Increasing trend in phase difference is coincident with decreasing backscatter; both can be attributed to random volume scattering that dominates over double bounce because of the increasing leaf coverage.

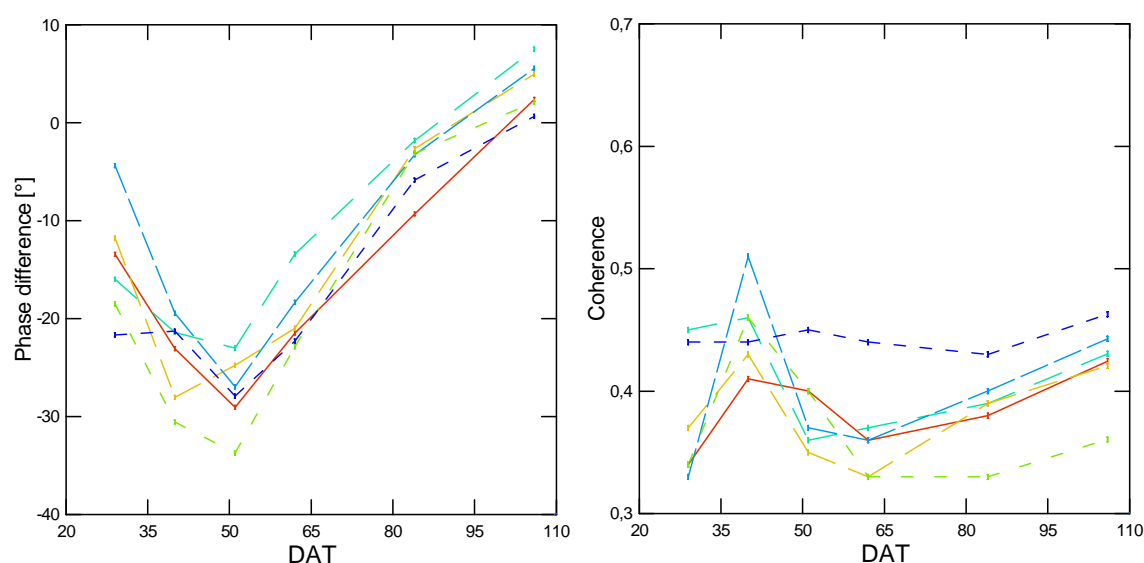


Figure 4-15: Co-polar phase difference and coherence of six rice parcels as a function of time at 26° incidence.

4.5.3 Polarimetric Decomposition: Alpha and Entropy

Based on the eigenvector decomposition, alpha and entropy are calculated according to chapter 3.2.3.4. Evolution of alpha and entropy is shown in Figure 4-16 as a function of time. The signatures of entropy and alpha show a similar behaviour during the vegetation period. They decrease from tillering to booting stage. After the depth point at booting stage, entropy and alpha value increase to ripening. Entropy values for open water surfaces (flooded stage, not covered by an acquisition) are generally low, since there is only one scattering mechanism from the water surface (surface scattering). Also alpha angle is very low (close to zero), which is typical for surface scattering.

With emerge of the plants, entropy jumps above 0.8 and decreases subsequently with further plant development. The high entropy at tillering indicates that more than one

scattering mechanism contributes to total backscatter. The identified scattering mechanisms are surface and double bounce scattering from the surface-stem interaction. The alpha angle of around 45° indicates a dipole-like scattering at tillering, whereas with the presence of strong double bounce scattering one could expect a higher alpha value. Minimum values of entropy (0.55) and alpha (20°) are reached at booting stage. With the beginning of the reproductive stage the Entropy increases again until flowering as a consequence of random volume scattering. From flowering it remains constant to ripening.

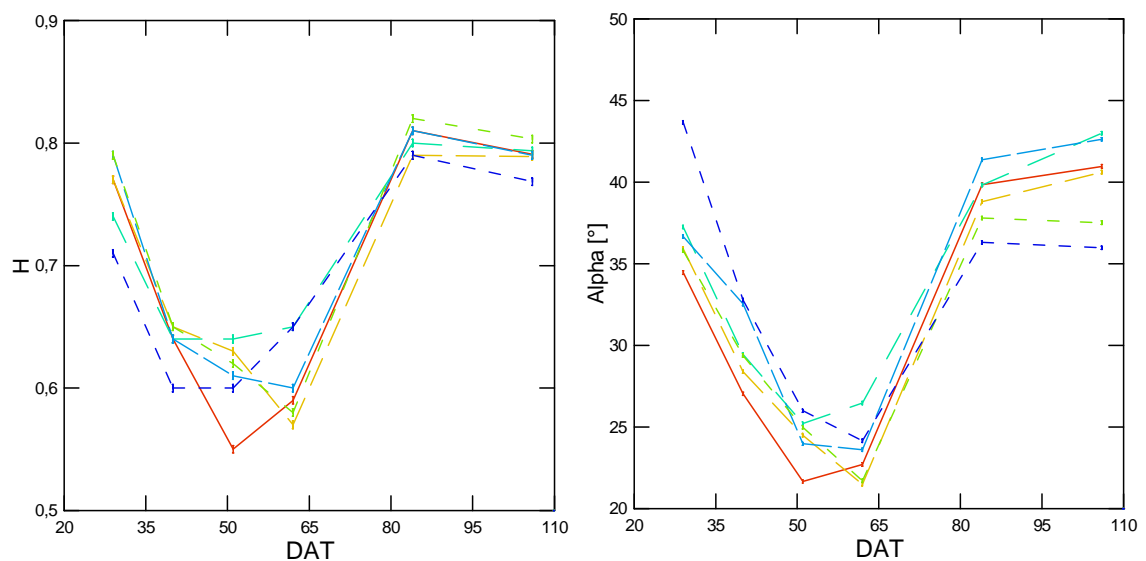


Figure 4-16: Co-polar eigenvector decomposition (alpha and entropy) of six rice parcels at 26° incidence.

4.5.4 Correlation Analysis between Backscattering Coefficients and Plant Variables*

To better understand backscattering of X-band microwaves, we conducted a correlation analysis between TerraSAR-X derived σ^0 (2009 data) and accumulated biomass. As already mentioned, microwave backscatter is not only dependent on one parameter, but rather a function of various parameters from soil and vegetation. In the case of paddy rice fields, we can simply assume that backscatter from the background (flooded surface) is constant. To investigate the different scattering layers inside the vegetation canopy, the plants were separated into the main parts (stem, leaf, and head), which is important for interaction with microwave radiation. Since backscatter

* This section is an extended version of the article: Koppe et al. (2011); Koppe et al. (2013).

return is related to the physical parameters of the plant such as its orientation, dielectric constant and the number of scattering elements, a correlation should be meaningful between the backscatter and different plant elements (biomass of stem, leaf, and head). The regression analysis is established for single dates to observe the trend in degree of correlation from date to date for the different scattering layers, instead of a pooled data set with all dates. For this study, the degree of correlation between backscatter and the different vegetation layers (stem, leaf and head) at a certain growth stage is important to understand the interaction between microwave backscatter and rice phenology. Table 4-8 shows the correlation coefficients for biomass of the whole plant as well as for the separated layers stem, leaf, and head. The correlation coefficients were calculated for VV and HH backscatter of HS data and for the single polarization VV backscatter of SM data.

For the first date, a significant correlation was found between HS data and the stem, whereas the correlation with the leaves is only slightly lower (for VV). For SM data, the correlation coefficients for all crop parameters are significantly lower. The lower correlation coefficients of SM data as compared to HS data could also have been influenced by heavy rain events before and during the SM acquisition. For the second acquisition, the correlation between backscatter and stem reduced for VV (HS) and remained relatively constant for HH polarization while correlation coefficients of both polarisations increased significantly for leaves. At 79 DAT, the stem contribution to total backscatter reached its minimum. The correlation coefficients of both polarizations are around 0.2 for HS data and 0.05 for SM data respectively. In comparison, the leaves show considerable correlation with backscatter values. At this stage, the crop heads are already fully emerged and show a correlation coefficient similar to the leaves. During the growing season, total biomass was most highly correlated with VV and HH backscatter DAT 46 (see Table 4-8).

Table 4-8: Correlation coefficients (R^2) between backscatter (HH and VV) and plant variables, including total biomass of the whole plant and the components stem, leaf and head for HS and SM (modified after Koppe et al. 2013).

		DAT 35 (37)			DAT 46 (48)			DAT 79 (81)		
		HS		SM	HS		SM	HS		SM
		VV	HH	VV	VV	HH	VV	VV	HH	VV
Stem	R^2	0.69	0.61	0.27	0.51	0.60	0.41	0.19	0.24	0.05
	RMSE (t/ha)	0.16	0.19	0.28	0.37	0.28	0.42	2.7	1.88	3.1
	RE [%]	18.9	20.7	38.5	21.7	16.6	25.7	55.6	38.9	85.5
Leaf	R^2	0.67	0.56	0.25	0.72	0.83	0.59	0.68	0.74	0.60
	RMSE (t/ha)	0.16	0.20	0.30	0.20	0.17	0.32	0.33	0.28	0.37
	RE [%]	19.5	24.5	34.5	16.5	12.5	22.8	21.2	17.8	26.3
Head	R^2	-	-	-	-	-	-	0.64	0.51	0.60
	RMSE (t/ha)	-	-	-	-	-	-	0.22	0.26	0.23
	RE [%]	-	-	-	-	-	-	17.8	20.5	19.8
Total biomass	R^2	0.61	0.58	0.27	0.64	0.80	0.51	0.37	0.35	0.31
	RMSE (t/ha)	0.42	0.49	0.60	0.44	0.32	0.56	2.44	2.56	2.95
	RE [%]	24.6	27.5	37.5	16.6	10.0	24.3	31.5	32.2	37.3

4.5.5 Polarimetric Growth Stage Monitoring

Based on the polarimetric analysis presented in this chapter, the polarimetric parameters are now evaluated for crop status monitoring. To cover most parts of the vegetation period at the vegetative phase but also at ripening, the time series of 26° of incidence is chosen for demonstration. For interpretation purpose, each acquisition is assigned to a dedicated phenological stage. The temporal distance between two acquisitions is at least 11 days (satellite repeat pass); this is why an acquisition date may not fit best to a certain phenological stage. Hence the acquisition of image data could have taken place in the transition zone between two phenological stages which has an influence on the values of the measured parameters.

For prediction of crop growth stage from remotely sensed data, the ideal operational case would be based on a single acquisition. To rely on a single acquisition there should be a parameter defining crop status univocal. Looking at the different polarimetric parameters, most of them are equivocal in relation to phenological stage and not suitable for crop status prediction based on a single parameter. For example, a co-polar ratio of 3 dB could be assigned to tillering but also to heading. To overcome ambivalence of a single parameter, Lopez-Sanchez et al. (2011) suggested to combine parameters since the parameter combination provides an univocal definition of phenological stage. For the recent study, the parameters ratio, polarimetric coherence, polarimetric phase difference, entropy and alpha are combined to define a unique signature of phenological stage. Polarimetric coherence based on the magnitude of HH and VV is high (> 0.8) for open water surfaces. This is why it could be used as an indicator of flooded fields at the beginning of the vegetation period. For the remaining vegetation period, polarimetric coherence shows no significant variation and is therefore not suitable as classification parameter in this case. Backscatter of HH and VV is summarized as Power since HH and VV signatures run parallel. Power values have informative character. For classification only the mentioned parameters are recommended since they can be put into distinct intervals for classification. As a simplification for the recent study, all parameters are classified into three classes: low, medium and high. The assigned growth stages are: flooded (as no acquisition was done at flooding, the information was extracted from water surfaces at the first acquisition),

tillering, stem elongation, heading and ripening. For explanation, there is certain statistical variability in the different parameters due to the heterogeneity of the studied parcels and the processing of the satellite data. To generalize classification scheme, 20 parcels were averaged for each parameter at each growth stage. Figure 4-17 shows the combination of the different parameters for the five defined growth stages. The respective parameters are relatively classified in low, medium and high values.

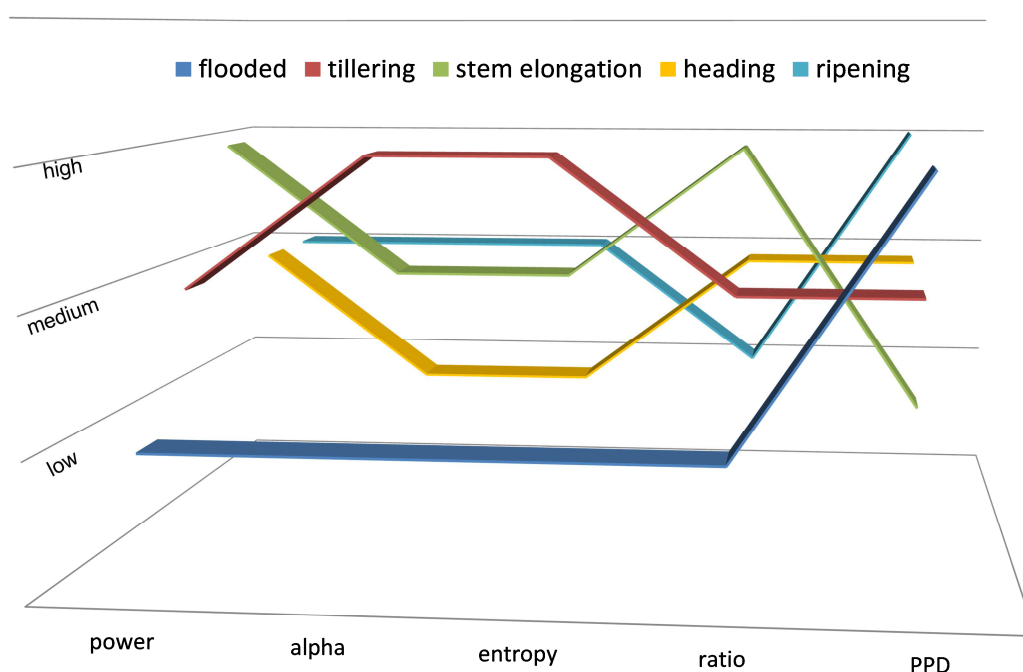


Figure 4-17: Relating phenological stage of rice to polarimetric parameters.

The flooded stage can be described with low power, alpha, entropy, ratio and high PPD since surface scattering induces a clear response of the mentioned parameters. Also the power of HH and VV is close to the noise level, whereas power at this stage can be very variable depending on the roughness of the water surface. Especially for steep incidence angles, the return can be very high from a rough water surface. Tillering identification is mainly based on eigenvector decomposition parameters, namely alpha and entropy. Both of them are very high, due to the presence of more than one scattering mechanism and double bounce return from the water-stem interaction. Additionally to these parameters, ratio is increasing with increasing differential extinction of co-polar channels and PPD is decreasing. Both of them were classified to medium value range. With the transition to the next growth stage, power increased to

maximum value and also ratio is close to its maximum. In relation to this, eigenvector decomposition parameters decreased to medium level and PPD reached its low mark. In the heading or reproductive stage, alpha and entropy drift to low values whereas PPD is increasing to medium level as a result of dominating random volume scattering. Last growth stage covered by an acquisition is characterized by high PPD, which increased from medium to its maximum from heading to ripening. Ratio is decreased to low mark since backscatter of HH and VV approach each other. The knowledge about the phenological development of rice and its expression in polarimetric parameters is valuable in terms of land cover classification (Appendix A.3) and growth stage monitoring.

4.5.6 Discussion of Polarimetric Rice Monitoring*

The backscattering behaviour of spaceborne X-band data as described above shows similarities with ground-mounted scatterometer data observed by Inoue et al. (2002) and Kim et al. (2000). Both studies mention a notably higher backscatter of HH compared to VV polarization during the growing season. This phenomenon can be explained by stronger attenuation of the vertical cylinders (stem and leaves) of the VV polarization case (Le Toan et al. 1989). The observed trend lines for HH and VV backscatter can be separated into three main parts: increasing trend up to 46 DAT, decreasing trend up to DAT 80 and an increasing trend again to the last acquisition. This dual-peak trend is incidence angle dependent; Kim et al. (2008) reported a clearer development of the two peaks for shallow incidence angles. The three main stages of the trend line are discussed consecutively.

Before transplantation, the paddy rice fields are flooded and the backscatter in either HH or VV is very low close to the noise (noise level -19dB for TerraSAR-X and TanDEM-X). Backscattered energy is depending on roughness of the surface, for a calm surface backscatter is lower than for a rough one. In the case of a calm surface, the water surface acts as a reflector for the incident radar wave (see Figure 4-19a). The increase in backscatter up to DAT 46 can be attributed to the fact that the main backscattering is contributed by the interaction between the stem and the underlying water surface

* This section is an extended version of the article: Koppe et al. (2011); Koppe et al. (2013).

(double bounce). Based on recorded power and calculated entropy values at the early vegetative stage, there are at least two types of backscattering namely the double bounce and the specular reflection from the water surface. A generalized ray tracing is depicted in Figure 4-19b. During the first growth stages, the plant structure remains mostly erectophile, i.e. the stems remain predominantly vertical and the leaves of the plant show a small insertion angle of around 5 to 25°. At this stage, the backscattering coefficient can be related to the amount and to the density (biomass) of the stems and leaves (see Table 4-8). The relationship is stronger at VV than at HH polarization. Considering backscattering behaviour and regression analysis, it can be stated that the higher the density of the vertical elements, the higher the double bounce return from the stem-surface interaction. Due to this double bounce scattering, σ^0 increases with increasing plant density and with plant growth as mentioned before. The first peak in backscattering coefficient is reached at a plant height of around 50 cm (DAT 46) and a total biomass of around 2.7 t/ha. Compared to the final height of up to 100 cm and a final biomass of 14 t/ha at harvest, the multi-temporal relationship with biomass gets lost in the early growing season. Using the same frequency, the increasing trend and hence the multi-temporal relationship can be maintained up to DAT 70 (plant height ca. 70 cm) (Inoue et al. 2002) by using a steep incidence angle of 25° or up to DAT 55 (60 cm) (Kim et al. 2000) by using an incidence angle of 10°. For steeper incidence angles, the peak in backscatter is reached later due to a shorter propagation path and lesser attenuation through the foliage (Woodhouse 2006). However, both studies are based on ground-mounted scatterometer measurements; an incidence angle of 10° is not feasible for spaceborne systems. Comparing the incidence angle differences in the present study, the previous statement by Woodhouse (2006) can be partially confirmed. For the steep incidence angle the increasing trend lasts not necessarily longer than for 46°, but for 26° there is at least a plateau (for HH a minor increase) at the peak backscatter. Compared to this, the shallow incidence angle is decreasing rapidly after reaching the peak (see Figure 4-12).

A longer-lasting increase in backscatter with crop age was reported for C-band data by Choudhury et al. (2007) and Chakroborty et al. (2005). In each case the maximum backscatter was reached at DAT 80 with a plant height of around 80 cm. L-band data

investigated by Ishitsuka et al. (2004) showed a later saturation level, but along with that also a very low sensitivity to changes in rice crop lower than 50 cm.

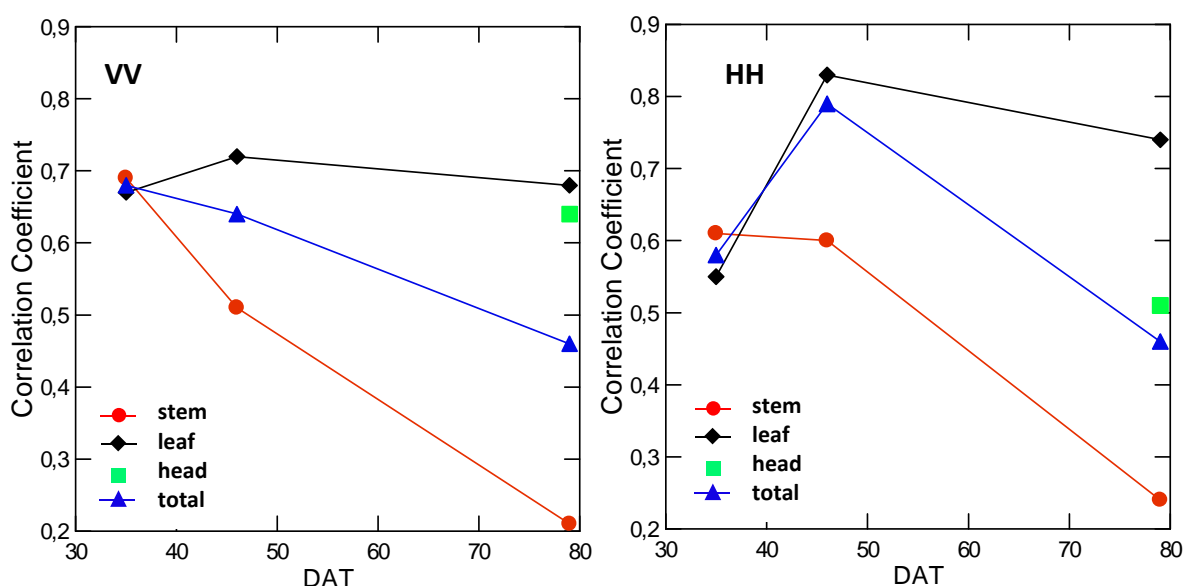


Figure 4-18: Correlation coefficients of TerraSAR-X HS backscatter (VV and HH) with stem, leaf, head and total biomass at DAT 35, 46 and 79 (Koppe et al. 2013).

After the peak in backscatter (DAT 46), the relationship with the stems ($R^2_{VV} = 0.51$ and $R^2_{HH} = 0.61$) in the recent study is lower than at the first acquisition. On the contrary, the correlation coefficients for leaves are higher than before ($R^2_{VV} = 0.72$ and $R^2_{HH} = 0.83$). This could indicate a combined contribution from the surface-stem double bounce scattering volume scattering from the upper part of the canopy (see Figure 4-18 and Figure 4-19c).

Although increases in height and biomass of the plants go on after the maximum backscatter is reached at DAT 46, a decreasing trend of both polarizations can be observed until DAT 80. This decrease in backscatter is due to increasing leaf density, which reduces the contribution from the surface-stem double bounce scattering by attenuation and random volume scattering as already indicated by correlation coefficients of DAT 46. This phenomenon agrees well with the backscattering signature for X-band reported by Kim et al. (2008) for paddy rice fields measured with a ground mounted polarimetric scatterometer. The decrease in backscatter stops at DAT 79 with a backscattering coefficient of around -10 dB for HH and -14 dB for VV. At this time, the contribution from the stems is almost blocked, the stems are poorly correlated with VV ($R^2 = 0.19$) and HH ($R^2 = 0.24$) whereas the upper canopy (leaves) is still

correlated with microwave backscatter ($R^2_{VV} = 0.68$ and $R^2_{HH} = 0.74$). After 70 DAT, the rice heads emerge as a new scattering element in the upper part of the canopy and show a dominant contribution to the backscatter signal (see Figure 4-19d). The relationship between microwave backscatter and rice heads results in a significant correlation ($R^2_{VV} = 0.64$ and $R^2_{HH} = 0.51$); this relationship was also reported by Inoue et al. (2002). It is rational to infer this as a function of X-band wavelength size, which is almost similar to the size of rice heads.

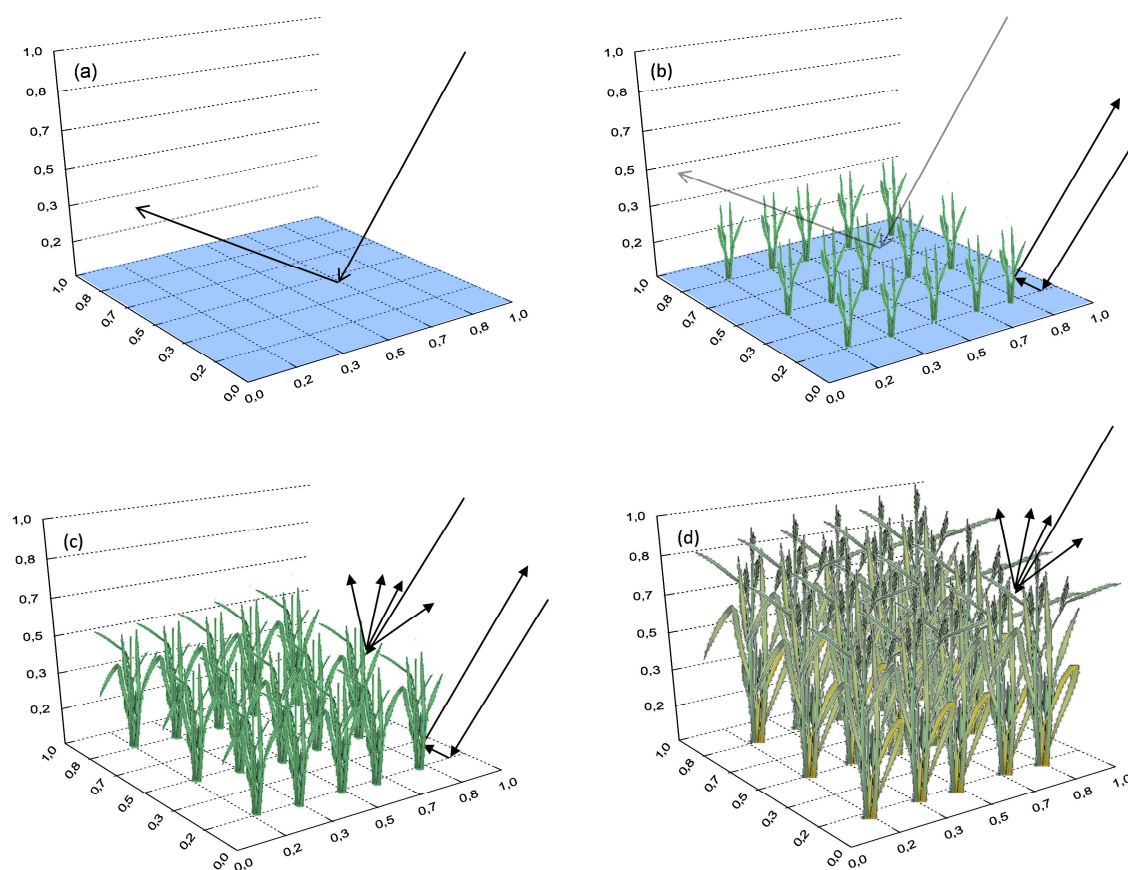


Figure 4-19: Backscatter behavior of rice at different growth stages. (a) Flooded rice field, DAT 0. (b) Early vegetative stage, DAT 35. (c) Late vegetative stage, DAT 46. (d) Reproductive stage, DAT 79.

After the decreasing trend, the backscattering increases slightly for HH polarization and around 2.5 dB for VV polarisation. Kim et al. (2000) explained the second increase in backscatter by the desiccation of the plants. At this growth stage, stems become drier and the reduced water content causes less vertical extinction, especially for VV polarization. In contrary, Inoue et al. (2002) reported a causal relationship between the previous emergences of the heads in the upper canopy and an increase in the backscatter. Both explanations could be also applicable for the observations in the

recent study. This increasing trend in backscatter is more obvious at larger incidence angles, because the penetration depth is lower than for steep incidence angles and the heads are thought to be the major scattering elements. Another reason for the increase in backscatter could be orientation of the elements. While they are mainly vertically orientated until the beginning of August, the orientation becomes random during the ripening period and induces more scattering in the upper canopy. Evidence for this could be that at the last acquisition (DAT 101), both polarizations approach each other (see Figure 4-12). The attenuation of the VV polarization by the vertical orientation of the cylinders is reduced. The backscatter coefficient of the rice cultivation is not polarization dependent as before.

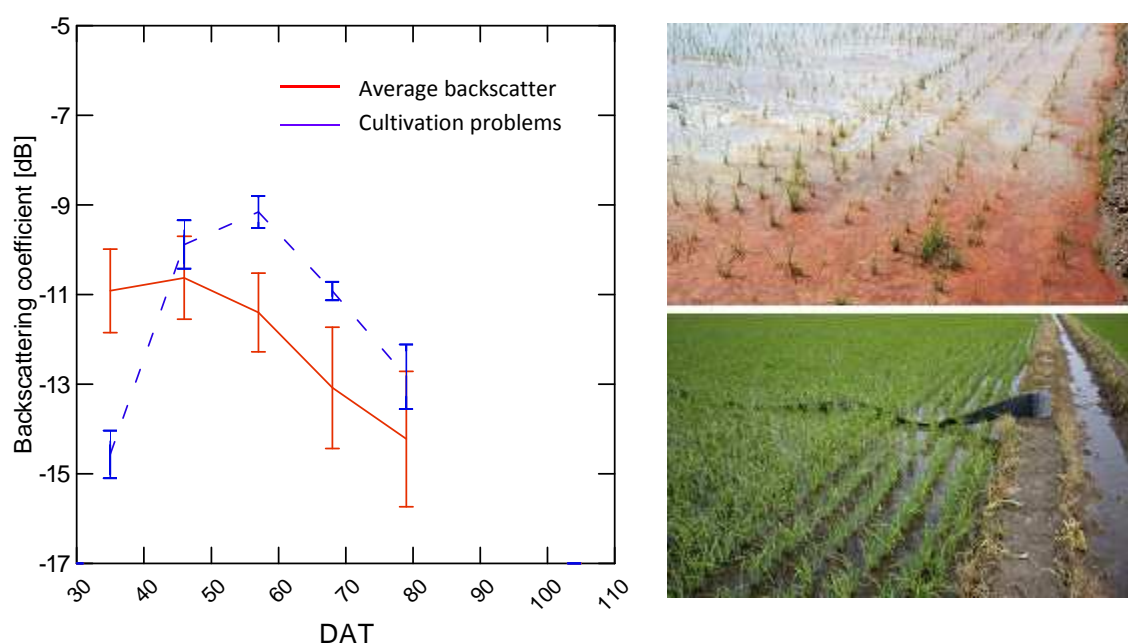


Figure 4-20: Left: Comparison of σ^0 signature between problematic fields (blue dashed line) and average of the normal growing fields (red solid line) based on SM VV backscatter. Upper right: Photo of a problematic field. Lower right: Photo of a normally growing field (Koppe et al. 2013).

During the vegetation period, growth problems due to cultivation practices were observed on two plots. These plots are outside the footprint of the HS data, so there is only a VV signature from SM available. In Figure 4-20, the blue line shows the course of signature of the problematic fields in comparison to mean signature of the other fields (red solid line). The backscatter signature of the affected plots is somehow shifted; the increase and decrease of backscatter are delayed of around 11 days due to the reduced plant growth rate. Also the maximum in backscatter is around 2 dB higher than the average of the other fields, which can be explained by a lower density of the

leaf layer. Both facts result in a longer validity of double bounce scattering and hence a later decrease in backscatter. Based on the multi-temporal backscatter analysis and the mono-temporal correlation analysis, it can be stated that the X-band backscatter is highly sensitive to changes in the canopy and the size of the dominant elements. This is confirmed by the course of correlation coefficients of VV and HH polarization with stem, leaf and head during the growing season (see Figure 4-18). At the first acquisition, the relationship is valid for stems and leaves; double bounce from the surface and vertical elements is the main scattering behaviour.

But with the development of the plants and hence with increasing leaf density, the correlation coefficients are lower for stems and increase for the leaf layer. At the last acquisition date, correlation with stems is poor, whereas there is still a correlation with the leaf layer and also with the recently emerged heads (at least for VV polarization). Both elements are located in the upper part. Consequently, the X-band microwave backscatter for medium incidence angles of about 39° shows a strong sensitivity to changes in the upper canopy. This also confirms reports by Brisco & Brown (1998) for multi-frequency crop monitoring. They stated that compared to the lower frequencies (C- and L-band), X-band has a significant higher contribution from the upper canopy. Unfortunately, in our study there are no acquisitions before DAT 35. Especially at the early growing stages until the first peak, X-band appears to be more effective for crop parameter estimation such as plant height and biomass, since the temporal variation of backscatter is much higher than for C-band data, as reported by Kim et al. (2000). For L-band data, no temporal backscatter variation before DAT 40 was found, except for incidence angles greater than 50° (Inoue et al. 2002). All frequencies have in common that shallow incidence angles are better suited for monitoring of early growth stages and steep incidence angles show a later saturation level of σ^0 . Due to the different interactions with the canopy, multi-frequency space-borne data should be investigated more intensively concerning their complementary information content for rice monitoring as already done for sugarcane by Baghdadi et al. (2010).

Comparing correlation coefficients for VV polarization of HS and SM, significant lower values for SM can be observed. Due to the small experimental test parcels of 150 m^2 that are further reduced by a buffer at the border to exclude mixed pixels, only around 50 to 60 SM pixel per acquisition date can be used for analysis (pixel spacing: 1.25m).

For HS data, around 400 pixels per acquisition date can be used to analyse polarimetric backscatter (pixel spacing: 0.5 m). For this experimental configuration, the geometric accuracy with a residue of 1.6 m (RMSE), speckle and remaining mixed pixels can reduce the prediction accuracy of crop canopy parameters by SM images compared to high resolution HS data.

4.5.6.1 Incidence Angle

Incidence angle of SAR imaging is an important system parameter as the recorded signal gets sensitive to different properties of crop and soil.

To evaluate the potential of different incidence angles for rice monitoring, the multi-temporal time series were acquired between 26° and 46°. Comparing at first VV polarizations of HS and SM (see upper diagram in Figure 4-12) with a little incidence angle difference of 3°, it can be mentioned that the trend lines are very similar. Despite of the differences in look directions to the fields (ascending orbit for HS and descending for SM) and resolution the mutual deviation of the trend lines is lower than 0.4 dB for each date. A much higher variation can be observed by comparing the signatures of 26°, 39° and 46°. The maximum backscatter values of the VV trend lines vary between -12.2 dB for 46° and -8.8 dB for 26°, respectively between -10 dB (46°) and -3.5 dB (26°) for HH polarization. The minimum backscatter values of the VV trend lines vary between -16.3 dB (46°) and -11.3 dB (26°), respectively between -13.3 dB (46°) and -8.5 dB (26°) for HH polarization (see Figure 4-12). Unfortunately, there is no acquisition before DAT 35 in 2009, so the very early rice growth cannot be described. In 2011, acquisition starts at DAT 29 and both time series have a time offset of only two days. The amplitude difference between first and second acquisition is around 6 dB (VV) and around 8 dB (HH) at 26° and 1.5 dB (VV) and 3 dB (HH) at 46°. Expressed differently, the dynamic of the steep incidence angle within these 11 days is around three times higher than for the shallow one at both polarizations.

4.5.6.2 Polarimetric Parameters

In the recent study, the benefit of polarimetric parameters based on dual-polarimetric SAR data (co-pol phase difference, co-pol coherence, co-pol ratio and entropy-alpha decomposition) was investigated.

Polarimetric decompositions are originally designed for full polarimetric SAR data, whereas the target scattering coherency matrix is separated into basic scattering mechanism (Cloude 2010). This decomposition is based on the assumption, that scattering mechanism can be represented by means of the entropy-alpha space. As full polarimetric data is not always available, the polarimetric exploitation has to be reduced to dual polarimetric data, described in Cloude (2007). For the dual polarimetric case, only half of the scattering matrix elements can be used for decomposition. In fact, this reduction of dimensionality does not provide the same comprehensive information content as quad polarimetric data (Ainsworth et al. 2008). However, in the recent study the entropy and alpha values show a physical response to different phenological stages of rice. Similar meaningful entropy-alpha decompositions based on dual-polarimetric data were demonstrated by Lopez-Sanchez et al. (2010) and Shan et al. (2011). The latter one revealed a slight degradation in information content by using dual-polarimetric images, but classification based on entropy and alpha was still applicable with satisfactory results. Comparing the entropy and alpha response of rice to other land cover classes, it could be mentioned, that especially the alpha signature is well suited for separating rice from other land cover (see Appendix A.3). Based on the strong differential extinction of rice, the alpha value decreases (from DAT 35 to DAT 65) although double bounce scattering is still valid. Lopez-Sanchez et al. (2011) observed similar characteristic and attributes this to vertically oriented volume that behaves like a polarization filter.

The correlation parameters co-polar phase difference and inter-channel coherence were analysed. As already mentioned, the inter-channel coherence at incidence angle of 25° is below 0.5 at all acquisitions, which is caused by strong attenuation of VV backscatter with respect to HH backscatter. This differential extinction enables the separation between phenological stages of rice and from other land cover classes. The coherence is not suited to differentiate between growth stages of rice, as it stays more or less constant over the growing period. But the coherence is well suited, to separate rice to other land cover classes (see Figure 4-21). The coherence of rice is very low at around 0.4, all other classes are between 0.7 and 0.9. Compared to coherence, the phase difference shows a distinct signature depending on the growth stage. To acquire data at a certain phenological stage is of high importance to ensure an accurate

growth stage monitoring. As repeat passes of satellites (TerraSAR-X 11 days) could prevent a timely monitoring, the concept of a constellation mission to reduce repeat cycle is also beneficial for agricultural applications. To fly in constellation with a “twin” satellite, the repeat pass could be reduced to 5 days by operating in same orbit with a 32.7° phasing. This constellation is foreseen for the two satellites TerraSAR-X and the identical PAZ (Koppe et al., submitted).

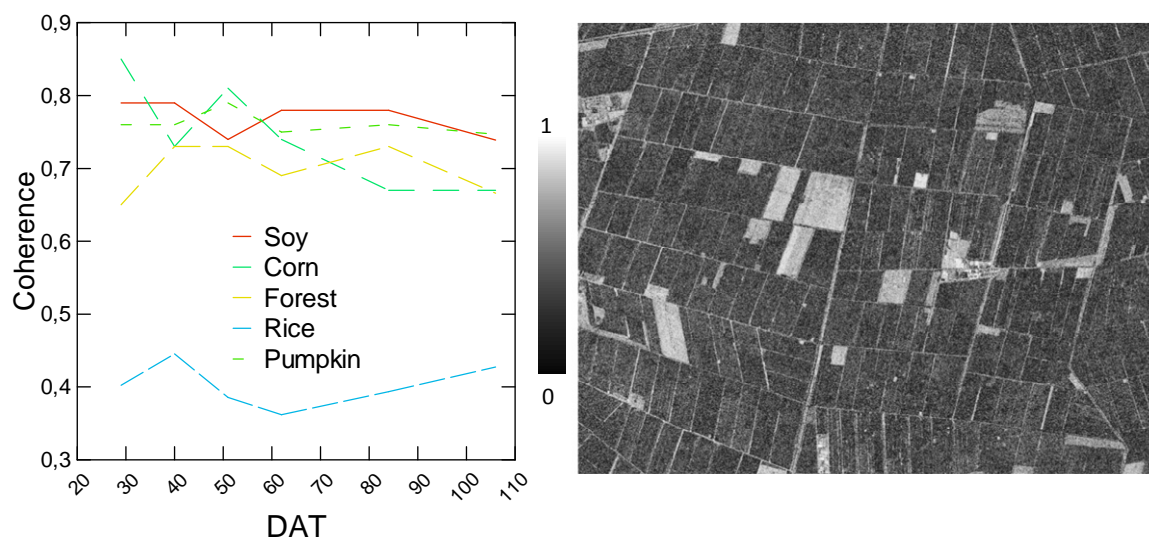


Figure 4-21: Left: Comparison of coherence signatures of different land cover classes. Right: Coherence image (July 7, 2011).

5 SYNERGISTIC SUMMARY AND CONCLUSION*

Food security in the light of population growth and global climate change becomes more and more important as the natural resources are limited. Sustainable management and regular monitoring of agricultural resources are important key factors of food safety for the next decades (Grunert 2005). In this context, remote sensing is a good tool for monitoring the agricultural environment on different scales to provide planning and decision support. In crop monitoring, remote sensing technologies have become indispensable in terms of acreage estimation, production control, yield estimation and damage assessment (Liaghat & Balasundram 2010). Major organizations and initiatives such as WB, WFP, FAO, GMES or MARS are using remotely sensed data to support continental and global crop monitoring services. Based on the wide range of satellite systems currently available, multi-sensoral data are of special interest to meet temporal and spatial requirements of monitoring services.

In the present thesis, the main emphasis was on investigating the potential of multi-sensoral and multi-temporal data for crop monitoring on a regional scale. More precisely, multi-spectral, hyperspectral and microwave data were acquired in order to derive crop parameters at different growth stages. The focal points of the study were:

- Making hyperspectral band math a useful tool for improving crop parameter prediction
- Exploring the capabilities of microwave data for crop stage monitoring. Special attention in this case is put on X-band polarimetric data analysis.

This chapter will summarise and synthesise the main findings of this study. It will further indicate the practical relevance of the research in conjunction with their limitations and recommendation with respect to future research.

* This section and sub-sections are an extended version of the articles: Koppe et al. (2010a); Koppe et al. (2012); Koppe et al. (2013).

5.1 Hyperspectral Imaging

This study compared vegetation indices calculated from multispectral and hyperspectral satellite remote sensing data for estimating winter wheat aboveground biomass, plant nitrogen concentration and plant height in North China Plain, and identified better vegetation indices by systematically evaluating all possible two band combinations using Hyperion satellite hyperspectral remote sensing data from 400 to 2500 nm. The results indicated that TVI showed the best performance among the analysed vegetation indices using either broad ($R^2 = 0.69, 0.32$ and 0.64 for biomass, N concentration and plant height, respectively) or narrow bands ($R^2 = 0.71, 0.33$ and 0.65 for biomass, N concentration and plant height, respectively). For the evaluated standard vegetation indices, narrow band indices only had slight improvements over corresponding broad band indices. The best performing Normalized Ratio Indices (NRI) selected through band combination analysis were significantly better than TVI, achieving R^2 of $0.83, 0.81$ and 0.79 for biomass, plant N concentration and plant height, respectively. They all used wavebands from the near infrared (NIR) (centred at 874, 732, and 763 nm) and short wave infrared (SWIR) (centred at 1225 and 1305 nm) spectrum with varying bandwidth between 10 and 190 nm. The results of this study suggest that it is important to include SWIR bands in multispectral satellite sensors for agricultural crop growth status monitoring. More studies are needed to further evaluate the results using data from more diverse conditions.

We can conclude that narrow band vegetation indices calculated from all possible waveband combination from Hyperion data perform much better for winter wheat parameters estimation on a regional level than standard vegetation indices calculated from red and NIR wavebands. Comparing all three index calculations, it was observed that two-band indices calculated according to equation 3.4 performed much better for estimation of aboveground biomass and total nitrogen content with at least 12% improvement for aboveground biomass and 48% for plant nitrogen content for winter wheat in the North China Plain. Because satellite image data were acquired at shooting and heading stage with a canopy closure of almost 100%, the saturation effect was obvious. This saturation effect is pointed out in a flat slope for regression between standard NDVI and aboveground biomass in Figure 4-9. Compared to this, the slope of

the regression line is much steeper using bands from the NIR and SWIR for index calculation. The results of band combination showed, that the saturation problem occurring for standard vegetation indices can be overcome by using different combinations for narrow band indices.

5.2 SAR C-band Imaging and Synergism of Optic and SAR

Envisat ASAR C-VV data show certain sensitivity to aboveground biomass. Bivariate regression analysis resulted in a coefficient of determination of about 0.75 for biomass. The simplified relationship between backscatter and crop condition is valid from jointing to heading stage. Before jointing and after heading stage, sophisticated models are necessary to separate backscatter contributions to retrieve canopy parameters.

In general, optical and SAR data provide complementary information from a vegetated surface. Hyperspectral sensors record surface reflectance in a wide range of the electromagnetic spectrum which provides the opportunity to extract information about crop canopy parameters and processes at pixel level. SAR microwave penetrate the vegetation and backscatter provide information from inside the canopy. Because of inherent speckle, backscatter values must be spatially averaged for regression analysis. Both kinds of information could be analysed separately or combined on a feature level. In a final investigation, crop parameters were related to combined C-VV backscatter and hyperspectral indices by means of a multiple regression model. For the relationship with biomass and plant height, regression models with coefficients of determination of 0.90 for biomass were established. This is an improvement of around 9% for aboveground biomass in comparison to single source hyperspectral regression model. While performance improvement is not that much of a combined model, the synergism of using complementary systems in monitoring winter wheat is obvious.

Improvements are more likely to be found in terms of filling acquisition gaps of optical data due to cloud cover and providing additional information by SAR.

5.3 SAR X-band Imaging

Rice crop growth was investigated using multi-temporal co-polar TerraSAR-X data. The results from the recent study are expected to improve the understanding of spaceborne X-band backscattering behaviour of rice crops. Concerning the experimental fields, it was important to apply different N rates to get different growth rates on the plots and hence a greater heterogeneity in biomass. Results obtained in this study demonstrated the potential of TerraSAR-X imagery for rice monitoring. The study had two objectives; one was to understand the X-band microwave backscatter behaviour during the growing season. The other was to investigate the relationship of backscatter coefficients with scattering elements of rice at a certain growth stage. The growth stages of rice generate a distinctive backscattering signature that can be separated from other land use classes. The signatures of both polarisation show two phases of backscatter increase, one at the beginning up to DAT 46 and a second one from DAT 80 onwards. Between these two phases, the backscatter strongly decreases. An interpretation of this unique signature was provided in this contribution. The results obtained from the correlation analysis show a strong sensitivity of X-band backscatter to changes within the upper canopy during the growth of rice. This includes a significant relationship between VV backscatter and heads after heading around DAT 70. In contrast to the sensitivity to changes in the upper canopy, microwave X-band data are not well suited for total biomass monitoring during the whole growing season due to an early saturation level compared to longer wavelength. To improve the relation of backscatter with the total biomass, a steeper incidence angle is required. Concerning this angular dependence of backscatter, further investigation is needed.

However, based on literature and the recent study, higher frequencies such as X-band are more suitable for change monitoring in the early vegetative stage because of the high dynamic range in a short time. Also the monitoring of changes in the upper canopy can be monitored. For relating biomass increase to microwave backscatter over a longer time, lower frequencies should be preferred.

Based on the results of the investigations, the proposed applications are the total biomass monitoring from transplanting to backscatter maximum as well as the rice

field identification based on the SAR data signature. Furthermore, X-band data are also suitable for monitoring changes in the upper canopy during the growing season. Changes can occur due to development of the plants, cultivation problems (e.g., diseases, water deficiency), and also the emergence of the panicle.

5.4 Validation of Hypothesis and Objectives

In chapter 1.4 the hypothesis and the objectives of the four sub-topics are formulated. In the following, the objectives are addressed in terms of validity.

5.4.1 Huimin Test Site

Concerning the multi-spectral and hyperspectral winter wheat monitoring, the objectives were successfully treated. Different kinds of vegetation indices (broad and narrow band standard vegetation indices) were compared and validated. Furthermore, a model for combining different wavebands to find most sensitive combinations was developed. Overall, it was possible to derive biophysical crop parameters by all of the vegetation indices in a statistically valid manner. But it was also clearly shown, that application of narrow band waveband combination performed best for biomass modelling.

For the relationship of hyperspectral data to crop conditions, narrow band Normalized Ratio Indices based on NIR (875 nm) and SWIR (1225 nm) were calculated for the 2006 growing cycle. As expected, hyperspectral indices show a much higher sensitivity to winter wheat conditions than C-VV radar data. Coefficient of determination was 0.83 for aboveground biomass for multi-temporal approach. In this case, the C-VV data are suggested to provide complementary information or to fill gaps if the hyperspectral information is not available.

To test the validity of the hyperspectral bivariate model, the established model of 2006 was applied to 2007 data to predict aboveground biomass. The predicted vs. measured 1:1 plot resulted in a high coefficient of determination ($R^2 = 0.84$), which proves inter-year validity of hyperspectral prediction power. Compared to multi-temporal approach, single date biomass prediction is less accurate as coefficient of

determination is only between 0.19 and 0.58 and RMSE is high (see Table 4-5). This is caused by lower variability of aboveground biomass across all fields at a given date.

Combining models from multi-sensoral data, the results outperform the single source estimations.

Table 5-1: Validation of objective and hypothesis for Huimin test site.

Objective	Chapter
<i>Multispectral and hyperspectral remote sensing</i>	
to quantitatively describe hyperspectral reflectance signature of winter wheat canopy during the vegetation period	4.2.1
to analyse, compare and evaluate satellite based multispectral and hyperspectral images in terms of broad band and narrow band vegetation indices for the estimation of winter wheat aboveground biomass, plant N concentration and plant height.	4.2.2
standard broad band and narrow band vegetation indices derived from multispectral sensor ALI	4.2.2.2
systematic identification of best waveband combinations in the Hyperion reflectance spectrum from 400 to 2500 nm	4.2.2.3 4.2.2.4
to investigate the ability to predict crop standing biomass by the different vegetation indices	4.2.2
<i>C-band microwave remote sensing</i>	
to quantitatively describe C-VV SAR backscattering of winter wheat canopy during the vegetation period	4.3.1
to investigate the ability to predict crop standing biomass by Envisat ASAR	4.3.2
<i>Synergy of hyperspectral and C-band microwave remote sensing</i>	
to explore the potential of complementary use of SAR and hyperspectral data for mapping crop and field conditions at a regional level	4.4

5.4.2 Jiansanjiang Test Site

For the test site Jiansanjiang, the identified objectives were all covered successfully. The polarimetric X-band backscatter signature was analysed in dependence on different incidence angles and phenological stages. A clear and unique signature was identified, that is well suited for crop growth stage monitoring. The backscatter intensities at different phenological stages were then related to standing biomass of rice. It was shown, that especially at the beginning of the growing season, there is a significant relationship with total biomass, but because of the low penetration depth, the relationship is rapidly decreasing. So it is suggested, that at the very early growing season, the X-band can be used for total biomass modelling. Apart from this, the lower penetration depth is well suited for monitoring changes in the upper part of the canopy. Based on the dual-polarimetric scattering behaviour and derived polarimetric parameters, a classification scheme for different growth stages was presented. The idea behind it is the determination of the growth stage based on a mono-temporal acquisition.

Table 5-2: Validation of objective and hypothesis for Jiansanjiang test site.

Objective	Chapter
<i>X-band microwave remote sensing</i>	
to assess the potential of high-resolution and multi-polarization X-band SAR data in agricultural monitoring	4.5
to study the sensitivity of X-band co-polar backscatter as a function of rice phenology stages based on multi-temporal acquisitions and different incidence angles	4.5.1
to evaluate the relationship between X-band co-polar backscatter and biomass of the different scattering layers (stem, leaf, and head)	4.5.4
to analyse to benefit of dual polarimetric X-band data for crop growth status monitoring	4.5.5

6 REFERENCES

- AINSWORTH, T. L., KELLY, J., & LEE, J.-S., 2008: Polarimetric Analysis of dual polarimetric SAR Imagery. – IGARSS 2008.
- ALBERTZ, J., 2009: Grundlagen der Interpretation von Luft- und Satellitenbildern. Eine Einführung in die Fernerkundung. Wissenschaftliche Buchgesellschaft. Darmstadt.
- ALLEN, D. M., 1974: The relationship between variable selection and data augmentation and a method for prediction. – *Technometrics*, **16**: 125-127.
- ASD (ANALYTICAL SPECTRAL DEVICES), 1999: Technical guide. <http://www.asdi.com>.
- BAGHDADI, N., BOYER, N., TODOROFF, P., EL HAJJ, M., & BÉGUÉ, A., 2010: Potential of SAR sensors TerraSAR-X, ASAR-ENVISAT and PALSAR-ALOS for monitoring sugarcane crops on Reunion Island. – *Remote Sensing of Environment*, **113**: 1724–1738.
- BALLESTER-BERMAN, J. D., LOPEZ-SANCHEZ, J. M., & FORTUNY-GUASCH, J., 2005: Retrieval of biophysical parameters of agricultural crops using polarimetric SAR interferometry. – *IEEE Transactions on Geoscience and Remote Sensing*, **43**(4): 683-694.
- BAMLER, R., & SCHÄTTLER, B., 1993: SAR data acquisition and image formation. – SCHREIER, G. (ED.): SAR geocoding: Data and Systems. Wichmann-Verlag, Karlsruhe.
- BAN, Y., & HOWARTH, P. J., 1998: Orbital effects on ERS-1 SAR temporal backscatter profiles of agricultural crops. – *International Journal of Remote Sensing*, **19**: 3465-3470.
- BARET, F., & GUYOT, G., 1991: Potentials and Limits of Vegetation Indices for LAI and APAR Assessment. – *Remote Sensing of Environment*, **35**: 161-173.
- BERK, A., ANDERSON, G. P., ACHARYA, P. K., CHETWYND, J. H., BERNSTEIN, L. S., SHETTLE, E. P., MATTHEW, M. W., & ADLER-GOLDEN, S. M., 2000: MODTRAN4 User's Manual. – Hanscom AFB, MA: Air Force Research Laboratory.
- BIGGAR, S. F., THOME, K. J., & WISNIEWSKI, W., 2003: Vicarious Radiometric Calibration of EO-1 Sensors by Reference to High-Reflectance Ground Targets. – *IEEE Transactions on Geoscience and Remote Sensing*, **41** (6): 1174-1179.
- BLAES, X., & DEFOURNY, P., 2003: Retrieving Crop Parameters Based on Tandem ERS 1/2 Interferometric Coherence Images. – *Remote Sensing of Environment*, **88**: 374-385.
- BLAES, X., VANHALLE, L., & DEFOURNY, P., 2005: Efficiency of crop identification based on optical and SAR image time series. – *Remote Sensing of Environment*, **96**(3-4): 352-365.
- BORENGASSER, M., HUNGATE, W. S., & WATKINS, R., 2007: Hyperspectral Remote Sensing: Principles and Applications. CRC Press, Boca Raton.
- BOUMAN, B. A. M., KROPFF, M. J., TUONG, T. P., WOPEREIS, M. C. S., TEN BERGE, H. F. M., & VAN LAAR, H. H., 2001: ORYZA2000: Modeling Lowland Rice. – International Rice Research Institute, Los Baños, Philipines and Wageningen. University and Research Centre, Wageningen, The Netherlands.

- BOUVET, A., LE TOAN, T., & LAM-DAO, N., 2009: Monitoring of the Rice Cropping System in the Mekong Delta Using ENVISAT/ASAR Dual Polarization Data. – *IEEE Transactions on Geoscience and Remote Sensing*, **47**(2): 517-526.
- BREMNER, J. M., 1960: Determination of nitrogen in soil by the Kjeldahl method. – *Journal of Agricultural Science*, **55**: 11-33.
- BRISCO, B., & BROWN, R. J., 1995: Multidate SAR/TM synergism for crop classification in western Canada. – *Photogrammetric engineering and remote sensing*, **61**: 1009-1014.
- BRISCO, B., & BROWN, R. J., 1998: Agricultural applications with radar. – HENDERSON, F. M., & LEWIS, A. J. (ED.): *Principles and Applications of Imaging Radar*. John Wiley & Sons, New York.
- BROGE, N. H., & LEBLANC, E., 2000: Comparing predicting power and stability of broadband and hyperspectral vegetation indices for estimation of green leaf area index and canopy chlorophyll density. – *Remote Sensing of Environment*, **76**: 156-172.
- BROGE, N. H., & MORTENSEN, J. V., 2002: Deriving green crop area index and canopy chlorophyll density of winter wheat from spectral reflectance data. – *Remote Sensing of Environment*, **81**: 45-57.
- BROWN, S. C. M., QUEGAN, S., MORRISON, K., BENNETT, J. C., & COOKMARTIN, G., 2003: High-Resolution Measurements of Scattering in Wheat Canopies Implications for Crop Parameter Retrieval. – *IEEE Transactions on Geoscience and Remote Sensing*, **41**: 1602-1610.
- CAIRNS, B., 2003: SPECIAL ISSUE PAPERS – Atmospheric Correction and its Application to an Analysis of Hyperion Data. – *IEEE Transactions on Geoscience and Remote Sensing*, **41**(6): 1232-1245.
- CECCATO, P., GOBRON, N., FLASSE, S., PINTY, B., & TARANTOLA, S., 2002: Designing a spectral index to estimate vegetation water content from remote sensing data: Part 1 Theoretical approach. – *Remote Sensing of Environment*, **82**: 188-197.
- CHAKRABORTY, M., MANJUNATH, K. R., PANIGRAHY, S., KUNDU, N., & PARIHAR, J. S., 2005: Rice crop parameter retrieval using multi-temporal, multi-incidence angle Radarsat SAR data. – *ISPRS Journal of Photogrammetric and Remote Sensing*, **59**(5): 310-322.
- CHANG, Y. L., HAN, C. C., REN, H., CHEN, C.-T., CHEN, K. S., & FAN, K.-C., 2004: Data fusion of hyperspectral and SAR images. – *Optical Engineering*, **43**: 1787-1797.
- CHEN, C.-M., HEPNER, G. F., & FORSTER, R. R., 2003: Fusion of hyperspectral and radar data using the IHS transformation to enhance urban surface features. – *ISPRS Journal of Photogrammetry and Remote Sensing*, **59**: 310-322.
- CHEN, J., & LIN, H., 2005: The application of ENVISAT ASAR data for rice growth monitoring based on semi-empirical backscattering model. – 26th Asian Conference on Remote Sensing, Hanoi, Vietnam.
- CHEN, J., & TIAN, Q., 2006: Estimating canopy chlorophyll and nitrogen concentration of rice from EO-1 Hyperion data. – *Remote Sensing for Agriculture*. Proceedings of the SPIE 6359.
- CHO, M. A., SKIDMORE, A. K., & ATZBERGER, C., 2008: Towards red-edge positions less sensitive to canopy biophysical parameters for leaf chlorophyll estimation using

- properties optique spectrales des feuilles (PROSPECT) and scattering by arbitrarily inclined leaves (SAILH) simulated data. – *International Journal of Remote Sensing*, **29**(8): 2241-2255.
- CHOUHDURY, I., CHAKRABORTY, M., & PARIHA, J. S., 2007: Estimation of Rice Crop Growth Parameter and Crop Phenology with Conjunctive Use of Radarsat and Envisat. – *Proceedings Envisat Symposium 2007*. Montreux, Switzerland, April 23–27, 2007, ESA SP-636.
- CLOUDE, S. R., 2007: The dual polarization entropy/alpha decomposition: a PALSAR case study. – *POLinSAR Workshop*, June 22-26th, 2007. Frascati, Italy. ESA Abstract Book.
- CLOUDE, S. R., 2010: *Polarisation Applications in Remote Sensing*. Oxford University Press, Oxford.
- CLOUDE, S. R., & POTTIER, E., 1997: An Entropy Based Classification Scheme for Land Applications of Polarimetric SAR. – *IEEE Transactions on Geoscience and Remote Sensing*, **35**(1): 68-78.
- COOPS, N. C., SMITH, M.-C., MARTIN, M. E., & OLLINGER, S. V., 2003: Prediction of Eucalypt Foliage Nitrogen Content From Satellite-Derived Hyperspectral Data. – *IEEE Transactions on Geoscience and Remote Sensing*, **41**(6): 1338-1346.
- DATT, B., MCVICAR, T. R., VAN NIEL, T. G., JUPP, D. L. B., & PEARLMAN, J. S., 2003: Pre-processing EO-1 Hyperion Hyperspectral Data to Support the Application of Agricultural Indexes. – *IEEE Transactions on Geoscience and Remote Sensing*, **41**(6): 1246-1259.
- DAUGHTRY, S. S. T., WALTHALL, C. L., KIM, M. S., DE COLSTOUN, E. B., & MCMURTREY, J. E., 2000: Estimating Corn Leaf Chlorophyll Concentration from Leaf and Canopy Reflectance. – *Remote Sensing of Environment* **74**: 229-239.
- DARVISHZADEH, R., SKIDMORE, A., SCHLERF, M., ATZBERGER, C., CORSIA, F., & CHOA, M., 2008: LAI and chlorophyll estimation for a heterogeneous grassland using hyperspectral measurements. – *ISPRS Journal of Photogrammetry and Remote Sensing*, **63**(4): 409-426.
- DE GROOTE, H., & TRAORÉ, O., 2005: The cost of accuracy in crop area estimation. – *Agricultural Systems*, **84**: 21-38.
- DENTE, L., SATALINO, G., MATTIA, F., & RINALDI, M., 2007: Assimilation of leaf area index derived from Asar and Meris data into Ceres-wheat model to map wheat yield. – *Remote Sensing of Environment*, **112**(4): 1395-1407.
- DORALSWAMY, P. C., MOULIN, S., COOK, P. W., & STERN, A., 2003: Crop yield assessment from remote sensing. – *Photogrammetric Engineering & Remote Sensing*, **74**: 665-674.
- EINER, M., MINET, C., STEIGENBERGER, P., & CONG, X., 2011: Imaging Geodesy - Toward Centimeter-Level Ranging Accuracy with TerraSAR-X. – *IEEE Transactions on Geoscience and Remote Sensing*, **49**(2): 661-671.
- FAO, 2013: *FAO statistical Yearbook, 2013*: <http://www.fao.org/economic/ess/ess-publications/ess-yearbook/en/#.UmvV2BA7A00> (accessed June 9, 2013).
- FAOSTAT, 2013: <http://www.faostat3.fao.org> (accessed June 9, 2013).

- FERWERDA, J. G., SKIDMORE, A. K., & MUTANGA, O., 2005: Nitrogen detection with hyperspectral normalized ratio indices across multiple plant species. – *International Journal of Remote Sensing*, **26**: 4083-4095.
- FILLELA, I., AMARO, J. L., & PENUELAS, J., 1996. Relationship between photosynthetic radiation-use efficiency of barley canopies and the photochemical reflectance index (PRI). *Physiology Plantarum*, **96**: 211-216.
- FRITZ, T., & EINEDER, M., 2010: TerraSAR-X Basic Product Specification Document. – TSX-GS-DD-3302, Issue 1.7. <http://infoterra.de/documents>.
- GALVAO, L. S., FORMAGGIO, A. R., & TISOT, D. A., 2005: Discrimination of sugarcane varieties in Southeastern Brazil with EO-1 Hyperion data. – *Remote Sensing of Environment*, **94**: 523-534.
- GANZEY, S. S., 2005: Transboundary geo-systems in the south of the Russian Far East and in northeast China. Vladivostok Dalnauka, Vladivostok.
- GAO, J., 2006: Canopy Chlorophyll Estimation by Remote Sensing. PhD thesis, Manhattan, Kansas, USA.
- GAO, B.-C., MONTES, M. J., DAVIS, C. O., & GOETZ, A. F. H., 2009: Atmospheric correction algorithms for hyperspectral remote sensing data of land and ocean. – *Remote Sensing of Environment*, **113**(1): 17-24.
- GHERBOUDJ, I., MAGAGI, R., BERG, A. A., & TOTH, B., 2011: Soil moisture retrieval over agricultural fields from multi-polarised and multi-angular RADARSAT-2 SAR data. – *Remote Sensing of Environment*, **115**(1): 33-43.
- GITELSON, A., MERZYAK, M.N., & LICHTENTHALER, K., 1996: Detection of red edge position and chlorophyll content by reflectance. – *Plant Physiology*, **148**: 501-508.
- GMES, 2012: <http://www.gmes.info> (accessed March 12, 2012).
- GNYP, M. L., MIAO, Y., YUAN, F., USTIN, S. L., YU, K., YAO, Y., HUANG, S., & BARETH, G., 2013: Hyperspectral canopy sensing of paddy rice aboveground biomass at different growth stages. – *Field Crops Research*, <http://www.sciencedirect.com/science/article/pii/S0378429013003298>.
- GNYP, M. L., BARETH, G., KOPPE, W., MIAO, Y., LENZ-WIEDEMANN, V. I. S., FEI, L., HENNIG, S. D., JIA, L., LAUDIEN, R., CHEN, X., & ZHANG, F.: Development and Implementation of a Multiscale Biomass Model using Hyperspectral Data for Winter Wheat in the North China Plain. – *International Journal of Applied Earth Observation and Geoinformation*, 2013 submitted.
- GONG, P., PU, R., BIGING, G. S., & LARRIEU, M. R., 2003: Estimation of Forest Leaf Area Index Using Vegetation Indices Derived From Hyperion Hyperspectral Data. – *IEEE Transactions on Geoscience and Remote Sensing*, **41**(6): 1355-1362.
- GRUNERT, K. G., 2005: Food quality and safety: consumer perception and demand. – *European Review of Agricultural Economics*, **32**(3): 369-391.
- HABOUDANE, D., MILLER, J. R., PATTEY, E., ZARCO-TEJADA, P. J., & STRACHAN, I. B., 2004: Hyperspectral vegetation indices and novel algorithms for predicting green LAI of crop canopies: Modeling and validation in the context of precision agriculture. – *Remote Sensing of Environment*, **90**: 337-352.
- HAJNSEK, I., KRIEGER, G., KOSTAS, P., BAUMGARTNER, S., RODRIGUEZ-CASSOLA, M., & PRATS, P., 2010: TanDEM-X: First Scientific Experiments during the Commissioning Phase. – 8th European Conference on Synthetic Aperture Radar, 7-10 June, Aachen.

- HANSEN, P. M., & SCHJOERRING, J. K., 2003: Reflectance measurement of canopy biomass and nitrogen status in wheat crops using normalized difference vegetation indices and partial least square regression. – *Remote Sensing of Environment*, **86**: 542-553.
- HELD, A., TICEHURST, C., LYMBURNER, L., & WILLIAMS, N., 2003: High resolution mapping of tropical mangrove ecosystems using hyperspectral and radar remote sensing. – *International Journal of Remote Sensing*, **24**: 2739-2759.
- HENDERSON, F. M., & LEWIS, A. J. (ed), 1998: Principles and Applications of Imaging Radar. John Wiley & Sons, New York.
- HUETE, A. R., 1988: A soil vegetation adjusted index (SAVI). *Remote Sensing of Environment*, **25**(2): 295-309.
- HÜTT, C., 2012: Potential von hochauflösenden, multitemporalen und dual-polarimetrischen TerraSAR-X Radaraufnahmen für Landnutzungsklassifikationen. Diploma thesis, University of Cologne.
- ILRI, 1989: Effectiveness and Social/Environmental Impacts of Irrigation Projects: a Review. – Annual Report 1988, International Institute for Land Reclamation and Improvement (ILRI), Wageningen, The Netherlands.
- INOUE, Y., KUROSU, T., MAENO, H., URATSUKA, S., KOZU, T., DABROWSKA-ZIELINSKA, K., & QI, J., 2002: Season-long daily measurements of multifrequency (Ka, Ku, X, C, and L) and full-polarization backscatter signatures over paddy rice field and their relationship with biological variables. – *Remote Sensing of Environment*, **81**: 194-204.
- IRRI, 2011: International Rice Research Institute, Annual Report. <http://www.irri.org/ar2009> (accessed May 13, 2011).
- ISHITSUKA N., SAITO, G., OUCHI, K., & URATSUKA, S., 2004: Observation of Japanese rice paddy fields using multi wavelength and full polarimetric SAR – Remote sensing sensor on next generation satellite. – *Advances in Astronautical Sciences*, **117**: 565-575.
- ITT VISUAL INFORMATION SOLUTIONS, 2011: <http://www.exelisvis.com/> (accessed August 15, 2011).
- JAMER, T., KÖTZ, B., & ATZBERGER, C., 2003: Spektroradiometrische Ableitung biophysikalischer Vegetationsparameter von Weizenbeständen: Vergleichende Untersuchung verschiedener empirisch-statistischer Verfahren. – *Photogrammetrie, Fernerkundung, Geoinformatik*, **1**: 43-50.
- JINSONG, C., HUI, L., & ZHIYUAN, P., 2007: Application of ENVISAT ASAR Data in Mapping Rice Crop Growth in Southern China. – *IEEE Geoscience and Remote Sensing Letters*, **4**(3): 431-435.
- JONGSCHAAP, R. W. W., & SCHOUTEN, L. S. M., 2005: Predicting wheat production at regional scale by integration of remote sensing data with a simulation model. – *Agronomy for sustainable development*, **25**: 481-489.
- JU, X. T., KOU, C. L., ZHANG, F. S., & CHRISTIE, P., 2006: Nitrogen balance and groundwater nitrate contamination: comparison among three intensive cropping systems on the North China Plain. – *Environmental Pollution*, **143**: 117-125.

- JUSTICE, C. O., & BECKER-RESTEF, I., 2007: Report from the Workshop on Developing a Strategy for Global Agricultural Monitoring in the Framework of the Group on Earth Observation (GEO), UN/FAO, Rome, July 2007.
- KARJALAINEN, M., KAARTINEN, H., & HYYPPÄ, J., 2008: Agricultural Monitoring Using Envisat Alternating Polarization SAR Images. – *Photogrammetric Engineering & Remote Sensing*, **74**: 117-124.
- KHURSHID, K., STAENZ, K., SUN, L., NEVILLE, R., WHITE, H. P., BANNARI, A., CHAMPAGNE, C. M., & HITCHCOCK, R., 2006: Preprocessing of EO-1 Hyperion data. – *Canadian Journal of Remote Sensing*, **32**: 84-97.
- KIM, S.-B., KIM, B.-K., KONG, Y.-K., & KIM, Y.-S., 2000: Radar backscattering measurements of rice crop using X-band scatterometer. – *IEEE Transactions on Geoscience and Remote Sensing*, **38**(3): 1467-1471.
- KIM, Y.-H., HONG, S. Y., & LEE, H., 2008: Radar Backscattering Measurement of a Paddy Rice Field using Multi-frequency (L, C and X) and Full-polarization. – *IGARSS Geoscience Remote Sensing Symposium*, 7-11 July Boston, 553-556.
- KLAUSING, H., & HOLPP, W. (ed.), 2000: Radar mit realer und synthetischer Apertur. Oldenbourg Wissenschaftsverlag, München.
- KOPPE, W., GNYP, M. L., LAUDIEN, R., JIA, L., LI, F., CHEN, X., ZHANG, F., & BARETH, G., 2006: Deriving of winter wheat characteristics from combined radar and hyperspectral data analysis. – *SPIE Proceedings, Geoinformatics'2006*, Wuhan, China.
- KOPPE, W., BACH, K., & LUMSDON, P., submitted: Benefits of TerraSAR-X – PAZ Constellations for Maritime Surveillance. – 10th European Conference on Synthetic Aperture Radar, EUSAR, 3-5 June 2014, Berlin.
- KOPPE, W., LI, F., GNYP, M. L., MIAO, Y., JIA, L., CHEN, X., ZHANG, F., & BARETH, G., 2010a: Evaluating Multispectral and Hyperspectral Satellite Remote Sensing Data for Estimating Winter Wheat Growth Parameters at Regional Scale in the North China Plain. – *Photogrammetrie, Fernerkundung, Geoinformation*, **3**: 167-178.
- KOPPE, W., KIEFL, N., HENNIG, S. D., & JANOTH, J., 2010b: Validation of Pixel Location Accuracy of Orthorectified TerraSAR-X Products. – 8th European Conference on Synthetic Aperture Radar, Aachen, 7-10 June, Aachen.
- KOPPE, W., & KIEFL, N., 2010: Terrapid-3D. Filter Methods for SAR data preparation for image fusion with optical data. Technical Note. Project confidential.
- KOPPE, W., GNYP, M. L., YAO, Y., MIAO, Y., & BARETH, G., 2011: Agricultural Monitoring with Spaceborne X-band SAR Data. – *Proceedings on the Workshop of Remote Sensing Methods for Change Detection and Process Modelling*, 18-19 November 2010, University of Cologne, Germany. *Kölner Geographische Arbeiten*, **92**: 55-61.
- KOPPE, W., HENNIG, S. D., LI, F., GNYP, M. L., MIAO, Y., JIA, L., CHEN, X., & BARETH, G., 2012: Multi-Temporal Hyperspectral and Radar Remote Sensing for Estimating Winter Wheat Biomass in the North China Plain. – *Photogrammetrie, Fernerkundung, Geoinformation*, **3**: 281-298.
- KOPPE, W., LI, F., GNYP, M. L., HÜTT, C., MIAO, Y., YAO, Y., CHEN, X., & BARETH, G., 2013: Rice monitoring with multi-temporal and dual-polarimetric TerraSAR-X data. – *International Journal of Applied Earth Observation and Geoinformation*, **21**: 568-576.

- KOYAMA, C. N., KORRES, W., FIENER, P., & SCHNEIDER, K., 2010: Variability of Surface Soil Moisture Observed from Multi-temporal C-band SAR and Field Data. – *Vadose Zone Journal*, **9**(4): 1014-1024.
- KÜHBAUCH, W., & HAWLITSCHKA, S., 2003: Remote sensing – a future technology in precision farming. – *Proceedings of the Workshop on POLinSAR. Applications of SAR Polarimetry and Polarimetric Interferometry (ESA SP-529)*.
- KUMAR, L., SCHMIDT, K., DURY, S., & SKIDMORE, A., 2003: Imaging spectrometry and vegetation science. – VAN DER MEER, F. D., & DE JONG, S. M. (ed.): *Imaging Spectrometry*. Springer, Dordrecht.
- LAM-DAO, N., LE TOAN, T., APAN, A., BOUVET, A., YOUNG, F., & LE VAN, T., 2009: Effects of changing rice cultural practices on C-band synthetic aperture radar backscatter using Envisat advanced synthetic aperture radar data in the Mekong River Delta. – *Journal of Applied Remote Sensing*, **3**(1).
- LANCASHIRE, P. D., BLEIHOLDER, H., LANGELÜDDECKE, P., STAUSS, R., VAN DEN BOOM, T., WEBER, E., & WITZEN-BERGER, A., 1991: An uniform decimal code for growth stages of crops and weeds. – *Annals of applied Biology*, **119**: 561-601.
- LAUDIEN, R., & BARETH, G., 2006: Multitemporal Hyperspectral Data Analysis for Regional Detection of Plant Diseases by using a Tractor-and an Airborne-based Spectrometer. – *Photogrammetrie, Fernerkundung, Geoinformation*, **3**: 217-228.
- LEE, K.-S., COHAN, W. B., KENNEDY, R. E., MAIERSPERGER, T. K., & GOWER, S. T., 2004: Hyperspectral versus multispectral data for estimation leaf area index in four different biomes. – *Remote Sensing of Environment*, **91**: 508-520.
- LE TOAN, T., LAUR, H., MOUGIN, E., & LOPES, A., 1989: Multitemporal and dual-polarization observations of agricultural vegetation covers by X-band SAR images. – *IEEE Transactions on Geoscience and Remote Sensing*, **27**: 709-717.
- LIAGHAT, S., & BALASUNDRAM, S. K., 2010: A review: The role of remote sensing in precision agriculture. – *American Journal of Agricultural and Biological Sciences*, **5**(1): 50-55.
- LI, F., GNYP, M. L., JIA, L., MIAO, Y., YU, Z., KOPPE, W., BARETH, G., CHEN, X., & ZHANG, F., 2008: Estimating N status of winter wheat using a handheld spectrometer in the North China Plain. – *Field Crops Research*, **106**: 77-85.
- LILLESAND, T. M., KIEFER, R. W., & CHIPMAN, J. W. (ed.), 2008: *Remote Sensing and Image Interpretation*. John Wiley & Sons, New York.
- LIM, K.-S., TAN, C.-P., KOAY, J.-Y., KOO, V. C., EWE, H. T., LO, Y.-C., & ALI, A., 2007: Multitemporal C-Band Radar Measurement on Rice Fields. – *PIERS Online*, **3**: 44-47.
- LIN, H., CHEN, J., PEI, Z., & ZHANG, S., 2009: Monitoring Sugarcane Growth Using ENVISAT ASAR Data. – *IEEE Transactions on Geoscience and Remote Sensing*, **48**(8): 2572-2580.
- LIU, L., WANG, J., BAO, Y., HUANG, W., MA, Z., & ZHAO, C., 2006: Predicting winter wheat condition, grain yield and protein content using multi-temporal EnviSat-ASAR and Landsat TM satellite images. – *International Journal of Remote Sensing*, **27**: 737-753.
- LOPEZ-SANCHEZ, J. M., BALLESTER-BERMAN, J. D., PAYA, S., CAZCARRA, V., & NAVARRO, V. D., 2010: An advanced electromagnetic model for rice fields at X-band:

- Development and interpretation of dual-pol TerraSAR-X images. – 8th European Conference on Synthetic Aperture Radar, Aachen, 7-10 June, Aachen.
- LOPEZ-SANCHEZ, J. M., & BALLESTER-BERMAN, J. D., 2009: Potentials of polarimetric SAR interferometry for agriculture monitoring. – *Radio Science*, **44**: 1-20.
- LOPEZ-SANCHEZ, J. M., CLOUDE, S. R., & BALLESTER-BERMAN, J. D., 2011: Retrieval of rice phenology by means of copolar dual-pol images provided by TerraSAR-X. – Proceedings of the 4th TerraSAR-X Science Team Meeting, DLR, Wessling, Germany, February 2011.
- LYON, J. G., YUAN, D., LUNETTA, R. S., & ELVIDGE, C. D., 1998: A Change Detection Experiment Using Vegetation Indices. – *Photogrammetric Engineering & Remote Sensing*, **64**: 143-150.
- MAITRE, H., 2013: Processing of Synthetic Aperture Radar (SAR) Images. SciTech Publishing. John Wiley & Sons, New York.
- MASSONNET, D., & SOUYRIS, J.-C., 2008: Imaging with Synthetic Aperture Radar. CRC Press, Boca Raton.
- MATTIA, F., LE TOAN, T., PICARD, G., POSA, F. I., D'ALESSIO, A., NOTARNICOLA, C., GATTI, A. M., RINALDI, M., & SATALINO, G., 2003: Multitemporal C-Band Radar Measurements on Wheat Fields. – *IEEE Transactions on Geoscience and Remote Sensing*, **41**(7): 1551-1560.
- MCNAIRN, H., & BRISCO, B., 2004: The application of C-band polarimetric SAR for agriculture: a review. – *Canadian Journal of Remote Sensing*, **30**: 525-542.
- MCNAIRN, H., CHAMPAGNE, C., SHANG, J., HOLMSTROM, D., & REICHERT, G., 2009: Integration of optical and synthetic aperture radar (SAR) imagery for delivering operational annual crop inventories. – *ISPRS Journal of Photogrammetry and Remote Sensing*, **64**: 434-449.
- MCNAIRN, H., HOCHHEIM, K., & RABE, N., 2004: Applying polarimetric radar imagery for mapping the productivity of wheat crops. – *Canadian Journal of Remote Sensing*, **30**: 517-524.
- MEIER, U., 2001: Growth stages of mono and dicotyledonous plants. – Federal Biological Research Centre for Agriculture and Forestry, <http://www.bba.de/veroeff/bbch/bbcheng.pdf>.
- MIAO, Y., MULLA, D. J., RANDALL, G. W., VETSCH, J. A., & VINTILA, R., 2009: Combining chlorophyll meter readings and high spatial resolution remote sensing images for in-season site-specific nitrogen management of corn. – *Precision Agriculture*, **10**: 45-62.
- MILLER, G. T., 2004: Sustaining the Earth. Thompson Learning, Pacific Grove.
- MORAN, M. S., INOUE, Y., & BARNES, E. M., 1997: Opportunities and limitations for image-based remote sensing in precision crop management. – *Remote Sensing of Environment*, **61**: 319-346.
- MOTT, H., 2006: Remote Sensing with Polarimetric Radar. John Wiley & Sons, New York.
- MULLA, D., 2012: Twenty five years of remote sensing in precision agriculture: Key advances and remaining knowledge gaps – *Biosystems Engineering*, **114**(4): 358–371.

- MUTANGA, O., & SKIDMORE, A. K., 2004: Narrow band vegetation indices overcome the saturation problem in biomass estimation. – *International Journal of Remote Sensing*, **25**: 3999-4014.
- NATIONAL BUREAU OF STATISTICS OF CHINA, 2010: China agriculture yearbook. China Agriculture Press.
- NEST – Next ESA SAR Toolbox. <http://nest.array.ca/web/nest> (accessed May 21, 2013).
- NGUYEN, H. T. & LEE, B.-W., 2006: Assessment of rice leaf growth and nitrogen status by hyperspectral canopy reflectance and partial least square regression. – *European Journal of Agronomy*, **24**: 349-356.
- OLIVER, C., & QUEGAN, S. (ed.), 2004: Understanding Synthetic Aperture Radar Images. SciTech, NC 27613.
- OPPELT, N., & MAUSER, W., 2004: Hyperspectral monitoring of physiological parameters of wheat during a vegetation period using AVIS data. – *International Journal of Remote Sensing*, **25**: 145-159.
- OTB SOFTWARE: <http://www.orfeo-toolbox.org> (accessed October 21, 2013).
- PEARLMAN, J. S., BARRY, P. S., SEGAL, C. C., SHEPANSKI, J., BEISO, D., & CARMAN, S. L., 2003: Hyperion, a Space-Based Imaging Spectrometer. – *IEEE Transactions on Geoscience and Remote Sensing*, **41**(6): 1160-1173.
- PENG, D., HUETE, A. R., HUANG, J., WANG, F., & SUN, H., 2011: Detection and estimation of mixed paddy rice cropping patterns with MODIS data. – *International Journal of Applied Earth Observation Geoinformation*, **13**: 13-23.
- PERONA, P., & MALIK, J., 1990: Scale-space and edge detection using anisotropic diffusion. – *IEEE Transactions on Pattern Analysis Machine Intelligence*, **12**: 629-639.
- PEARSON, J. S., & MILLER, L. D., 1972: Remote mapping of standing crop biomass for estimation of the productivity of the shortgrass prairie, pawnee national grassland, Colorado. *Proceedings of the 8th International Symposium on Remote Sensing of the Environment*, 1355-1379.
- PICARD, G., LE TOAN, T., & MATTIA, F., 2003: Understanding C-Band Radar Backscatter From Wheat Canopy Using a Multiple-Scattering Coherent Model. – *IEEE Transactions on Geoscience and Remote Sensing*, **41**: 1583-1591.
- PREVOT, L., CHAUKI, H., TROUFLEAU, D., WEISS, M., BARET, F. & BRISSON, N., 2003: Assimilating optical and radar data into the STICS crop model for wheat. – *Agronomie*, **23**: 297-303.
- RAN, Y. H., LI, X., & LU, L., 2010: Evaluation of four remote sensing based land cover products over China. – *International Journal of Remote Sensing*, **31**: 391-401.
- RANEY, R. K., & HOPKINS, J., 2011: A perspective on compact polarimetry. – *IEEE Transactions on Geoscience and Remote Sensing Newsletter*, **160**: 12-18.
- REIGBER, A., NEUMANN, M., FERRO-FAMIL, L., JAGER, M., & PRATS, P., 2008: Multi-baseline coherence optimisation in partial and compact polarimetric modes. – *IEEE Geoscience and Remote Sensing Symposium IGARSS*, July 7-11, 2008.
- REYNIERS, M., & VRINDTS, E., 2006: Measuring wheat nitrogen status from space and ground-based platform. – *International Journal of Remote Sensing*, **27**: 549-567.
- RIBBES, F., & LE TOAN, T., 1999a: Rice field mapping and monitoring with Radarsat data. – *International Journal of Remote Sensing*, **20**: 745-765.

- RIBBES, F., & LE TOAN, T., 1999b: Coupling radar data and rice growth model for yield estimation. – *Proceedings International Geoscience and Remote Sensing Symposium*, **4**: 2336-2338.
- RICHARDS, J. A., 2009: Remote sensing with imaging radar. Springer Verlag, Heidelberg.
- RICHTER, K., ATZBERGER, C., VUOLO, F., WEIHS, P., & D'URSO, G., 2009: Experimental assessment of the Sentinel-2 band setting for RTM-based LAI retrieval of sugar beet and maize. – *Canadian Journal of Remote Sensing*, **35**(3): 230-247.
- RONDEAUX, G., STEVEN, M., & BARETH, F., 1996: Optimization of soil-adjusted vegetation indices. – *Remote Sensing of Environment*, **55**: 95-107.
- ROSICH, B., & MEADOWS, P., 2004: Absolute Calibration of ASAR Level 1 Products. Technical Note. <http://earth.esa.int/> (accessed January 5, 2010).
- ROUSE, J. W., HAS, R. H., SCHELL, J. A. & DEERING, D. W., 1974: Monitoring vegetation systems in the Great Plains with ERTS. – *Third ERTS Symposium*, NASA Sp-351, Vol. 1 NASA: 309-317.
- SATALINO, G., MATTIA, F., LE TOAN, T., & RINALDI, M., 2009: Wheat Crop Mapping by Using ASAR AP data. – *IEEE Transactions on Geoscience and Remote Sensing*, **47**: 527-530.
- SEAMLESS, 2012: <http://www.seamless-ip.org/> (accessed March 12, 2012).
- SCHMIDT, K. S., & SKIDMORE, A. K., 2003: Spectral discrimination of vegetation types in a coastal wetland. – *Remote sensing of environment*, **85**: 92-108.
- SCHNEIDER, K., 2003: Assimilating remote sensing data into a land surface process model. – *International Journal of Remote Sensing*, **24**: 2959-2980.
- SCHOENWIESE, C.-D. 2006: *Praktische Statistik für Meteorologen und Geowissenschaftler*. Gebrüder Bornträger, Stuttgart.
- SCHOWENGERDT, R. A., 2007: Remote sensing: models and methods for image processing. Elsevier Academic Press, Amsterdam.
- SHAN, Z., WANG, C., ZHANG, H., & CHEN, J., 2011: H- α Decomposition and Alternative Parameters for Dual Polarization SAR Data. – *PIERS Proceedings*, Suzhou, China, September 12-16, 2011: 1386-1390.
- SHAO, Y., FAN, X., LIU, H., XIAO, J., ROSS, S., BRISCO, B., BROWN, R., & STAPLES, G., 2001: Rice monitoring and production estimation using multitemporal RADARSAT. – *Remote Sensing of Environment*, **76**: 310-325.
- SHEN, S. H., YANG, S. B., LI, B.B., TAN, B. X., LI, Z. Y., & LE TOAN, T., 2009: A scheme for regional rice yield estimation using ENVISAT ASAR data. *Science in China Series D: Earth Science*, **52**(8): 1183-1194.
- SIMS, D. A., & GAMON, J. A., 2002: Relationships between leaf pigment content and spectral reflectance across a wide range of species, leaf structures and development stages. – *Remote Sensing of Environment*, **81**: 337-354.
- SMITH, M.-L., MARTIN, M. E., PLOURDE, L., & OLLINGER V., 2003: Analysis of Hyperspectral Data for estimation of Temperate Forest Canopy Nitrogen Concentration: Comparison Between an Airborne (AVIRIS) and a Spaceborne (Hyperion) Sensor. – *IEEE Transactions on Geoscience and Remote Sensing*, **41**(6): 1332-1337.
- SORIA-RUIZ, J., FERNANDEZ-ORDONEZ, Y., & MCNAIRN, H., 2009: Corn Monitoring and Crop Yield Using Optical and Microwave Remote Sensing. – Ho, P.-G. P., (ed): *Geoscience and Remote Sensing*. InTech.

- STILES, J., SARABANDI, K., & ULABY, F., 2000: Electromagnetic scattering from grassland – Part II: Measurement and modeling results. – *IEEE Transactions on Geoscience and Remote Sensing*, **38**: 349-356.
- STRACHAN, I. B., PATTEY, E., & BOISVERT, J. B., 2002: Impact of nitrogen environmental conditions on corn as detected by hyperspectral reflectance. – *Remote Sensing of Environment*, **80**: 213-224.
- SUGA, Y., & KONOSHI, T., 2008: Rice crop monitoring using X, C and L band SAR data. *Proceedings SPIE 7104*, 16 September 2008, Cardiff, United Kingdom.
- TENNAKON, S. B., MURTY, V. V. N., & EIUMNOH, A., 1992: Estimation of cropped area and grain yield of rice using remote sensing data. – *Remote Sensing of Environment*, **13**: 427-439.
- THENKABAIL, P. S., LYON, J. G., & HUETE, A., 2011: *Hyperspectral Remote Sensing of Vegetation*. CRC Press, Boca Raton.
- THENKABAIL, P. S., SMITH, R. B., & DE PAUW, E., 2000: Hyperspectral vegetation indices and their relationships with agricultural crop characteristics. – *Remote Sensing of Environment*, **71**: 158-182.
- THENKABAIL, P. CHANG, S., ENCLONA, E. A., ASHTON, M. S., & VAN DER MEER, B., 2004: Accuracy assessment of hyperspectral waveband performance for vegetation analysis application. – *Remote Sensing of Environment*, **91**: 354-376.
- TOUZI, R., BOERNER, W. M., LEE, J. S., & LUENEBURG, E., 2004: A review of polarimetry in the context of synthetic aperture radar: concepts and information extraction. – *Canadian Journal of Remote Sensing*, **30**: 380-407.
- TUCKER, C. J., 1979: Red and Photographic Infrared Linear Combinations for Monitoring Vegetation. – *Remote Sensing of Environment*, **8**: 127-150.
- ULABY F. T., ALLEN, C. T., EGER, G., & KANEMASU, E., 1984: Relating the microwave backscattering coefficient to leaf area index. *Remote Sensing of Environment*, **14**: 113-133.
- ULABY, F. T., MOORE, R. K., & FUNG A. K. (ed.), 1986: *Microwave Remote Sensing. Active and Passive. Volume II*. Artech House, Norwood.
- ULABY, F. T., HELD, D., DONSON, M. C., McDONALD, K. C., & SENIOR, T. B. A., 1987: Relating Polarization Phase Difference of SAR Signals to Scene Properties. – *IEEE Transactions on Geoscience and Remote Sensing*, **25**(1): 83-92.
- ULABY, F. T., 1989: *Handbook of radar scattering statistics for terrain*. Artech House, Norwood.
- UN Database, 2012: <http://esa.un.org/unpd/wpp/unpp/p2k0data.asp> (accessed March 12, 2012).
- USGS, 2007: EO-1 User's Guide, <http://eo1.usgs.gov/userGuide/index.php> (accessed March 25, 2012).
- VAN ZYL, J. J., 2011: *Synthetic Aperture Radar Polarimetry. Band 2*. JPL Space Science and Technology Series. John Wiley & Sons, New York.
- WATSON, D., 1947: Comparative physiological studies in the growth of field crops. Variation in net assimilation rate and leaf area between species and varieties, and within and between years. – *Annals of Botany*, **11**: 41-76.
- WOODHOUSE, I. H. (ed.), 2006: *Introduction to Microwave Remote Sensing*. Taylor & Francis, New York.

- WOOSTER, M., 2007: Remote sensing: sensors and systems. – *Progress in Physical Geography*, **31**(1): 95-100.
- WU, F., WANG, C., ZHANG, H., ZHANG, B., & TANG, Y., 2011: Rice Crop Monitoring in South China with RADARSAT-2 Quad-Polarization SAR Data. – *IEEE Geoscience and Remote Sensing Letters*, **8**: 196-200.
- XAVIER, A. C., RUDORFF, B. F. T., MOREIRA, M. A., ALVARENGA, B. S., DE FREITAS, J. G., & SALOMON, M. V., 2006: Hyperspectral field reflectance measurements to estimate wheat grain yield and plant height. – *Science Agriculture*, **63**: 130-138.
- YOSHIDA, S., 1981: Fundamentals of rice crop science. IRRI, Los Baños.
- ZARCO-TEJADA, P. J., BERJÓN, A., & MILLER, J. R., 2007: Stress detection in crops with hyperspectral remote sensing and physical simulation models. Airborne Imaging Spectroscopy Workshop, October 8, 2004, Bruges, Belgium.
- ZHANG, Y., WANG, C., WU, W., QI, J., & SALAS, W. A., 2009: Mapping paddy rice with multitemporal ALOS/PALSAR imagery in southeast China. – *International Journal of Remote Sensing*, **30**: 6301-6315.
- ZHAO, D., LI, J., & QI, J., 2004: Hyperspectral characteristic analysis of a developing cotton canopy under different nitrogen treatments. – *Agronomie*, **24**: 463-471.
- ZHAO D., HUANG, L., LI, J., & QI, J., 2007: A comparative analysis of broadband and narrowband derived vegetation indices in predicting LAI and CCD of a cotton canopy. – *ISPRS Journal of Photogrammetry & Remote Sensing*, **62**: 25-33.

APPENDIX

A.1: Selection of Standard Vegetation Indices

Table A-1: Standard vegetation indices.

Index	Name	Description	Reference
NDVI	Normalized Difference Vegetation Index	$\frac{R_{NIR} - R_{RED}}{R_{NIR} + R_{RED}}$	Rouse et al. (1974)
RVI	Ratio Vegetation Index	R_{NIR} / R_{RED}	Pearson & Miller (1972)
SAVI	Soil Adjusted Vegetation Index	$(1+L) * (R_{800} - R_{670}) / (R_{800} - R_{670} + L)$	Haboudane et al. (2004)
OSAVI	Optimized Soil-Adjusted Vegetation Index	$(1+0.16) \frac{R_{800} - R_{670}}{R_{800} + R_{670} + 0.16}$	Rondeaux et al. (1996)
HVI	Hyperspectral Vegetation Index	$R_{750} - R_{700}$	Gitelson et al. (1996)
HNDVI	Hyperspectral Normalized Difference Vegetation Index	$\frac{R_{827} - R_{668}}{R_{827} + R_{668}}$	Oppelt & Mauser (2004)
GI	Greennees Index	R_{554} / R_{677}	Zarco-Tejada et al. (2007)
TVI	Triangular Vegetation Index	$0.5 * [120 * (R_{750} - R_{550}) - 200 * (R_{670} - R_{550})]$	Broge & Leblanc (2000)
MCARI2	Modified Chlorophyll Absorption Ratio Index	$\frac{1.5 * [2.5 * (R_{800} - R_{670}) - 1.3 * (R_{800} - R_{550})]}{\sqrt{(2 * R_{800} + 1) - (6 * R_{800} - 5 * \sqrt{R_{670}}) - 0.5}}$	Haboudane et al. (2004)
TCI	Triangle Chlorophyll Vegetation Index	$\frac{(R_{800} + 1.5 * R_{550}) - R_{675}}{R_{800} - R_{700}}$	Gao (2006)
RRE	Reflexion Red Edge	$(R_{670} + R_{780}) / 2$	Baret & Guyot (1991)
REP	Red Edge Position	$700 + (740 - 700) * \frac{R_{re} - R_{700}}{R_{740} - R_{700}}$	Baret & Guyot (1991)

A.2: TerraSAR-X HH and VV Imagery of Rice

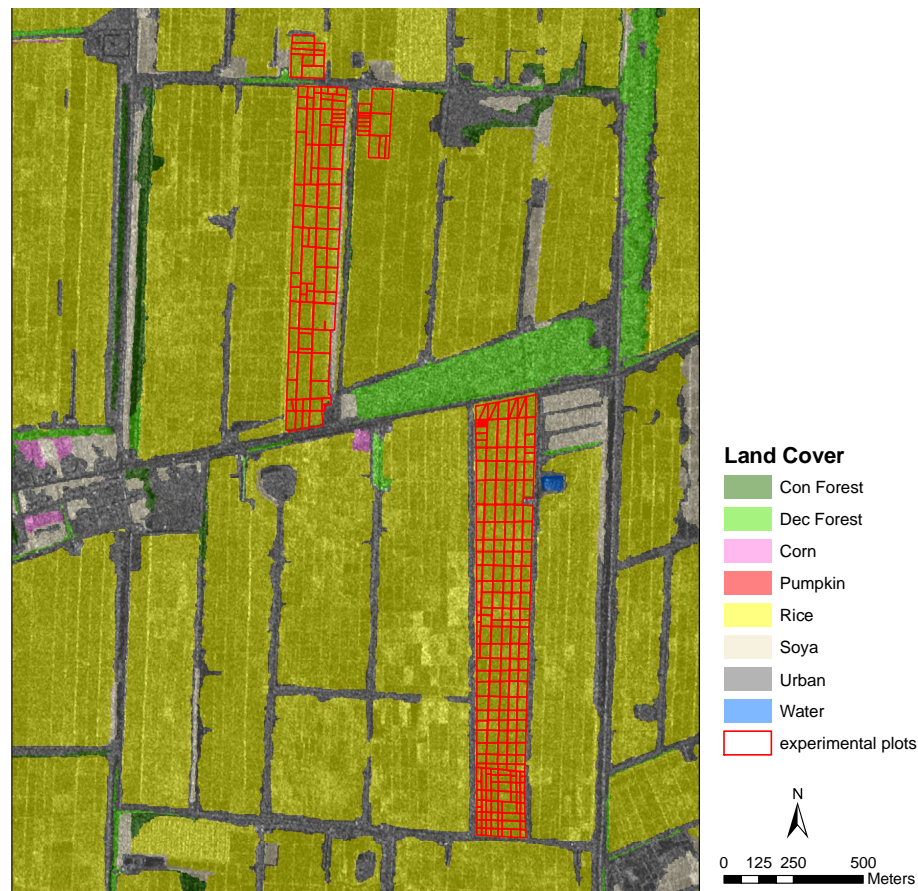
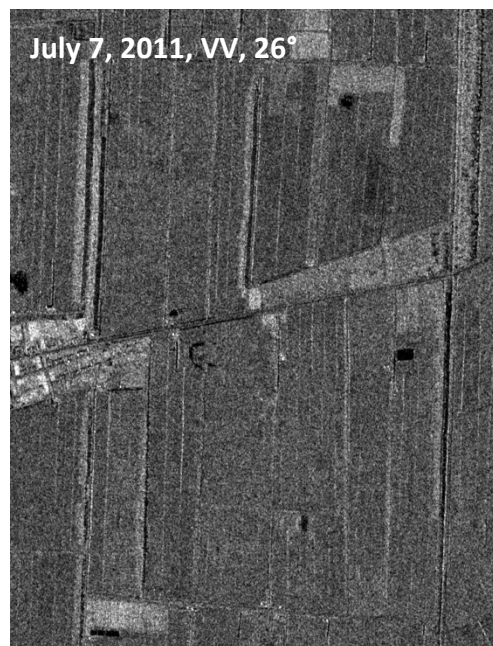
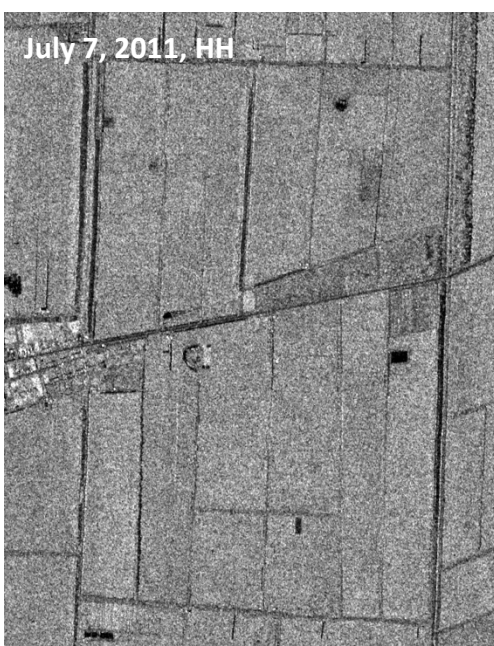
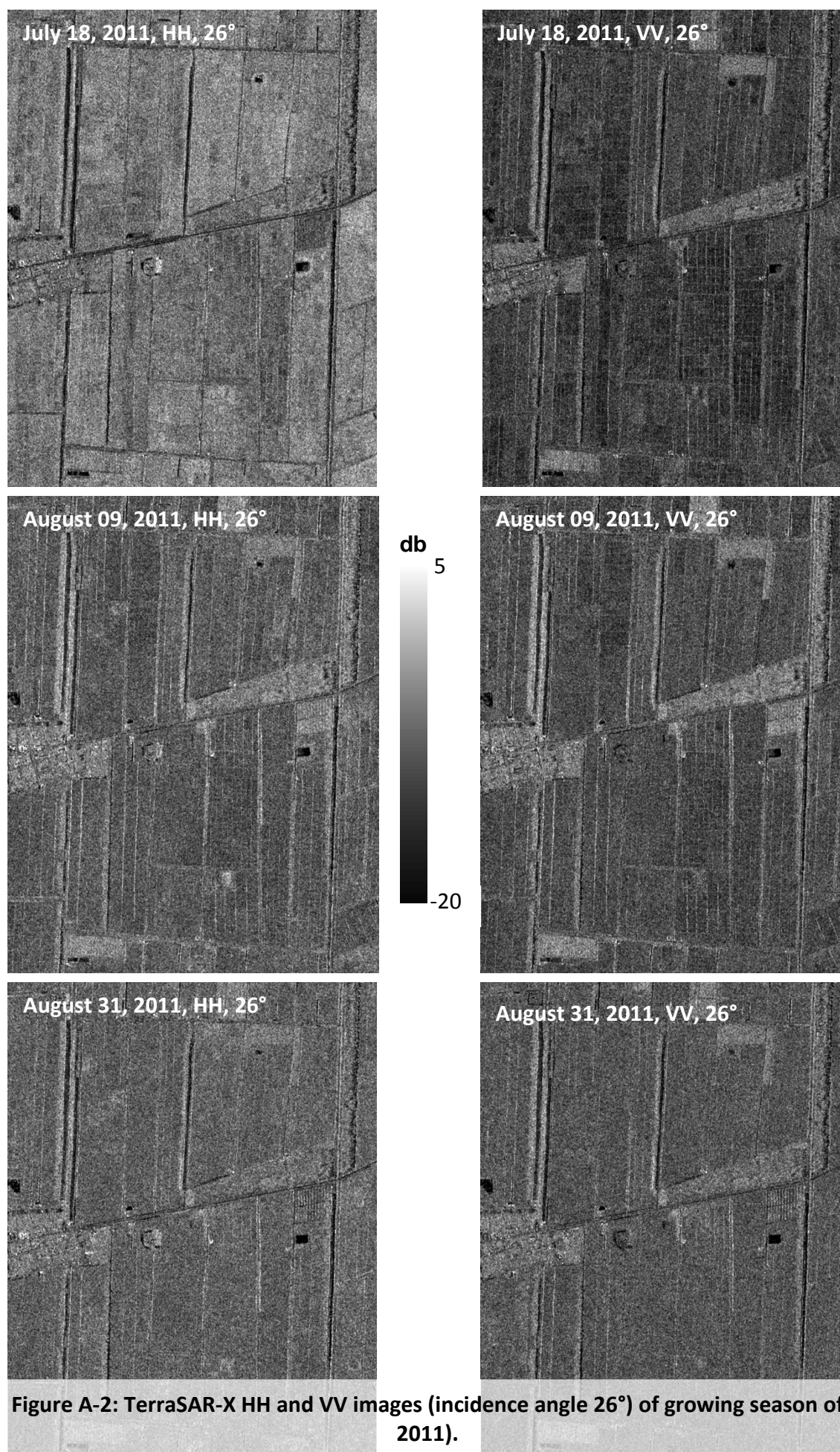


Figure A-1: Landcover classification (TerraSAR-X HS 2009, July 5 and July 27) (modified after Hütt, 2012), overlaid by experimental plots.

Appendix A.2 gives an overview about the used field plots for biomass correlation analysis in 2009 and polarimetric backscatter analysis in 2011 (Figure A-1). Below in Figure A-2 the TerraSAR-X imagery of HH and VV (26°) of the area of interest are shown. The backscatter of VV is always lower than of HH, at the end of the growing season HH and VV approach each other.





A.3: Separability of Rice against other Crops

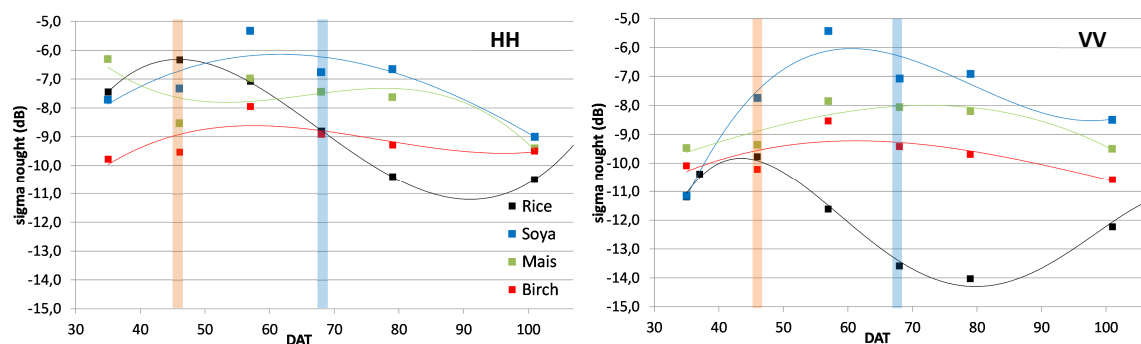


Figure A-3: X-band backscatter (inc. angle 39°) of HH and VV of rice crop 2009.

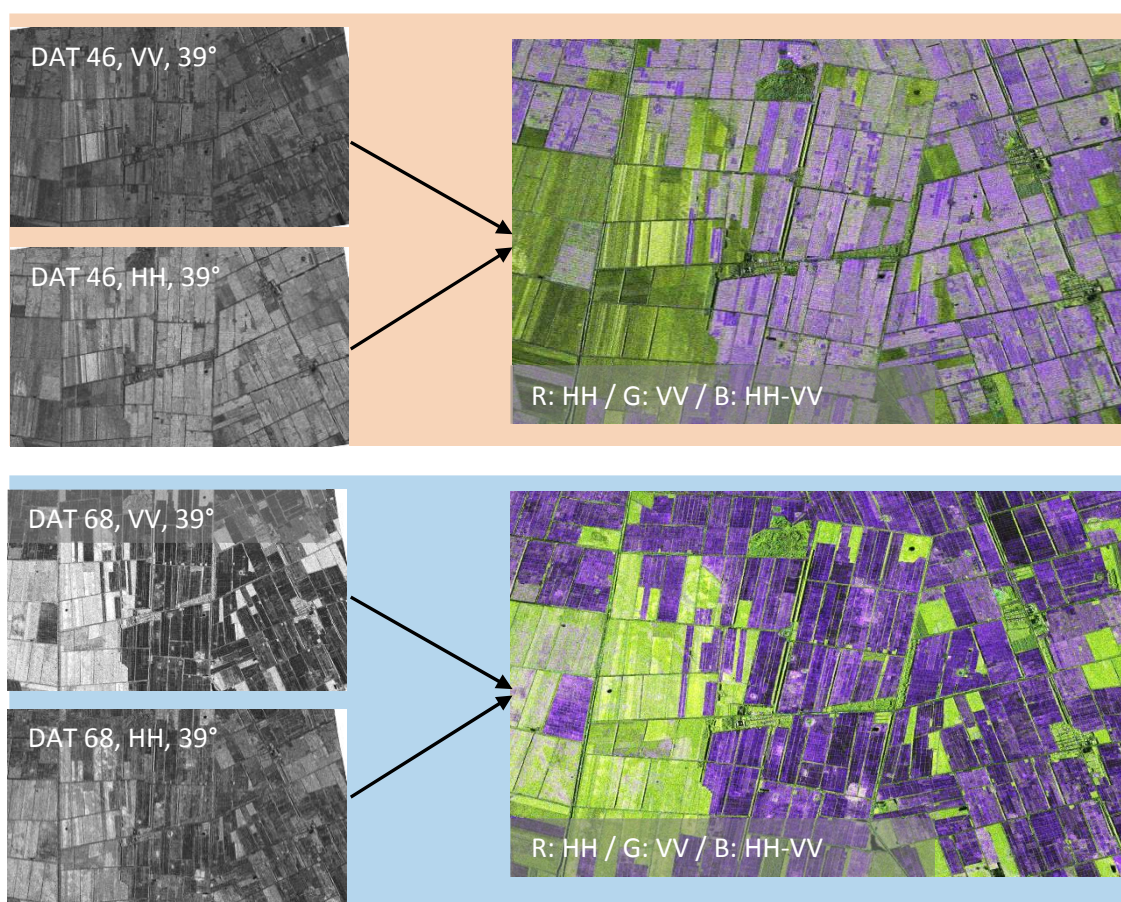


Figure A-4: TerraSAR-X color composite of DAT 46 and DAT 68 (2009).

Backscatter analysis of polarimetric amplitude is important for land cover classification. Based on the unique backscatter signature of HH and VV compared to other land cover classes of this area, rice can be identified especially on the difference between HH and VV (purple areas in Figure A-4). Considering single polarizations, the separability is limited, especially around DAT 30 to DAT 50 (see Figure A-3). The

dynamic range for all classes for HH is within 3.5 dB. But by combining both polarizations, the difference between rice and non-rice becomes obvious (see Figure A-4 and Figure A-5).

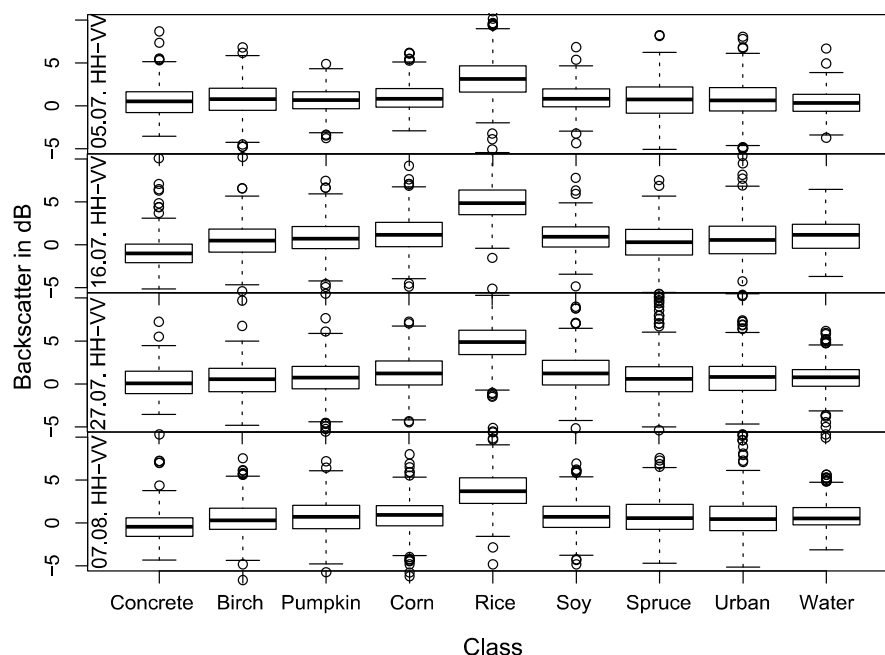


Figure A-5: Separability analyses of land cover classes based on HH and VV difference (modified after Hütt 2012).

As an outlook, the separability based on alpha angle at beginning of august 2009 (alpha-entropy decomposition) is shown in Figure A-7. The alpha angle of rice strongly differs from the other land cover classes.

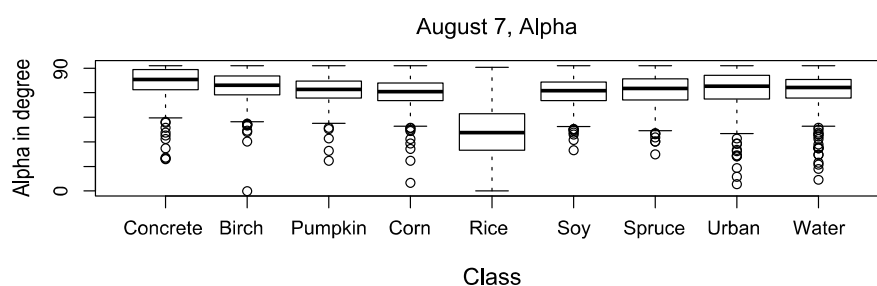
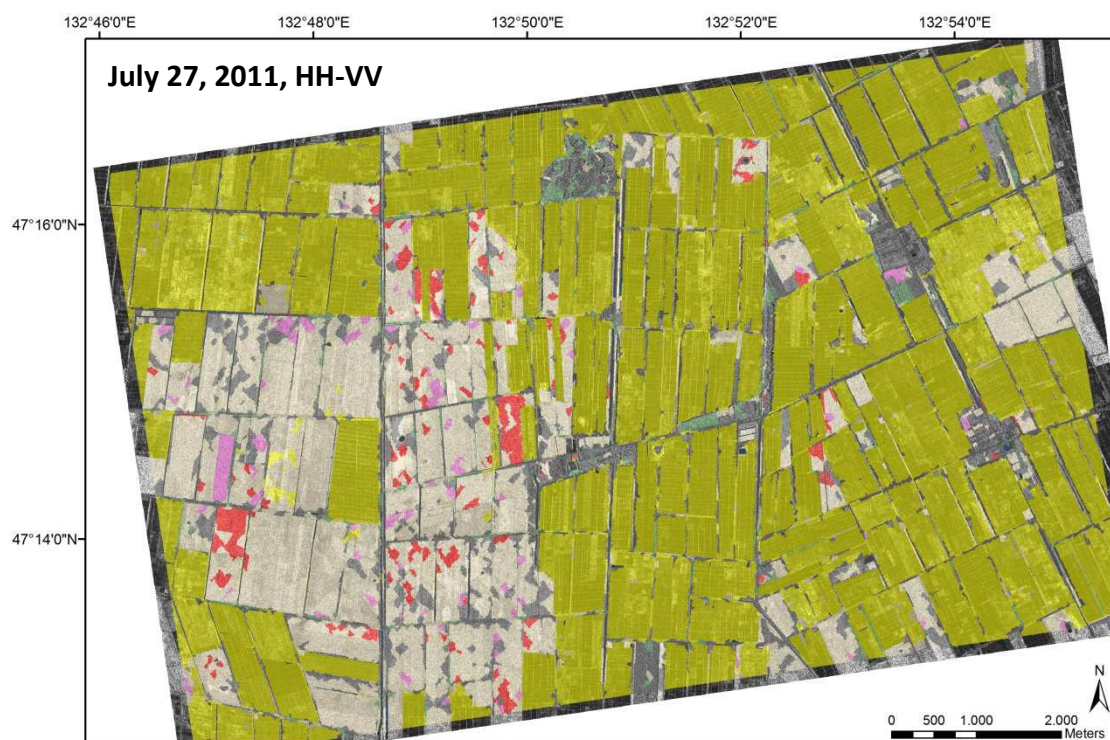
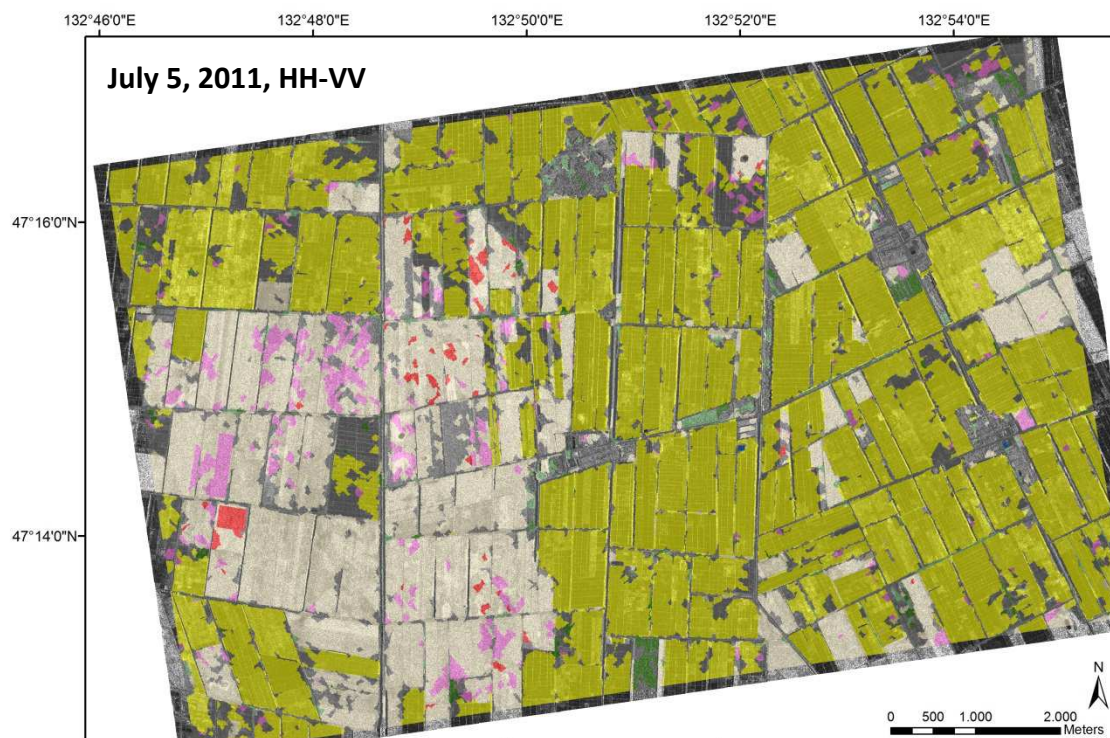


Figure A-6: Separability analyses of land cover classes based on alpha angle (modified after Hütt 2012).

Below are two land cover object based classifications, classified on amplitude and HH-VV difference from July 5 and from July 27. Considering only the separability of rice areas, results confirm the theoretical analysis of Figure A-4 and Figure A-5. Based on visual evaluation, the rice areas are significantly better classified at July 27, also if the user and producer accuracy of rice are similar in both classifications (Hütt 2012).

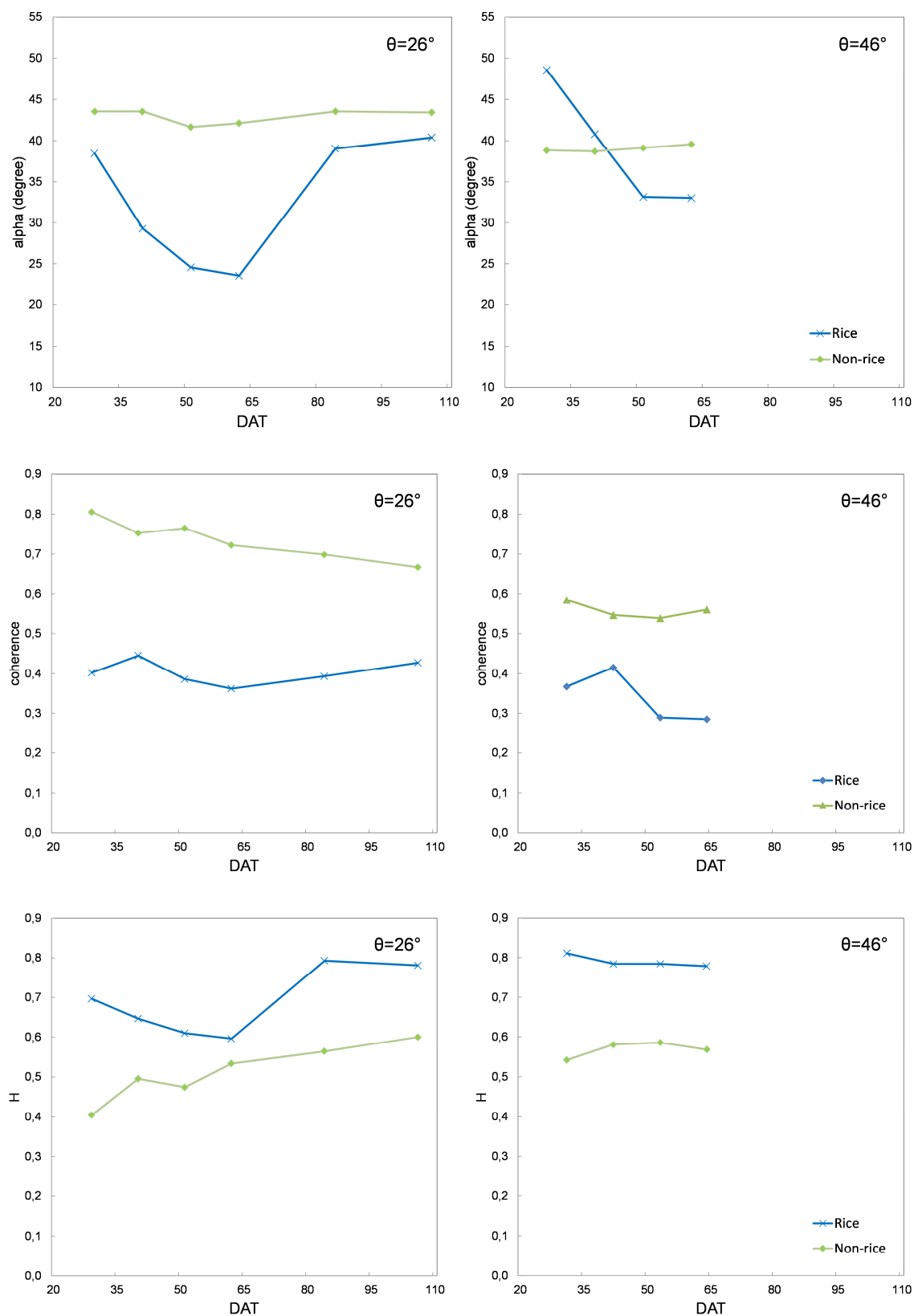


Land Cover



Figure A-7: Land cover classifications (modified after Hütt 2012).

A.4: Polarimetric parameters for rice and non-rice.



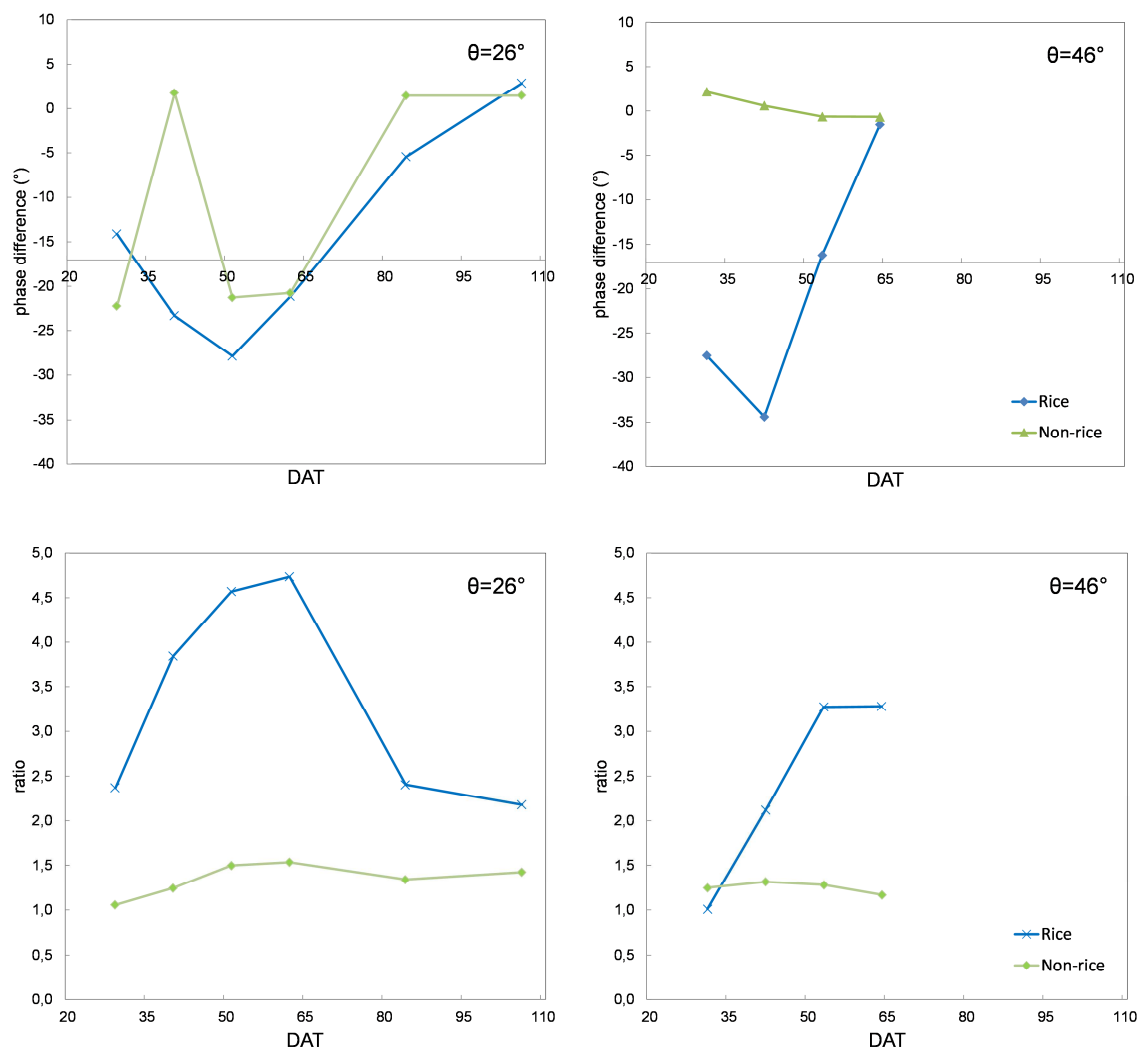


Figure A-8: Polarimetric parameters for rice and non-rice for incidence angle of 26° and 46°

Erklärung

Ich versichere, dass ich die von mir vorgelegte Dissertation selbständig angefertigt, die benutzten Quellen und Hilfsmittel vollständig angegeben und die Stellen der Arbeit – einschließlich Tabellen, Karten und Abbildungen –, die anderen Werken im Wortlaut oder dem Sinn nach entnommen sind, in jedem Einzelfall als Entlehnung kenntlich gemacht habe; dass diese Dissertation noch keiner anderen Fakultät oder Universität zur Prüfung vorgelegen hat; dass sie – abgesehen von unten angegebenen Teilpublikationen – noch nicht veröffentlicht worden ist sowie, dass ich eine solche Veröffentlichung vor Abschluss des Promotionsverfahrens nicht vornehmen werde. Die Bestimmungen der Promotionsordnung sind mir bekannt. Die von mir vorgelegte Dissertation ist von Prof. Dr. Georg Bareth betreut worden.

Köln, den 15. November 2013

Teilpublikationen:

- KOPPE, W., GNYP, M. L., LAUDIEN, R., JIA, L., LI, F., CHEN, X., ZHANG, F., & BARETH, G., 2006: Deriving of winter wheat characteristics from combined radar and hyperspectral data analysis. – SPIE Proceedings, Geoinformatics'2006, Wuhan, China.
- KOPPE, W., LI, F., GNYP, M. L., MIAO, Y., JIA, L., CHEN, X., ZHANG, F., & BARETH, G., 2010: Evaluating Multispectral and Hyperspectral Satellite Remote Sensing Data for Estimating Winter Wheat Growth Parameters at Regional Scale in the North China Plain. – Photogrammetrie, Fernerkundung, Geoinformation, **3**: 167-178.
- KOPPE, W., GNYP, M. L., YAO, Y., MIAO, Y., & BARETH, G., 2011: Agricultural Monitoring with Spaceborne X-band SAR Data. – Proceedings on the Workshop of Remote Sensing Methods for Change Detection and Process Modelling, 18-19 November 2010, University of Cologne, Germany, Kölner Geographische Arbeiten, **92**: 55-61.
- KOPPE, W., HENNIG, S. D., LI, F., GNYP, M. L., MIAO, Y., JIA, L., CHEN, X., & BARETH, G., 2012: Multi-Temporal Hyperspectral and Radar Remote Sensing for Estimating Winter Wheat Biomass in the North China Plain. – Photogrammetrie, Fernerkundung, Geoinformation, **3**: 281-298.
- KOPPE, W., LI, F., GNYP, M. L., HÜTT, C., MIAO, Y., YAO, Y., CHEN, X., & BARETH, G., 2013: Rice monitoring with multi-temporal and dual-polarimetric TerraSAR-X data. – International Journal of Applied Earth Observation and Geoinformation, **21**: 568-576.

Wolfgang Koppe

Professional Interests: SAR, Polarimetry, 3D techniques, Sensor fusion, GIS, Avionic

Personal Details

Date of Birth: 26 May 1977
 Place of Birth: Jena, Germany
 Marital status: single

Employment History

since 12.2012	Expert status (SAR and Geo-information) within EADS
since 03.2009	Geo-information Application Development Manager <i>Infoterra GmbH (EADS-Astrium), Friedrichshafen</i>
07.2007 – 02.2009	Radar Development and Production Engineer <i>Infoterra GmbH (EADS-Astrium), Friedrichshafen</i>
12.2006 – 06.2007	Student Assistant <i>Fraunhofer FGAN FHR, Wachtberg</i>
11.2005 – 09.2006	Student Assistant <i>ZFL (Zentrum für Fernerkundung der Landoberfläche), Bonn</i>
since 01.2005	PhD Student <i>GIS and Remote Sensing Group, University of Cologne</i>
01.2003 – 12.2004	Diploma Thesis, Freelancer <i>Infoterra GmbH (EADS-Astrium), Friedrichshafen</i>

Education and Qualifications

10.1997 – 12.2003	Study of Geography <i>Friedrich-Schiller-University Jena, Germany</i> Main subject: Geoinformatic, Physical Geography Secondary subject: Geology, Ecology
10.1991 – 06.1995	Albert-Schweitzer-Gymnasium, Jena
09.1983 – 06.1991	POS Grete-Unrein, Jena

Internship, Work Experience

08.2002 – 09.2002	GAF München
08.2001 – 09.2001	German Aerospace Center (DLR), Oberpfaffenhofen
02.1999 – 01.2003	Institute of Geography, University Jena – Student Assistant
02.1997 – 08.1998	Department of Archeology, Weimar

Courses

2011	Project Management, EADS, Friedrichshafen, Germany
2010	FGAN/FHR Summer School on Radar/SAR, Remagen, Germany
2010	SARscape, CREASO, Gilching, Germany

Personal Skills

Software:	ERDAS Imagine, ENVI, SARSCAPE, PCI Geomatica, eCognition, ArcGIS, MS Office, ADOBE Photoshop, MS Visio
Native language:	German
Other languages:	English – excellent Russian – basic knowledge
Personal Interests:	sport (table tennis, soccer, skiing), reading, traveling

Publications (first Author)

- KOPPE, W., LI, F., GNYP, M. L., HÜTT, C., MIAO, Y., YAO, Y., CHEN, X., & BARETH, G., 2013: Rice monitoring with multi-temporal and dual-polarimetric TerraSAR-X data. - International Journal of Applied Earth Observation and Geoinformation, **21**: 568-576.
- KOPPE, W., HENNIG, S. D., LI, F., GNYP, M. L., MIAO, Y., JIA, L., CHEN, X., & BARETH, G., 2012: Multi-Temporal Hyperspectral and Radar Remote Sensing for Estimating Winter Wheat Biomass in the North China Plain. – Photogrammetrie, Fernerkundung, Geoinformation, **3**: 281-298.
- KOPPE, W., LI, F., GNYP, M. L., MIAO, Y., JIA, L., CHEN, X., ZHANG, F., & BARETH, G., 2010: Evaluating Multispectral and Hyperspectral Satellite Remote Sensing Data for Estimating Winter Wheat Growth Parameters at Regional Scale in the North China Plain. – Photogrammetrie, Fernerkundung, Geoinformation, **3**: 167-178.

Conference Contributions (first Author)

- KOPPE, W., BACH, K., & LUMSDON, P., 2013, submitted: Benefits of TerraSAR-X – PAZ Constellations for Maritime Surveillance. – 10th Eur. Conf. on Synthetic Aperture Radar, EUSAR, 3-5 June 2014, Berlin.
- KOPPE, W., HUMMEL, P., & RAGGAM, H., 2012: TerraSAR-X Stereo Imagery for Ground Control Points retrieval. 6th International Conference on Recent Advances in space Technologies, RAST 2013, June 12 – June 14., Istanbul.
- KOPPE, W., HENNIG, S.D., JANOTH, J., HUMMEL, P., & RAGGAM, H., 2012: Accuracy Validation of TerraSAR-X derived Ground Control Points. IGARSS 2012, July 22 – July 27, Munich.
- KOPPE, W., GNYP, M. L., YAO, Y., MIAO, Y., & BARETH, G., 2011: Agricultural Monitoring with Spaceborne X-band SAR Data. – Proceedings on the Workshop of Remote Sensing Methods for Change Detection and Process Modelling, 18-19 November 2010, University of Cologne, Germany, *Kölner Geographische Arbeiten*, **92**: 55-61.
- KOPPE, W., KIEFL, N., HENNIG, S. D., & JANOTH, J., 2010: Validation of Pixel Location Accuracy of Orthorectified TerraSAR-X Products. 8th European Conference on Synthetic Aperture Radar, 07.-10. June 2010, Eurogress, Aachen, Germany.
- KOPPE, W., KIEFL, N., HENNIG, S. D., & JANOTH, J., 2010: Assessment of TerraSAR-X Orthorectified Imagery Based on Commonly Used DEMs as well as on TerraSAR-X Stereo DEM. XXIV FIG International Congress 2010, Sydney, Australia, 11-15 April 2010.
- KOPPE, W., KIEFL, N., HENNIG, S. D., & JANOTH, J., 2010: Validation of Pixel Location Accuracy of Orthorectified TerraSAR-X Products. – 8th European Conference on Synthetic Aperture Radar, Aachen, 7-10 June, Aachen.
- KOPPE, W., GNYP, M. L., LAUDIEN, R., JIA, L., LI, F., CHEN, X., ZHANG, F., & BARETH, G., 2006: Deriving of winter wheat characteristics from combined radar and hyperspectral data analysis. – SPIE Proceedings, Geoinformatics'2006, Wuhan, China.
- KOPPE, W., 2006: Monitoring of Grassland Biomass by Multitemporal Remote Sensing Data. 2nd Workshop of the EARSel Special Interest Group on Land Use and Land Cover, Bonn, Germany, 2006.
- KOPPE, W., GNYP, M. L., LAUDIEN, R., JIA, L., LI, F., CHEN, X., ZHANG, F., & BARETH, G., 2006: Spektrale Charakterisierung von Winterweizen für hyperspektrale Fernerkundungsanalysen. – DGPF Annual Conference 2006, Berlin.